

AL-TR-90-063

AD:

AD-A231 830



Final Report  
for the period  
November 1988  
to June 1990

**Aluminum Alloys for ALS Cryogenic  
Tanks: Oxygen Compatibility  
Volume 2. Final Report**

September 1990

Authors:  
R.P Reed  
N.J. Simon  
J.D. McColskey  
C.N. McCowen  
E.S. Drexler

National Institute of Standards and  
Technology  
325 Broadway  
Boulder CO 80303  
AL 99011

DTIC  
ELECTE  
S' FEB 06 1991 D  
B

**Approved for Public Release**

Distribution is unlimited. The AL Technical Services Office has reviewed this report, and it is releasable to the National Technical Information Service, where it will be available to the general public, including foreign nationals.

*Prepared for the:* **Astronautics Laboratory (AFSC)**  
Air Force Space Technology Center  
Space Systems Division  
Air Force Systems Command  
Edwards AFB CA 93523-5000

91 2 04 066

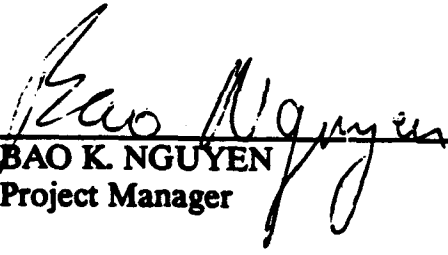
## NOTICE

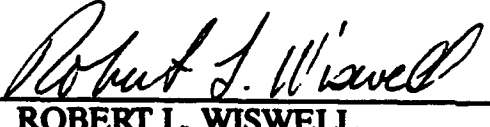
When U. S. Government drawings, specifications, or other data are used for any purpose other than a definitely related Government procurement operation, the fact that the Government may have formulated, furnished, or in any way supplied the said drawings, specifications, or other data, is not to be regarded by implication or otherwise, or in any way licensing the holder or any other person or corporation, or conveying any rights or permission to manufacture, use or sell any patented invention that may be related thereto.

## FOREWORD

This final report was submitted by National Institute of Standards and Technology, Boulder CO on completion of contract AL 99011 with the Astronautics Laboratory (AFSC), Edwards AFB CA. AL Project Managers were Bao Nguyen and Lt Bruce Pham.

This report has been reviewed and is approved for release and distribution in accordance with the distribution statement on the cover and on the DD Form 1473.

  
BAO K. NGUYEN  
Project Manager

  
ROBERT L. WISWELL  
Chief, Liquid Propulsion Branch

FOR THE DIRECTOR

  
CLARK W. HAWK  
Director, Propulsion Division

## REPORT DOCUMENTATION PAGE

Form Approved  
OMB No. 0704-0188

1a. REPORT SECURITY CLASSIFICATION UNCLASSIFIED		1b. RESTRICTIVE MARKINGS										
2a. SECURITY CLASSIFICATION AUTHORITY.		3. DISTRIBUTION/AVAILABILITY OF REPORT Approved for Public Release Distribution is Unlimited										
2b. DECLASSIFICATION/DOWNGRADING SCHEDULE												
4. PERFORMING ORGANIZATION REPORT NUMBER(S)  NISTIR3943		5. MONITORING ORGANIZATION REPORT NUMBER(S)  AL-TR-90-063 Vol. 2										
6a. NAME OF PERFORMING ORGANIZATION National Institute of Standards and Technology	6b. OFFICE SYMBOL (If applicable)	7a. NAME OF MONITORING ORGANIZATION Astronautics Laboratory										
6c. ADDRESS (City, State, and ZIP Code) 325 Broadway Boulder, Colorado 80303	7b. ADDRESS (City, State, and ZIP Code) AL/RKLB Edwards AFB CA 93523-5000											
8a. NAME OF FUNDING/SPONSORING ORGANIZATION	8b. OFFICE SYMBOL (If applicable)	9. PROCUREMENT INSTRUMENT IDENTIFICATION NUMBER AL 99011										
8c. ADDRESS (City, State, and ZIP Code)	10. SOURCE OF FUNDING NUMBERS  <table border="1"><tr><td>PROGRAM ELEMENT NO.</td><td>PROJECT NO.</td><td>TASK NO.</td><td>WORK UNIT ACCESSION NO.</td></tr><tr><td>4SL1</td><td>3148</td><td></td><td></td></tr></table>			PROGRAM ELEMENT NO.	PROJECT NO.	TASK NO.	WORK UNIT ACCESSION NO.	4SL1	3148			
PROGRAM ELEMENT NO.	PROJECT NO.	TASK NO.	WORK UNIT ACCESSION NO.									
4SL1	3148											
11. TITLE (Include Security Classification) Aluminum Alloys for ALS Cryogenic Tanks: Oxygen Compatibility--Final Report												
12. PERSONAL AUTHOR(S) Reed, Richard Palmer, Simon, Nancy Jane, McColskey, Joseph David, McCowan, Christopher Nelson, and Drexler, Elizabeth Susan												
13a. TYPE OF REPORT Final	13b. TIME COVERED FROM 8811 TC 9006	14. DATE OF REPORT (Year, Month, Day) 9009	15. PAGE COUNT 126									
16. SUPPLEMENTARY NOTATION												
17. COSATI CODES <table border="1"><tr><th>FIELD</th><th>GROUP</th><th>SUB-GROUP</th></tr><tr><td>13</td><td>13</td><td></td></tr><tr><td>11</td><td>06</td><td>01</td></tr></table>		FIELD	GROUP	SUB-GROUP	13	13		11	06	01	18. SUBJECT TERMS (Continue on reverse if necessary and identify by block number) aluminum alloys, 2219, aluminum-lithium alloys, 8090, 2090, Weldalite, oxygen compatibility, mechanical-impact test, LOX compatibility, promoted-combustion test, oxygen reaction	
FIELD	GROUP	SUB-GROUP										
13	13											
11	06	01										
19. ABSTRACT (Continue on reverse if necessary and identify by block number) In Part II of this program, selected tempers of alloys 8090, 2090, WL049, and 2219 were tested for compatibility with liquid oxygen in modified open-cup and pressurized mechanical-impact equipment at White Sands Test Facility. Drop height (potential energy), pressure, and environment (liquid oxygen, LOX, and gaseous oxygen, GOX) were varied in these tests. Additional promoted-combustion tests were also conducted at WSTF.												
Reactions, ranging in size from those that could be observed with the naked eye to those that required use of the scanning electron microscope (SEM), were identified in all alloys. Those that require little or no magnifying power to view are labeled macroreactions; those that require the use of optical microscopy or SEM are called microreactions. Al-Li alloys had more macroreactions than 2219; 2219 had more, or an equivalent number of microreactions than each of the Al-Li alloys. The discovery that reactions with oxygen occur over a large range of sizes emphasizes an inherent												
20. DISTRIBUTION/AVAILABILITY OF ABSTRACT <input checked="" type="checkbox"/> UNCLASSIFIED/UNLIMITED <input type="checkbox"/> SAME AS RPT. <input type="checkbox"/> DTIC USERS		21. ABSTRACT SECURITY CLASSIFICATION UNCLASSIFIED										
22a. NAME OF RESPONSIBLE INDIVIDUAL BAO K. NGUYEN		22b. TELEPHONE (Include Area Code) 805-275-5541	22c. OFFICE SYMBOL RKLB									

19.

ambiguity in the definition of a reaction in mechanical-impact tests. Current practice of accepting only visual observations leads to inconsistencies (reactions may be overlooked and their observation depends on proper lighting conditions). The size of reactions observed in these tests has not been correlated with in-service performance.

Circumferential tensile (hoop) stresses in the mechanical-impact tests are of the order of magnitude required to fracture the Al-alloy specimens. Most specimens crack internally or fracture (split) inwardly from the perimeter. The minimum absorbed energy needed to induce splitting (tensile failure) in the specimen has been found to be less than, or equal to, that required to induce reactions. Therefore, mechanical failure will precede, or usually be attendant with, reactions in oxygen environments.

Al-Li alloys were superior to 2219 in flammability in the presence of GOX, as measured in the promoted-combustion tests. Therefore, within the ability of the current tests to discern relative compatibility and flammability with LOX and GOX, the Al-Li alloys and 2219 must be judged equally acceptable for Advanced Launch System (ALS) cryogenic tankage. Modifications to the current NASA NHB 8060.1B standard for mechanical-impact tests in LOX or GOX are suggested; these changes would reduce the large disparity in test procedures that currently exists among laboratories that conduct these tests.

Accession For	
NTIS GRA&I	<input checked="" type="checkbox"/>
DTIC TAB	<input type="checkbox"/>
Unannounced	<input type="checkbox"/>
Justification	
By _____	
Distribution/	
Availability Codes	
Dist	Avail and/or Special
A-1	



## CONTENTS

II.1. Executive Summary	1.
II.2. Introduction	3.
II.3. Material Characterization	4.
II.3.1. Inventory	4.
II.3.2. Chemical Composition	4.
II.3.3. Microstructure of the As-Received Materials	4.
II.4. Experimental Procedures	11.
II.4.1. Impact Specimen Preparation	11.
II.4.1.1. Test Specimen Machining and Surface Finish	11.
II.4.1.2. Specimen Cleaning Procedure	11.
II.4.2. Mechanical-Impact Tests in the Modified Open-Cup Machine	11.
II.4.2.1. Equipment and Procedures	11.
II.4.2.2. Materials	12.
II.4.2.3. Conditions	12.
II.4.3. LOX and GOX Impact Tests in the Modified Pressurized Impact Machine	12.
II.4.3.1. Equipment and Procedures	12.
II.4.3.2. Materials and Conditions	14.
II.4.4. Calibration of Open-Cup and Pressurized Testers	18.
II.4.4.1. Open-Cup Tester	18.
II.4.4.2. Pressurized Tester	21.
II.5. Experimental Results	23.
II.5.1. Fracture and Deformation Modes	23.
II.5.1.1. Anisotropic Radial Shear Deformation	23.
II.5.1.2. Shear Lips	23.
II.5.1.3. Striker-Pin Eccentricity	26.
II.5.1.4. Splits	26.
II.5.1.5. Cracks	32.
II.5.1.6. Adiabatic Shear Bands	32.
II.5.1.7. Striker-Pin/Specimen Friction	39.
II.5.1.8. Localized Melting	39.
II.5.2. Open-Cup Mechanical-Impact Tests	40.
II.5.2.1. Initial Report of Reactions Observed by WSTF Staff	40.
II.5.2.2. Physical Measurements of Specimens	46.
II.5.2.3. Macroreactions in Open-Cup Tests	51.
II.5.3. Pressurized Mechanical-Impact Tests	51.
II.5.3.1. Initial Report of Reactions Observed by WSTF Staff	51.
II.5.3.2. Physical Measurements on Specimens	61.
II.5.3.3. Comparison of Macroreactions and Physical Measurements, Pressurized and Open-Cup Tests	61.
II.5.4. Comparison of Mechanical-Impact Equipment and Procedures at WSTF, MSFC, and SSFL	67.
II.5.5. Promoted-Combustion Tests	69.
II.6. Ignition Temperatures and Conditions	75.
II.6.1. Experimental Studies of Ignition Temperature of Al in O <sub>2</sub>	75.
II.6.2. Experimental Studies of Ignition Temperature of Al in N <sub>2</sub>	76.
II.7. Discussion	77.
II.7.1. Absorbed Energy	77.
II.7.2. Splits	78.

II.7.3.	Rebound Heights	78.
II.7.4.	Reactions	82.
II.7.4.1.	Microreactions	82.
II.7.4.2.	Size of Reactions	88.
II.7.5.	Reaction/Fracture Relationship	94.
II.7.6.	Reactions in Al-Li Alloys and Alloy 2219	96.
II.8.	Summary	99.
II.8.1.	Definition of Reaction	99.
II.8.2.	NASA Standard NHB 8090.1B (Paragraph 413, test 13)	99.
II.8.3.	Reaction/Fracture Energies	100.
II.8.4.	Comparison of Al-Li Alloys with 2219	100.
II.9.	Recommendations	102.
II.10.	Acknowledgements	103.
II.11.	References	104.
II.12.	Appendix	107.

## LIST OF FIGURES

<u>Figure Number</u>		
II.3.1.	The grain size and morphology of (a) the WL049-T851 (Lot 1) temper and (b) the WL049-T651 temper.	7.
II.3.2.	The grain size and morphology of (a) the WL049-T851 (Lot 2) alloy and (b) the 2219-T87 alloy.	8.
II.4.1.	Schematics of the original open-cup test machine (a) and the modified open-cup test machine (b) with the specimen centering ring and without (c).	13.
II.4.2.	Standard WSTF pressurized test machine. (Figure by M. Rucker, WSTF.)	15.
II.4.3.	Modified WSTF pressurized test machine. (Figure by M. Rucker, WSTF.)	16.
II.5.1.	Deformation modes in mechanical-impact test specimen: (a) Concentric strike, (b) Eccentric strike.	24.
II.5.2.	Long axis of deformed specimen parallel to rolling direction. Etched WL049-T851, tested in open cup at 6 kg·m. (5X)	25.
II.5.3.	Extensive shear lip (lower, right-of-center) in 2090-T81, tested in GOX at ambient pressure. (5X) Shear lip in 2090-T81, tested in GOX, ambient pressure (a) lip at lower, right-of-center. (5X) (b) microridges on lip formed by friction between striker pin and metal. (500X)	27.
II.5.4.	Grain structure beneath shear lip of 2219-T37. (10 kg·m, LOX). (100X)	28.
II.5.5.	Grain structure adjacent to shear lip and indentation in 2090-T81 (10 kg·m, LOX).	29.
II.5.6.	Typical splits extending under the striker-pin indentation for (a) alloy 2090-T81, open-cup LOX, 6 kg·m; (b) WL049-T851, open-cup LOX, 10 kg·m; (c) 2219-T87, open-cup LOX, 10 kg·m.	30.
II.5.7.	Crack growth along L orientation in 2090-T87 at (a) 10 kg·m and (b) 8 kg·m open cup LOX.	31.
II.5.8.	The characteristic fracture surface of a split of the 2090-T81 open-cup LOX specimen: (a) low-magnification SEM micrograph of the general fracture morphology, (b) local, surface topography.	33.
II.5.9.	Transgranular shear and intergranular cracking layers in 2090-T81 specimen impacted at low temperatures (open-cup LOX). (750X)	34.
II.5.10.	Intergranular microcracking associated with split in 2090-T81 (10 kg·m, pressurized LOX). (100X)	35.
II.5.11.	Microcracks in 2090-T81 (a) adjacent to shear lip (8 kg·m, GOX), and (b) in region between bottom of shear lip (indicated by curved "line" on the top) and specimen perimeter (10 kg·m, GOX). (Both at 50X)	36.
II.5.12.	Adiabatic shear bands adjacent to shear lip in (a) 2090-T81 (130X), (b) WL049-T851 (400X), and (c) 2219-T87 (130X).	37.

II.5.13.	Regions of localized melting on shear lip (a, 1000X) and on compression surface (b, 500X) of 2090-T87 (10 kg·m, GOX).	41.
II.5.14.	Region of localized melting at the base of the shear lip in WL049-T851 (GOX, 6 kg·m).	42.
II.5.15.	Localized melting in 2219-T851 (10 kg·m, GOX) at the root of the shear lip. In both (a) and (b) the shear lip is on the top, the indentation (with specimen machining markings still showing) on the bottom.	43.
II.5.16.	Percentage of reactions vs. potential (impact) energy for open-cup tests in LOX.	45.
II.5.17.	Average penetration depth vs. potential (impact) energy for open-cup tests in LOX.	45.
II.5.18.	Percentage of reactions vs. average penetration depth for open-cup tests in LOX.	49.
II.5.19.	Average eccentricity vs. average penetration depth for open-cup tests in LOX with a potential (impact) energy of 10 kg·m.	49.
II.5.20.	Percentage of splits vs. average penetration depth for open-cup tests in LOX.	50.
II.5.21.	Percentage of splits vs. potential (impact) energy for open-cup tests in LOX.	50.
II.5.22.	Two reactions in 8090-T8771 (10 kg·m, open-cup LOX) that extend over large distances or shear lip. (5X)	52.
II.5.23.	Small reactions on shear lip of alloy 2090-T81 (8 kg·m, open-cup LOX). (5X)	53.
II.5.24.	Reactions in 2090-T81 (6 kg·m, open-cup LOX) along shear lip and at crack. Note the even smaller reaction below, and to the left of, the reaction at the crack. (5X)	54.
II.5.25.	Two extensive reactions in 2090 (6 kg·m, open-cup LOX) that initiated on shear lip. (5X)	55.
II.5.26.	Macroreaction on shear lip of WL049-T851 (10 kg·m, open-cup LOX). (5X)	56.
II.5.27.	Macroreaction at split in WL049-T651 (10 kg·m, open-cup LOX). (5X)	57.
II.5.28.	Reaction on shear lip of WL049-T651 (10 kg·m, open-cup LOX). (5X)	58.
II.5.29.	Reaction on shear lip of alloy 2219-T851 (10 kg·m, open-cup LOX). (5X)	59.
II.5.30.	Average penetration depth vs. potential (impact) energy for pressurized tests in LOX and GOX.	64.
II.5.31.	Percentage of splits vs. average penetration depth for pressurized tests in LOX and GOX.	64.
II.5.32.	Average eccentricity vs. average penetration depth for pressurized tests in LOX and GOX with a potential (impact) energy of 10 kg·m.	65.
II.5.33.	Absorbed energy vs. penetration depth for open-cup and pressurized tests in LOX and GOX.	68.
II.5.34.	Burn length vs. test pressure for (a) 8090-T8771, (b) 8090-T8151, (c) 8090-T3, (d) 2090-T81, 12.7-mm thick plate, (e) WL049-T851,	

	(f) WL049-T651, (g) WL049-T351, (h) 2219-T87, (i) 2219-T851, and (j) 2219-T37.	72.
II.5.35.	Summary of burn length vs. test pressure of fitted curves for the following alloys: 8090 (temper T8771, T8151, and T3); 2090-T81; WL049 (temper T851, T651, and T351); and 2219 (temper T87, T851, and T37).	72.
II.7.1.	Absorbed energy, calculated from specimen deformation characteristics, vs. absorbed energy, calculated from rebound heights.	74.
II.7.2.	Tensile fracture energy vs. minimum absorbed energy needed to induce splits in open-cup tests.	79.
II.7.3.	Average rebound height vs. potential energy from open-cup tests where (a) splits did not occur, and (b) where the specimen split.	80.
II.7.4.	Local microreaction on shear lip of 8090-T8771 from 10 kg·m, pressurized LOX test. 100X(SEM)	81.
II.7.5.	Local microreactions on back of 2090-T81 specimens from 10 kg·m, pressurized GOX tests (a) 50X, (b) 500X, (c) 1000X, and (d) 1000X.	83.
II.7.6.	Microreactions on the shear lip of 2090-T81 specimens from 10 kg·m GOX tests. (a) 1000X, (b) 3000X, (c) 1000X, and (d) 50X.	84.
II.7.7.	Microreactions on the top specimen surface (a) 100X, and shear lip (b) 3000X, and (c) 1500X of WL049-T851 from pressurized LOX tests at 10 kg·m.	86.
II.7.8.	Microreactions in 2219 from pressurized LOX and GOX tests on shear lip (a) T851, 75X and (b) T87, 200X, at bottom of shear lip (c) T87, 500X, on back (d) T87, 1000X, and under striker-pin indentation (e) T87, 5X and (f) T851, 1000X.	89.
II.7.9.	Number of observed reactions vs. optical power of the observation.	91.
II.7.10.	Minimum absorbed energy to cause a reaction vs. minimum absorbed energy to cause splitting.	95.

LIST OF TABLES

Table  
Number

II.3.1.	Inventory of Al and Al-Li Plate Material.	5.
II.3.2.	Compositions of Al-Li Alloys and Alloy 2219, wt%.	6.
II.3.3.	Second Phase Particle Counts on Al-Li Alloys and Alloy 2219.	10.
II.4.1.	Taguchi Test Matrix Variables.	17.
II.4.2.	Average 304 SS Calibration Disk Results, Using an Open Cup Machine and an Impact Energy of 10 kg·m (72 ft·lb).	19.
II.4.3.	Average 304 SS Calibration Disk Results from WSTF Using an Open-Cup Machine and an Impact Energy of 10 kg·m (72 ft·lb).	20.
II.4.4.	304 SS Calibration Disk Results Using an Open-Cup Machine, in an Ambient Environment with an Impact Energy of 10 kg·m (72 ft·lb) at WSTF.	20.
II.4.5.	Average 2090-T81 Comparison Test Results at WSTF Using an Open-Cup Machine; and at MSFC and SSFL Using a Pressurized Machine with an Impact Energy of 10 kg·m (72 ft·lb).	22.
II.4.6.	Average 2090-T81 Comparison Test Results at WSTF Using a Pressurized Machine with an Impact Energy of 10 kg·m (72 ft·lb).	22.
II.5.1.	Thermal Transient Parameters.	39.
II.5.2.	Results of Open-Cup Mechanical Impact Tests in LOX, Ambient Pressure.	44.
II.5.3.	Summary of Physical Measurements: On Specimens in LOX, Ambient Pressure.	47.
II.5.4.	Summary of Physical Measurements: Splits and Eccentricity; on Specimens in LOX at Ambient Pressure.	48.
II.5.5.	Results of Pressurized Mechanical Impact Tests.	60.
II.5.6.	Summary of Physical Measurements: On Specimens in LOX and GOX, Ambient and Pressurized Environment.	62.
II.5.7.	Summary of Physical Measurements: Splits and Eccentricity, on Specimens in GOX, LOX, Ambient and Pressurized Environment.	63.
II.5.8.	Penetration Depths and Rebound Heights, Open-Cup and Pressurized Tests.	66.
II.5.9.	Comparison of Specimen Impact Depths: 2090-T81 (12.5-mm plate, 3-mm thick comparison samples).	70.
II.5.10.	Results of Promoted-Combustion Tests from WSTF on Specimens 14.7 cm Long.	71.
II.7.1.	Reaction Frequency.	97.

## II.1. EXECUTIVE SUMMARY

In Part I of this program, Al-Li alloys 8090-T3 and 2090-T81, and Al alloy 2219 (tempers T851 and T37) were tested for compatibility with liquid oxygen using pressurized mechanical-impact apparatuses at two NASA laboratories, Marshall Space Flight Center (MSFC) and White Sands Test Facility (WSTF). Specimens and data from tests at Santa Susana Field Laboratory (SSFL), Rocketyne, on alloy 2090-T81 were supplied by ALCOA. Pressurized mechanical-impact data on alloy WL049-T351 were produced by WSTF. In addition, WSTF conducted open-cup mechanical-impact and promoted-combustion tests on all of these alloys. Results and analyses of these tests are included as Part I of this report.

In Part II of this program, selected tempers of alloys 8090, 2090, WL049, and 2219 were tested in modified open-cup and pressurized mechanical-impact equipment at WSTF. Drop height (potential energy), pressure, and environment (liquid oxygen, LOX and gaseous oxygen, GOX) were varied in these tests. Additional promoted-combustion tests were also conducted at WSTF.

Reactions, ranging in size from those that could be observed with the naked eye to those that required use of the scanning electron microscope (SEM), were identified in all alloys. Those that require little or no magnifying power to view are labeled macroreactions; those that require the use of optical microscopy or SEM are called microreactions. Al-Li alloys had more macroreactions than 2219; 2219 had more, or an equivalent number of microreactions than each of the Al-Li alloys. Al-Li alloys were superior to 2219 in flammability in the presence of GOX, as measured in the promoted-combustion tests. Therefore, within the ability of the current tests to discern relative compatibility and flammability with LOX and GOX, the Al-Li alloys and 2219 must be judged equally acceptable for Advanced Launch System (ALS) cryogenic tankage.

The mechanical-impact test imparts significant deformation (absorbed) energy to the Al-alloy specimens. Axial compression, radial shear, and circumferential tensile (hoop) stresses are all of the order of magnitude required to fracture the specimen. From these large stresses, most specimens crack internally or fracture (split) inwardly from the perimeter. The minimum absorbed energy needed to induce splitting (tensile failure) in the specimen has been compared to the minimum absorbed energy needed to induce reactions in the specimen. It was found that the minimum energy to induce fracture was less than, or equal to, that required to induce reactions. Therefore, mechanical failure will precede, or usually be attendant with, reactions in oxygen environments.

The discovery that reactions with oxygen occur over a large range of sizes emphasizes an inherent ambiguity in the definition of a reaction in mechanical-impact tests. Current practice of accepting only visual observations leads to inconsistencies (reactions may be overlooked and their observation depends on proper lighting conditions). The size of reactions observed in these tests has not been correlated with in-service performance. Furthermore, we suggest ten modifications to the current NASA NHB 8060.1B standard for mechanical-impact tests in LOX or GOX; these changes would reduce the large disparity in test procedures that exists among laboratories

that conduct these tests. In summary, the definition of a reaction is arbitrary and modifications are needed to ensure closer conformance of testing procedures. For these reasons, it is recommended that the current open-cup and pressurized mechanical-impact, oxygen-compatibility tests not be used as a qualification test for alloys in aerospace applications.

## II.2. INTRODUCTION

The oxygen-compatibility studies reported here are part of a broader National Institute of Standards and Technology (NIST) program to assess new high-strength Al-Li alloys for use in the cryogenic tankage of the Advanced Launch System (ALS). This program is sponsored by the Air Force Systems Command, Astronautics Laboratory, Edwards Air Force Base, with Bao Nguyen, Task Manager. It is part of the Materials and Processes Validation (3101) of the Structures, Materials, and Manufacturing (3000) portion of the ALS Advanced Development Program.

The purpose of the NIST oxygen-compatibility program has been to assess the relative compatibility with liquid and gaseous oxygen of high-strength Al-Li alloys and alloy 2219 for use in ALS cryogenic tanks. Program objectives were: (1) to provide well-characterized specimens of state-of-the-art commercial alloys for LOX (liquid oxygen) and GOX (gaseous oxygen) measurements at either of the qualified NASA test laboratories, MSFC and WSTF; (2) to study the roles of intrinsic material variables, such as fracture properties, chemistry, and second phase particles, on ignition characteristics; and (3) to assess the extrinsic test variables, such as impact energy, pressure, temperature, and specimen size, orientation, and specimen location (within the specimen cup or holder) on reaction tendencies.

This is our final report on oxygen compatibility of Al-Li alloys. Our interim report (original date of issue January 5, 1990) is being reissued along with this report, and is referred to as Part I in this report. (Some typographical errors have been corrected in the reissued report, dated May 25, 1990). Cryogenic mechanical and thermal property data located in Sections I.3.3. and I.3.4. of Part I are incorporated and updated in NIST reports, "Comparative Measurements of Cryogenic Mechanical Properties of Al-Li Alloys and Alloy 2219,"<sup>2</sup> and "Review of Cryogenic Mechanical and Thermal Properties of Al-Li Alloys and Alloy 2219."<sup>3</sup>

In Part II of this program, alloys 8090-T8771, 2090-T81, WL049-T851 and T651, and 2219-T87, T851, and T37 were tested for compatibility with liquid oxygen using the open-cup and pressurized mechanical-impact facilities at WSTF. Both the open-cup and pressurized tests were carried out with equipment that had been modified as a result of the investigations in Part I. In the present test series, drop height (potential energy) was varied from 2 to 10 kg·m, for both LOX and GOX environments, and pressure ranged from ambient to 0.67 MPa (100 psi). Additional promoted-combustion tests were conducted at WSTF.

Analyses and interpretive studies of the WSTF data and impact specimens were conducted at NIST-Boulder. Chung-Chu Wan of the Aerospace Corporation has contributed observations on impacted specimens using the scanning electron microscope.

In this report the new series of open-cup and pressurized mechanical-impact data from tests conducted at WSTF are discussed. Conclusions and recommendations are presented that compare the relative compatibility with oxygen of Al-Li alloys to alloy 2219, that associate the energies required for reaction in Al alloys with the energies required for mechanical failure. We suggest that, under current specifications, the mechanical-impact test is not a useful qualification test.

## II.3. MATERIAL CHARACTERIZATION

### II.3.1. Inventory

A list of the alloys, suppliers, dates that alloys were received by NIST, and quantity of material is found in Table II.3.1. This report (Part II) covers compatibility tests on the following alloys: 8090-T8771, 2090-T81, WL049 (T851 and T651), and 2219 (T87, T851, and T37). The 2219-T87 with the lot number 294592 was used for the oxygen compatibility testing, the 2219-T87 with lot number 484881 was used in the mechanical testing reported elsewhere.<sup>2</sup>

### II.3.2. Chemical Composition

The chemical compositions of the alloys, as furnished by the material suppliers,\* are given in Table II.3.2. All compositions fall within the Aluminum Association specifications for each alloy. The WL049 alloy does not have a generic specification at this time, and is commonly termed Weldalite 049TM.\*\*

### II.3.3. Microstructure of the As-Received Materials

The Interim Report (Section I.3.5.) included microstructural characterizations for the 8090-T3, 2090-T81, WL049-T351, and 2219-T851 and T37 alloys. Here, the as-received microstructures of three WL049 tempers [T851 (Lot 1), T851 (Lot 2), and T651] and 2219-T87 are reported. In addition, data on the number and volume fraction of second phase particles for all alloys with T8 tempers are presented.

The microstructures of the WL049 tempers [Figures II.3.1(a,b) and II.3.2(a)] consist of large pancake grains that contain many small recrystallized grains. The pancake-grain sizes in the WL049-T851 (Lot 1 and Lot 2) temper are 3 to 5-mm long and up to 1-mm wide in the rolling plane. The WL049-T651 temper has a smaller pancake-grain size, often less than 1-mm long and 0.5-mm wide in the rolling plane. These materials also differ in recrystallized grain size and second phase particle content. The recrystallized grain sizes for the WL049-T651 and WL049-T851 (Lot 2) tempers were normally less than 10  $\mu\text{m}$ . In the WL049-T851 (Lot 1) temper, areas of recrystallized grains that have sizes greater than 100  $\mu\text{m}$  were observed.

The as-received microstructure of the 2219-T87 alloy and temper has a grain size and morphology similar to that reported for the 2219-T851 and T37 tempers. The grains are slightly elongated in the rolling direction with lengths up to 0.3 mm and widths normally less than 0.05 mm [Figure II.3.2(b)].

\*The analyses of the 2219 alloys were furnished by an independent contractor.

\*\*Trade names are furnished to identify the material adequately. Such identification does not imply recommendation or endorsements by NIST, nor does it imply that the materials identified are necessarily the best available for the purpose.

Table II.3.1. Inventory of Al and Al-Li Plate Material.

Date Received	Supplier	Alloy	Quantity	Plate Dimensions, cm	Lot Number
7/12/89	Kaiser	2219-T851	4	122 x 122 x 1.27	429881
7/12/89	Kaiser	2219-T37	4	122 x 122 x 1.27	486341
8/10/89	ALCOA	2090-T81	1	122 x 244 x 1.27	103301
8/10/89	ALCOA	2090-T81	1	122 x 244 x 1.91	103299
9/22/89	ALCAN	8090-T8771	4	91.4 x 163 x 1.27	3503302B
10/3/89	Reynolds	WL049-T651	4	122 x 122 x 1.27	0387240A
11/14/89	ALCOA	2219-T87	1	30.5 x 30.5 x 1.27	294592
11/27/89	Reynolds (Lot 1)	WL049-T851	1	122 x 122 x 1.27	0387250A
03/09/90	Reynolds (Lot 2)	WL049-T851	1	30.5 x 30.5 x 1.27	9002311A
03/14/90	NASA	2219-T87	4	30.5 x 30.5 x 1.27	484881

Table II.3.2. Compositions of Al-Li Alloys and Alloy 2219, wt%.

Alloy	Ca	Li	Mg	Zr	Si	Fe	Ti	Cr	Zn	Ag	Ni	B	Mn
8090-T871	1.21	2.36	0.68	0.11	0.02	0.06	0.028	0.002	0.04	—	0.004	—	—
2090-T81 12.7 mm	2.70	2.3	0.03	0.12	—	0.08	0.19	<0.00	0.01	—	0.01	<0.0000	<0.00
2090-T81 19.1 mm	2.85	2.3	0.05	0.10	—	0.07	0.13	<0.00	0.02	—	0.01	0.0007	<0.00
WL049-T851 (Lot 1)	4.72	1.28	0.42	0.12	0.02	0.03	0.02	—	0.02	0.35	0.01	—	<0.00
WL049-T851 (Lot 2)	4.36	1.25	0.39	0.14	0.03	0.07	0.02	—	0.02	0.35	<0.01	—	<0.00
WL049-T651	4.72	1.28	0.42	0.12	0.02	0.03	0.02	<0.00	0.00	0.35	0.01	—	<0.00
2219-T87 Lot No. 294592	5.87	—	0.01	0.22	0.07	0.01	0.04	<0.00	—	—	<0.00	—	0.23
2219-T87 Lot No. 484881	5.71	—	<0.00	0.15	0.07	0.02	0.03	0.01	—	—	<0.00	—	0.30
2219-T851	5.71	—	—	0.08	0.04	0.02	0.044	0.18	—	—	0.016	—	0.24
2219-T37	5.72	—	—	0.028	0.04	0.018	0.03	0.02	—	—	<0.00	—	0.22

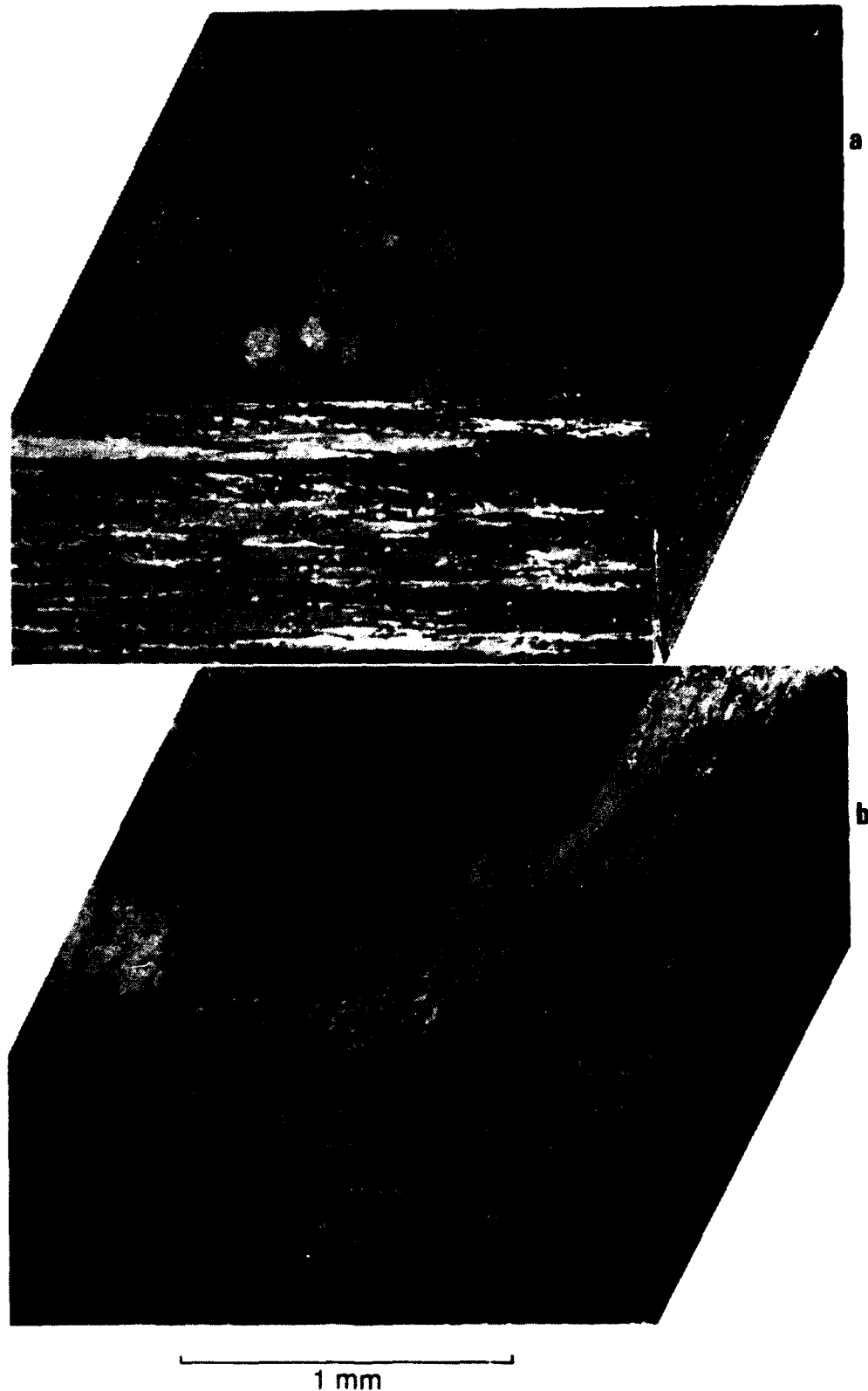


Figure II.3.1. The grain size and morphology of (a) the WL049-T851 (Lot 1) temper and (b) the WL049-T651 temper.

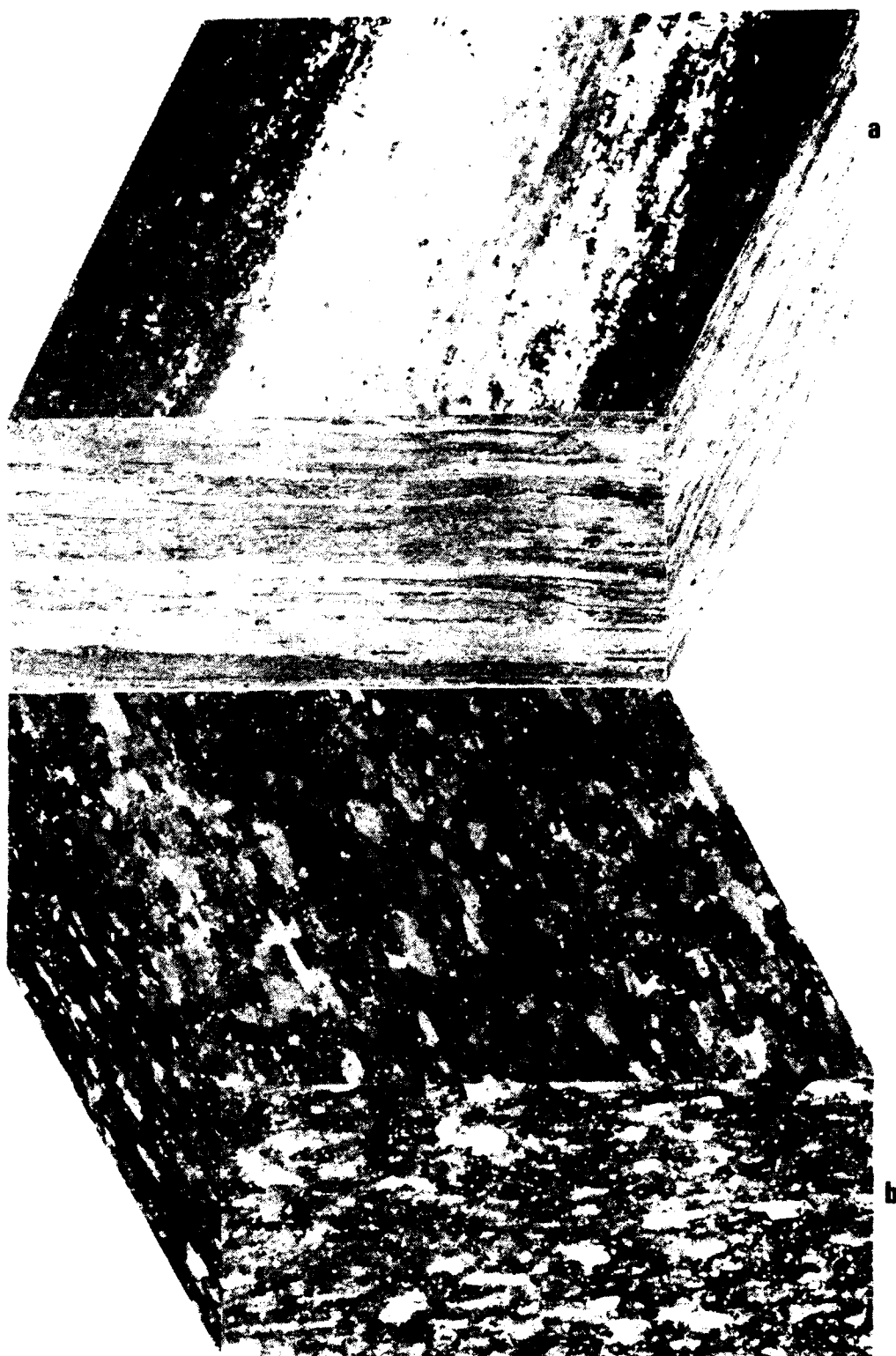


Figure II.3.2. The grain size and morphology of (a) the WL049-T851 (Lot 2) alloy and (b) the 2219-T87 alloy.

The second phase particle counts were made using an optical microscope (400X) equipped with an image analysis system. The procedure used included: (1) polishing to a 1- $\mu\text{m}$  diamond finish and light attack polishing in a dilute NaOH solution and 0.3- $\mu\text{m}$   $\text{Al}_2\text{O}_3$ ; (2) measuring second phase particles located in consecutive fields along paths perpendicular to the rolling direction (100 fields per alloy, 2  $\text{mm}^2$  total area); (3) approximating second phase particle size using the area of each second phase particle measured and assuming a circular shape to calculate a diameter; (4) separating second phase particles into 10 bins based on diameter; and (5) approximating second phase particle volumes using mean diameters for each bin and assuming a spherical second phase particle shape.

The second phase particle counts collected for the alloys with T8 tempers are given in Table II.3.3. Alloy 2090-T81 has the lowest number of second phase particle, followed by the T8151 and T8771 tempers of alloy 8090, WL049-T851 (Lot 2), 2219-T87 and T851, and, finally, WL049-T851 (Lot 1) with the highest number of second phase particle. A ranking by second phase particle volume produces the same order. The distributions in second phase particle sizes broaden as the second phase particle content of the alloys increases; alloys having higher numbers of second phase particle also have more large second phase particle present in their microstructures. The most notable change in second phase particle content for a given alloy type is the reduction in second phase particle content for the second lot of WL049-T851.

We place little significance on the undersized second phase particle counts ( $< 1 \mu\text{m}$ ) because of the various measurement errors possible for these small sizes. The variations in the oversized counts ( $> 9 \mu\text{m}$ ), however, indicate significant differences in the alloys. For example, the frequency of second phase particle with diameters greater than 9  $\mu\text{m}$  is highest for the 2219 alloys. The values for total second phase particle count and volume, reported in Table II.3.3, do not include data from the over- and undersized bins.

Table II.3.3. Second Phase Particle Counts on Al-Li Alloys and Alloy 2219.

Second Phase Particle Size Range. $\mu\text{m}$	Number of Second Phase Particles					
	8090-T8771	8090-T8151	2090-T81	19- <del>mm</del> (0.5-in)	WL049-T851 Lot 1 (0.75-in) plate	2219-T87 Lot 2 (Lot No. 294592)
1-2	2,433	1,536	408	736	10,018	4,294
2-3	639	626	460	386	4,772	633
3-4	203	224	190	144	1,452	166
4-5	119	100	82	67	555	75
5-6	49	39	30	37	249	57
6-7	19	11	16	22	154	34
7-8	17	14	9	6	97	17
8-9	11	5	2	2	56	11
Total Count	3,490	2,555	1,697	1,400	17,415	5,287
Total Volume	37,016	29,714	22,876	20,798	216,110	40,795
Undersized*	6,358	2,496	2,998	766	9,000	8,913
Oversized††	12	19	4	0	68	17

\*Inclusion size  $< 1 \mu\text{m}$

††Inclusion size  $> 9 \mu\text{m}$

## II.4 EXPERIMENTAL PROCEDURES

### II.4.1. Impact Specimen Preparation

#### II.4.1.1. Test Specimen Machining and Surface Finish

Test specimens were machined as specified in NASA NHB 8060.1B<sup>1</sup> to a 1.6-mm (1/16-in) thickness. Specimen diameter was 17 mm (11/16 in). The specimens were machined from alloys 8090-T8771, 2090-T81, WL049 (T851, and T651), and 2219 (T87, T851, and T37). All specimens were machined at WSTF and had a surface finish in the 16-20- $\mu$ in range.

The 8090-T8771 and WL049 specimens tested in the open-cup machine had both a factory side and a machined side. All other specimens tested in the open-cup configuration had both sides machined. Specimens with both sides machined were taken from the center of the plate. Almost all specimens tested in the modified pressurized machine had both a factory side and a machined side. The one exception was that both sides of the 2219-T87 alloy tested at 6-kg·m impact energy were machined. In both the open-cup and pressurized testing, a machined surface was always impacted by the striker pin (i.e., the factory side, when present, was down against the cup or anvil).

#### II.4.1.2. Specimen Cleaning Procedure

The machined specimens were cleaned according to NASA NHB 8060.1B,<sup>1</sup> "Flammability, Odor, and Outgassing Requirements and Test Procedures for Materials in Environments That Support Combustion." A copy of the preface of that document and a portion of paragraph 418, Test 13, relating to specimen cleaning, are given in Appendix I.A.

### II.4.2. Mechanical-Impact Tests in the Modified Open-Cup Machine

#### II.4.2.1. Equipment and Procedures

The WSTF uses an open-cup mechanical-impact machine previously described in Part I this report (I.4.2.1.). However, results of Part I of this program indicated significant disparities in absorbed energies between the WSTF ABMA open-cup test machine and the MSFC pressurized machine in a LOX environment. The indentation depths of the 3-mm (1/8-in) specimens of alloy 2090-T81, tested at WSTF at 10 kg·m (72 ft·lb) were approximately 50 to 70 percent less than the impact depths of the same alloy tested in the MSFC pressurized machine at the same potential-energy level. (See Tables I.5.10 and I.C.3). Because Part I of the oxygen-compatibility program demonstrated that reaction sensitivity in Al alloys is a function of absorbed impact energy, NIST requested that WSTF deviate from their standard procedure by substituting a Ni-based alloy (Inconel 718\*) specimen cup for the Al-alloy specimen cup. (The Al-alloy at WSTF is 5052-H32.) It was

\*Trade names are furnished to identify the material adequately. Such identification does not imply recommendation or endorsements by NIST, nor does it imply that the materials identified are necessarily the best available for the purpose.

assumed that the Al-alloy cup was either absorbing a significant amount of the plummet energy or contributing to the low stiffness of the support system. The NASA NHB 8060.1B<sup>1</sup> and ASTM D2512<sup>4</sup> both specify the use of an Al-alloy cup. However, for the remainder of this program, the Al-alloy cup and stainless-steel insert were replaced by a Ni-based alloy cup. Figure II.4.1 indicates the differences, in both materials and dimensions, between the two cup arrangements. There were no other changes in the equipment or procedures for the open-cup tests, except that plummet and striker-pin assembly rebound heights were measured and recorded, usually for at least half of the impacts.

Procedures for open-cup tests were described in Part I, Section 4.2.1. Some additions to those descriptions follow. Flashes in the open-cup test machine are monitored visually at time of impact by the test technician and by videotaping the impact and replaying the videotape. The videotape shows more than the technician can see. Monitoring of the LOX level was discussed in Section I.4.2.1. Temperature at the specimen cup is not monitored with a thermocouple as it is during the pressurized tests.

#### **II.4.2.2. Materials**

Four Al-Li and Al alloys, of various tempers, were supplied to WSTF for open-cup oxygen-compatibility evaluation. The Al-Li alloys were 8090-T8771, 2090-T81, and WL049 (T851 and T651). The Al alloy was 2219 (T87, T851, and T37). All alloys were machined to 1.6-mm (1/16-in) thickness. Alloy 2090-T81, from the 12.7-mm (1/2-in) plate, was also machined to a 3-mm (1/8-in) thickness for comparison of absorbed energy with the different specimen cups.

#### **II.4.2.3. Conditions**

The alloys were tested in ambient-pressure LOX. Initially, ten specimens were impacted from each alloy, at 10 kg·m (72 ft·lb), 8 kg·m (58 ft·lb), and 6 kg·m (43 ft·lb). Additional sets of ten specimens were tested at lower energy levels, decreasing by 2 kg·m, until there were two successive energy levels at which no reactions occurred. After these tests to establish thresholds were completed, additional sets of ten tests were run on selected alloys above threshold, resulting in some final sets of 20 tests.

### **II.4.3. LOX and GOX Impact Tests in the Modified Pressurized Impact Machine**

#### **II.4.3.1. Equipment and Procedures**

The pressurized mechanical-impact test machine at WSTF is designed to expose specimens to mechanical impacts in the presence of LOX or GOX at pressures from 0 to 69 MPa (0 to 10,000 psi). The unmodified WSTF pressurized machine is described in Section I.4.3.1. of this report. Table I.5.10 (Part I of this report) shows that alloy 2090-T81, in a specimen thickness of 3 mm (1/8 in) from 12.5-mm (1/2-in) plate, had an average penetration depth of 0.08 mm (0.0032 in) when impacted in the WSTF pressurized machine at 10 kg·m (72 ft·lbs). In the MSFC pressurized test machine the same alloy had an average impact depth of 0.37 mm (0.0145 in) when impacted at the same potential-energy level. It was apparent that differences in the two test machines resulted in very different amounts of energy absorbed by the specimens.

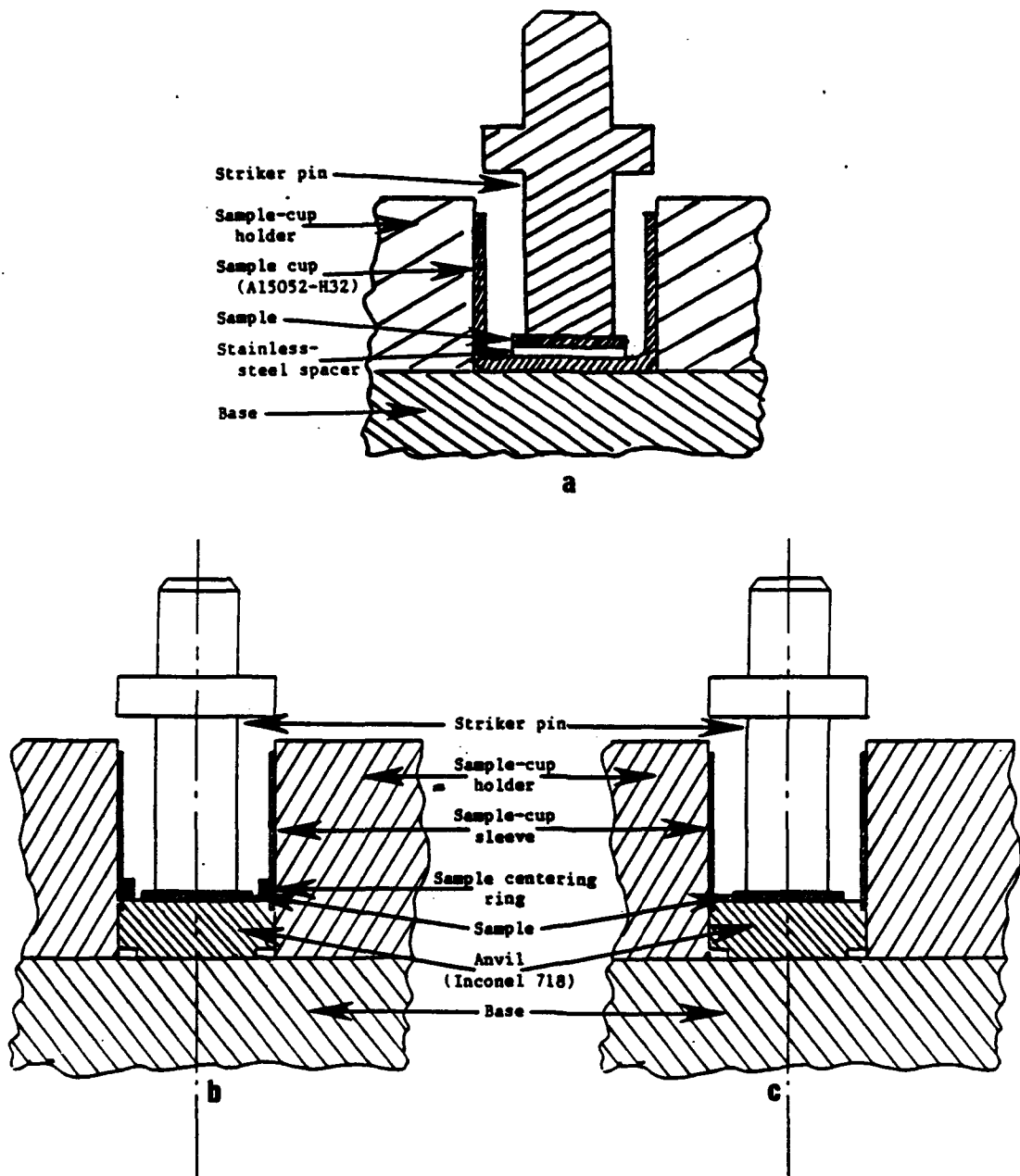


**Figure II.4.1.** Schematics of the original open-cup test machine (a) and the modified open-cup test machine (b) with the specimen centering ring and without (c).

For Part II of this program, the WSTF pressurized test system was modified to increase energy absorbed in the specimen. In cooperation with NIST, WSTF made modifications on an auxiliary pressurized tester to examine the effects of several design features on the absorbed energy of the specimen. The stiffness of the system was considerably increased. Figure II.4.2 shows the initial design of the WSTF pressurized test machine. The long, slender striker pin, the counterload chamber seals, the anvil-nut design and the pedestal base were all reviewed as the new design was developed.

The resulting modified pressurized-machine configuration is shown in Figure II.4.3. The modifications included: replacing the long slender striker assembly with a shorter, larger diameter striker pin and improving pressure-chamber alignment; eliminating the counterload assembly; replacing the threaded anvil nut with a slip-fit anvil; replacing the 25-mm (1.0-in) thick baseplate with a 100-mm (4.0-in) thick baseplate; and eliminating the tubular support column. The elimination of the counterload assembly did not have a detrimental effect on the impact depths of the 2090-T81 comparison specimens (see Section II.4.4.).

The modifications resulted in a change in the standard operating procedures normally used by WSTF. The specimen and specimen cup are still pre-cooled, if required, before installation. To install the specimen and specimen cup, the hold-down nuts must first be removed. The pressure chamber is then lifted up off the centering plate. The pre-cooled specimen and specimen cup are placed on the anvil plate. The pressure chamber is lowered onto the centering plate and tightened in place with the hold-down nuts. The striker-pin retainer and striker pin are removed and the specimen cup is filled with LOX through the top of the chamber. The pin and retainer are then bolted back onto the pressure chamber. The temperature of the cup interior is monitored continuously before, during, and just after impact with a thermocouple located in the cup, slightly above the specimen. Leads for the thermocouple pass through the chamber wall. A pressure transducer is used to measure the pressure change inside the chamber. Photocells are used to detect flashes that may occur inside the chamber. To better estimate the amount of energy that is absorbed by the specimen, NIST requested measurements on the plummet rebound heights. These measurements were generally made for at least half of the tests. The other operational procedures are the same as outlined in Part I of this report.

#### II.4.3.2. Materials and Conditions

Three alloys, 2090-T81, WL049-T851, and 2219-T87, were tested in ambient and pressurized LOX and GOX environments. A Taguchi test matrix was used in this program in an attempt to evaluate the effect of impact energy, pressure, and alloy type on reaction sensitivity. (See Appendix II.A., "Taguchi Matrix Analysis," for an explanation of how the matrix was derived.) The Taguchi test matrix, shown in Table II.4.1, was run in a random sequence, with all GOX tests run first, followed by the LOX tests. Three energy levels, 10, 8, and 6 kg·m (72, 58, and 43 ft·lb), and three pressure levels, 0.69, 0.35, and 0.10 MPa (100, 50 and 14.7 psi) were used in this matrix.

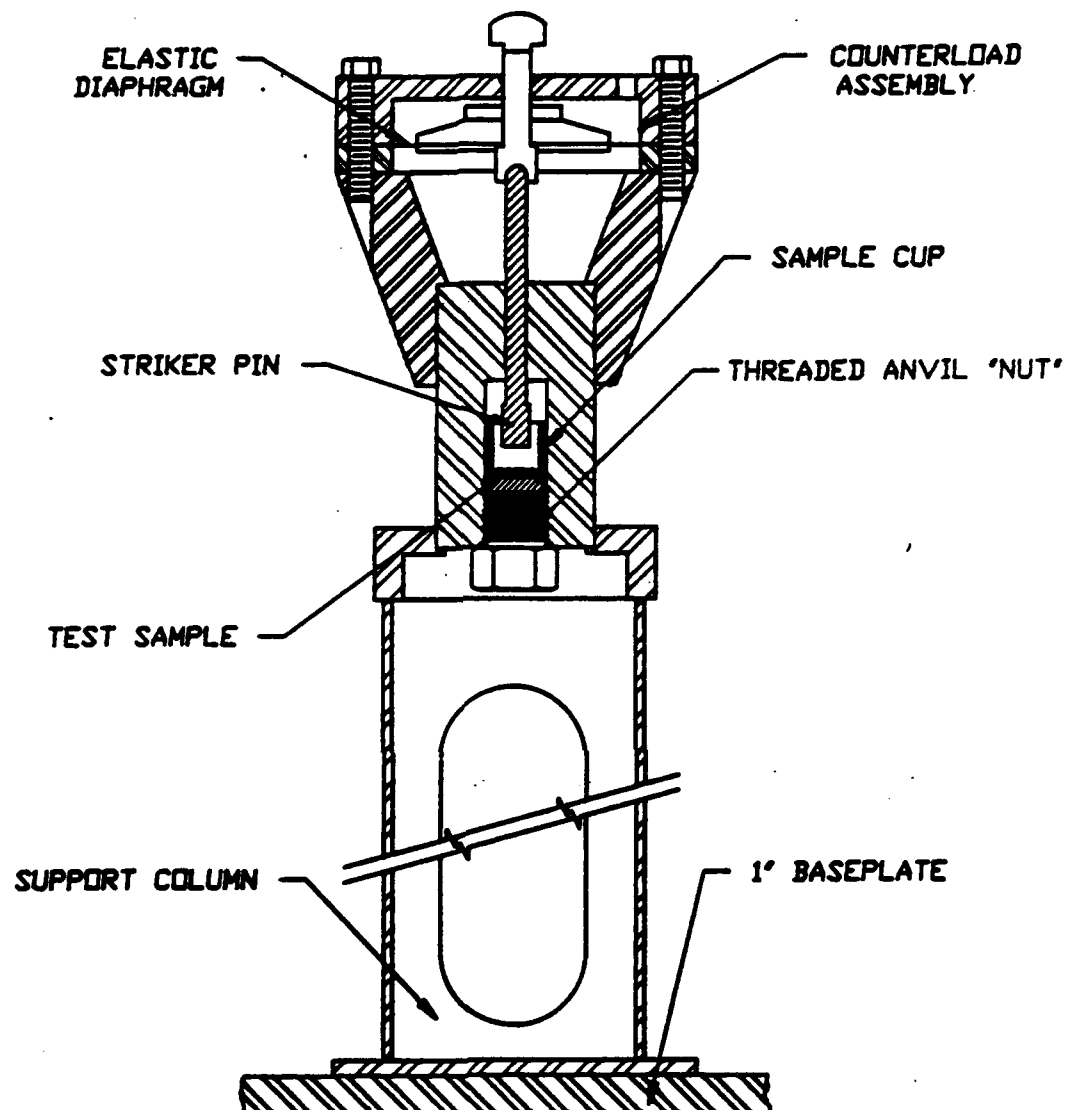
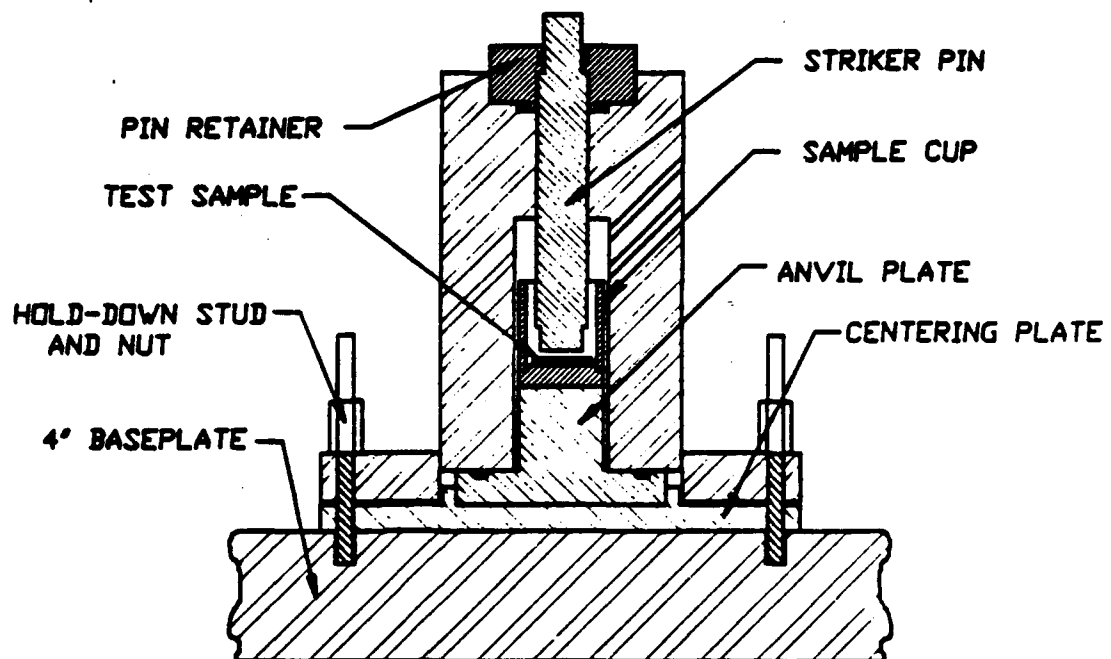


Figure II.4.2. Standard WSTF pressurized test machine. (Figure by M. Rucker, WSTF.)



MECHANICAL IMPACT TEST  
MODIFIED CONFIGURATION  
(NOT TO SCALE)

SUMMARY OF MODIFICATIONS

- REPLACED 1" BASEPLATE WITH 4" BASEPLATE
- ELIMINATED SUPPORT COLUMN
- REPLACED THREADED ANVIL NUT WITH SLIP-FIT ANVIL
- ELIMINATED COUNTERLOAD ASSEMBLY
- SHORTER STRIKER PIN HAS LARGER MAJOR DIAMETER
- IMPROVED ALIGNMENT
- QUICK-RELEASE PIN RETAINER

Figure II.4.3. Modified WSTF pressurized test machine. (Figure by M. Rucker, WSTF.)

Table II.4.1. Taguchi Test Matrix Variables.

Sequence Number	Variables				
	Pressure, MPa (psi)	Energy, kg·m (ft·lb)	Alloy	Environment	
1	Ambient	10 (72)	2219-T87	LOX/GOX	
2	Ambient	8 (58)	2090-T81	LOX/GOX	
3	Ambient	6 (43)	W049-T851	LOX/GOX	
4	0.35 (50)	10 (72)	W049-T851	LOX/GOX	
5	0.35 (50)	8 (58)	2219-T87	LOX/GOX	
6	0.35 (50)	6 (43)	2090-T81	LOX/GOX	
7	0.69 (100)	10 (72)	2090-T81	LOX/GOX	
8	0.69 (100)	8 (58)	W049-T851	LOX/GOX	
9	0.69 (100)	6 (43)	2219-T87	LOX/GOX	

## II.4.4. Calibration of Open-Cup and Pressurized Testers

### II.4.4.1. Open-Cup Tester

Part I of this program demonstrated that the open-cup (ABMA) test machine at WSTF delivered less energy to the specimens than did the MSFC pressurized test machine. For example, Tables I.5.10 and I.C.3 (LOX environment) show that for 3-mm (1/8-in) specimens of alloy 2090-T81, the impact depth from the WSTF open-cup machine is about 50 to 70% lower than that from the pressurized machines at MSFC or SSFL at 3.5 MPa (500 psi). However, calibration tests of the WSTF open-cup apparatus, conducted with a round striker pin on annealed AISI 304 disks in accordance with previously described procedures (Part I of this report, Section I.4.4.), yielded impact depths in reasonable agreement with the Bransford et al.<sup>5</sup> report. This report compared the impact machines at WSTF, MSFC, and SSFL, and showed that similar impact depths were obtained with the MSFC open-cup or pressurized machines, and the WSTF open-cup machine at least at ambient temperatures (see Figures 15 and 25 of that report). Table II.4.2 shows that the penetration depth measured at ambient temperature at WSTF was very close to that reported by Bransford et al. and was about 4% higher than at MSFC and SSFL. Calibration-disk thickness was 8.9 mm (0.350 in) for all tests. All facilities showed an analogous decrease in penetration depths, compared to ambient conditions, when tests were done in LOX. This effect was discussed in Part I of this report (see Section I.8.5.). To examine any possible effect from the flat-bottomed striker pin actually used in the impact tests, in contrast to the round-bottomed pins used in calibration tests, a series of tests was conducted with flat pins. Impact-depth results were comparable, considering the changed geometry, and the effect of temperature was also comparable (Table II.4.3).

These calibration tests were done without the specimen cup in accordance with previous calibration procedures. Since the actual tests on Al-Li and Al alloys were run with Al-alloy specimen cups at WSTF, the possibility that the cup decreased the amount of energy available for absorption by the specimen was then investigated. Bransford et al.<sup>5</sup> had previously examined the effect of an Al-alloy cup in the SSFL ABMA tester at only ambient temperature (see Figures 11 and 12 of that report and the last two entries in Table II.4.2). For calibration specimens of annealed AISI 304 stainless-steel disks (R<sub>B</sub>80), very little difference in the impact depth (obtained from the impact diameter made by a rounded striker pin) was observed when testing with and without the Al-alloy cup. Table II.4.4 shows our recent calibration tests with similar 304 disks. The Bransford results were confirmed for the WSTF open-cup machine, except that a slight decrease of 4% in penetration depth was found in one trial when the 347 stainless-steel insert was in the Al-alloy cup. However, the annealed 304 calibration disk was thick (8.9 mm) in comparison to the 1.6 or 3-mm thick specimens used in this series of impact tests. Also, the disk (R<sub>B</sub>80) was as soft or softer than the T8 temper of most of the Al-Li and Al alloys tested. These alloys had hardnesses ranging from R<sub>B</sub>77 (2219-T87) to R<sub>B</sub>86 (WL049-T851). The 304 disk could absorb much more energy than the alloy specimens being tested. (See Sections II.7.1. and 7.3. for a discussion of absorbed energy of the specimen and its dependence on deformation strain and the stress-strain curve.) This meant that the partitioning of impact energy into absorbed and recoil energy could be considerably different than in the actual tests. The Al-alloy (5052-H32) cup was also considerably softer (R<sub>B</sub>16) than the specimens. Hence, the thick 304 disk and Al-alloy cup system was not

Table II.4.2. Average 304 SS Calibration Disk Results, Using an Open-Cup Machine and an Impact Energy of 10 kg·m (72 ft·lb).

Facility	Env.	Striker- Pin Tip	Cup/Insert	Average Impact		No. of Specimens
				Depth mm	Depth (in)	
*KSC	LOX	Round	No/No	1.052	(0.0414)	5
*KSC	Ambient	Round	No/No	1.342	(0.0528)	5
*MSFL	LOX	Round	No/No	1.031	(0.0406)	3
*MSFL	Ambient	Round	No/No	1.314	(0.0517)	3
*WSTF	Ambient	Round	No/No	1.366	(0.0537)	6
WSTF	LOX	Round	No/No	1.048	(0.0412)	5
WSTF	Ambient	Round	No/No	1.388	(0.0546)	1
WSTF	Ambient	Round	Yes/No	1.360	(0.0535)	1
*SSFL	Ambient	Round	No/No	1.298	(0.0511)	3
*SSFL	Ambient	Round	Yes/No	1.267	(0.0499)	2

\*Denotes Data from Bransford Report

Table II.4.3. Average 304 SS Calibration Disk Results from WSTF Using an Open-Cup Machine and an Impact Energy of 10 kg·m (72 ft·lb).

Env.	Striker-Pin Tip	Cup	Average Impact Depth,		No. of Specimens
			mm	(in)	
Ambient	Flat	No	0.417	(0.0164)	5
LOX	Flat	No	0.248	(0.0098)	5

Table II.4.4. 304 SS Calibration Disk Results Using an Open-Cup Machine, in an Ambient Environment with an Impact Energy of 10 kg·m (72 ft·lb) at WSTF.

Striker-Pin Tip	Cup/Insert	Impact Depth,	
		mm	(in)
Round	No/No	1.388	(0.0546)
Round	Yes/No	1.360	(0.0535)
Round	Yes/Yes	1.326	(0.0522)
Round	No/No	1.368	(0.0538)

a good model for the actual experimental system in which a Ni-alloy cup with a thicker bottom section was substituted for the Al-alloy cup (Section II.4.2., Figure II.4.1). To avoid these inconsistencies, 3-mm (1/8-in) thick specimens of alloy 2090-T81 were used both as comparison standards (in addition to 304 disks) and to elucidate the effect of the specimen-cup material. Alloy 2090-T81 from 12.5-mm (1/2-in) plate had been tested in the 3-mm thickness at all three laboratories (WSTF, MSFC, and SSFL); this was the reason for selection of this alloy in this thickness as a comparison standard.

Table II.4.5 shows data from the various test facilities on the 2090-T81 alloy machined from 12.7-mm (1/2-in) plate. The asterisked (\*) data were generated and referenced in Part I of this report. Results from the WSTF open-cup tests indicate that specimens impacted in the Ni-alloy cup consistently had deeper penetration depths than those impacted in the Al-alloy cup. Ni-alloy cups had also been used in pressurized tests on similar specimens at MSFC and SSFL. Respectively, the impact depths from these pressurized tests were only 6 and 12% smaller than the WSTF open-cup results. Another result shown in Table II.4.5 is the difference in impact depths between 2090-T81 specimens that were machined from the outside surface (1 machined side, 1 factory side) of the plate, and the interior (2 machined sides) of the plate. Since the impact depths were greater in the specimens located at the outside surface, specimens from the exterior (1 machined side, 1 factory side) were used in further testing. Thus, the predominant number of tests in Part II of this program were run on exterior specimens.

#### II.4.4.2. Pressurized Tester

Major modifications to an auxiliary WSTF pressurized test machine were made to increase the energy absorbed by the specimens to a level equivalent to that in the WSTF open-cup machine. The 2090-T81 3-mm (1/8-in) specimens were used to evaluate absorbed energy of the specimen during the modification process. Factory-side specimens were used in these calibration tests. Final results, given in Table II.4.6, show that the modified WSTF pressurized test machine delivers about 83% as much energy to the specimen as the WSTF open-cup machine does. The uncertainty in measuring the penetration depth of the calibration specimens,  $\pm 0.013$  mm (0.0005 in), is about 3%. Also, Table II.4.6 shows that penetration depths are generally lower at LN<sub>2</sub> and LOX temperatures than at ambient temperatures, as is the case in open-cup calibrations.

Table II.4.5. Average 2090-T81 Comparison Test Results at WSTF Using an Open-Cup Machine; and at MSFC and SSFL Using a Pressurized Machine with an Impact Energy of 10 kg·m (72 ft·lb).

Test Facility	Machine	Pressure, MPa (psi)	Env.	Cup Alloy	Impact Depth, mm (in)	No. of Machined Sides	No. of Specimens
*MSFC	Pressurized	3.45 (500)	LOX	Ni-base	0.368 (0.0145)	1 & 2	17
*SSFL	Pressurized	2.76 (400)	LOX	Ni-base	0.345 (0.0136)	2	20
*WSTF	Open Cup	0.10 (14.7)	LOX	Al-base	0.129 (0.0051)	1 & 2	20
WSTF	Open Cup	0.10 (14.7)	LOX	Ni-base	0.391 (0.0154)	2	5
WSTF	Open Cup	0.10 (14.7)	LOX	Ni-base	0.528 (0.0208)	1	5

\*Denotes data from Part I of this report

Table II.4.6. Average 2090-T81 Comparison Test Results at WSTF Using a Pressurized Machine with an Impact Energy of 10 kg·m (72·lb).

Temperature	Pressure, MPa (psi)	Average Impact Depth, mm (in)		No. of Specimens
		mm	(in)	
Ambient	0.10 (14.7)	0.610	(0.0240)	2
Ambient	0.35 (50)	0.610	(0.0240)	2
Ambient	0.69 (100)	0.716	(0.0282)	3
LN <sub>2</sub>	0.10 (14.7)	0.559	(0.0220)	2
LN <sub>2</sub>	0.35 (50)	0.451	(0.0180)	3
LN <sub>2</sub>	0.69 (100)	0.584	(0.0230)	1
LOX	0.10 (14.7)	0.439	(0.0173)	2

## II.5. EXPERIMENTAL RESULTS

### II.5.1. Fracture and Deformation Modes

The sudden collision of the striker pin with the specimen during mechanical-impact tests produces unique deformation and fracture characteristics in Al-Li alloys and alloy 2219. These are illustrated in Figure II.5.1. The indentation of the striker pin produces compression forces in the specimen under the pin, radial shear forces toward the specimen perimeter outside the indentation of the striker pin, and tensile (hoop) forces around the outer perimeter of the specimen. The tensile forces are produced from the radial specimen plastic deformation that results in lateral specimen expansion. The strain rates are high ( $-3 \times 10^3 \text{ s}^{-1}$ ); therefore, near-adiabatic heating conditions exist (see Section I.7.5.). The general features of the deformation and fracture characteristics of the Al-alloy specimens in this study are discussed below.

#### II.5.1.1. Anisotropic Radial Shear Deformation

Following impact, the specimen experiences axial compression from the top and is constrained on its bottom side by the support cup. The yield stress is exceeded and the axial compression forces produce an indentation from the striker pin in the specimen of between 0.2 to 0.7 mm (0.010 to 0.025 in) for a plummet impact (potential) energy of 8 to 10  $\text{kg}\cdot\text{m}$  (58 to 72  $\text{ft}\cdot\text{lb}$ ). The radial shear forces result from the accommodation of the axial plastic deformation and the constrained lower specimen surface. The forces produced under these impact conditions for isotropic deformation conditions are shown schematically in Figure II.5.1(a). The radial plastic deformation of the specimen is anisotropic and is larger in the rolling (L) direction of the alloy (see Figure II.5.2, for example). A typical difference between the diameter of a specimen (with a concentric striker-pin indentation) in the direction of the anisotropic deformation to the normal direction is 1 mm (0.04 in). Eccentricity of the striker-pin impact indentation with respect to the center of the specimen also results in anisotropic radial shear; more extensive deformation occurs in the specimen area (between the indentation and circumference) that is smallest and, therefore, provides less constraint. The anisotropy of the radial shear forces from eccentricity of the striker-pin impact is illustrated in Figure II.5.1(b).

Since the flow strength in the transverse (T) orientation is less (by about 20 MPa, typically) than in the L orientation, one cannot associate the more extensive plastic deformation in the L orientation (in the radial specimen direction) with reduced flow strength in that direction. Instead, the more extensive deformation in the radial L orientation must be associated with less specimen constraint in the direction of the circumferential hoop forces. The flow strength in the T specimen direction is the constraint that influences radial deformation in the L orientation.

#### II.5.1.2. Shear Lips

The specimen material directly in contact with the perimeter of the striker pin is moving, owing to the radial anisotropic shear deformation. This specimen flow results in the appearance of a shear lip along portions

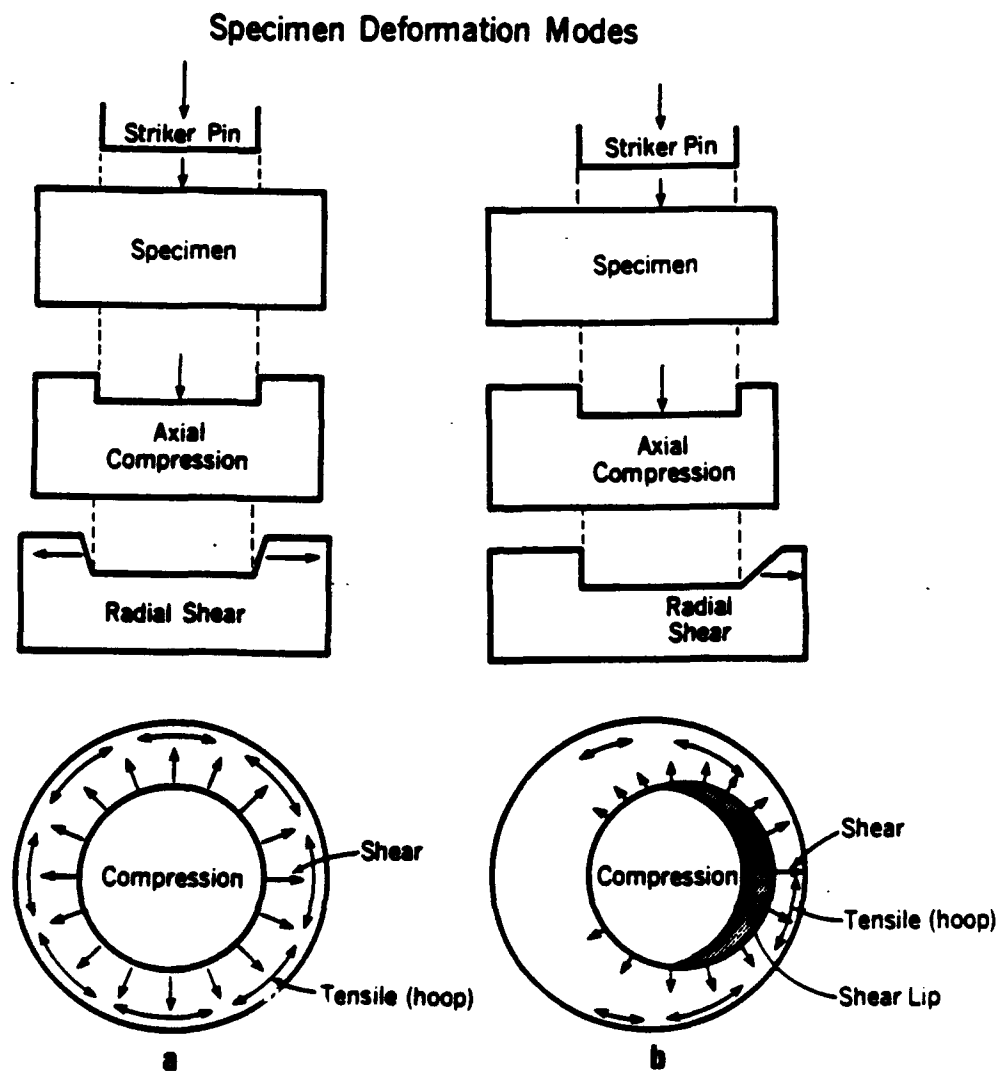


Figure II.5.1. Deformation modes in mechanical-impact test specimen:  
 (a) Concentric strike, (b) Eccentric strike.



Figure II.5.2. Long axis of deformed specimen parallel to rolling direction. Etched WL049-T851, tested in open cup at 6 kg·m. (5X)

of the perimeter of the indentation. This shear lip is illustrated in Figure II.5.3. In Figure II.5.4, the grain structure adjacent to the shear lip in 2219-T37 (10 kg·m, LOX) is shown. Large displacements of grains have occurred during the impact. This is also shown in Figure II.5.5, where the abrupt displacement of grains in alloy 2090-T81 (10 kg·m, LOX) is very obvious. In Figure II.5.4, the very thin layer of small grains on the impact surface suggests either extensive shear with attendant recrystallization or resolidification following local melting.

In Figure II.5.3(b), the microridges that are formed from the rapid intrusion of the striker pin into the specimen are shown. The irregularity of the microridges is controlled by the tolerance on the surface finish and contour of the striker pins. The shear lip is important, since most of the reactions occurred on this interface.

#### II.5.1.3. Striker-Pin Eccentricity

Both axial-deformation characteristics and shear lips are influenced by the amount of eccentricity of the striker-pin indentation with respect to the center of the specimen. If the eccentricity is large, axial deformation is accelerated in the region of the narrow gap between the indentation and the specimen perimeter.

A large eccentricity is illustrated in Figure II.5.3; an almost concentric strike is shown in Figure II.5.2. Distances between the centers of the striker-pin indentation and specimen range up to 2 mm (0.08 in).

#### II.5.1.4. Splits

When the plummet impact (potential) energy is large (~ 6-10 kg·m), the absorbed energy of the specimens is sufficient to impose tensile stresses on the specimen perimeter in excess of the tensile strength of the Al alloys. A crack is initiated along the specimen perimeter and grows inward. The crack usually grows into the region of high compressive forces under the striker-pin. These cracks are referred to as splits in this report, since they tend to separate the specimen into two regions. Typical splits for 2090-T81, WL049-T851, and 2219-T87 are shown in Figure II.5.6.

The initiation of the split occurs on the perimeter, in the region of large radial shear deformation (close to the shear lip). The split (crack) tends to propagate parallel to the rolling direction (L). This growth tendency is illustrated in Figures II.5.3, II.5.6(a), and II.5.7. All alloys exhibited the similar tendency to crack in the L direction. This is understandable: The fracture toughness in the TL orientation is lower than in the LT orientation for those alloys.

Specimens of 2090-T81 split at room temperature (GOX) at energy levels of 10, 8, and 6 kg·m. Specimens of WL049-T851 and 2219-T87 did not split at 295 K at these absorbed-energy levels. At low temperatures, the micromechanism of split fracture in all WL049 and 2219 tempers was microvoid coalescence. Limited delaminations in the plane of the specimen were observed in WL049-T851. The fracture micromechanism for splitting in 2090-T81 at both temperatures was a combination of intergranular cracking and transgranular shear. SEM photographs of these fracture mechanisms are shown



Figure II.5.3. Extensive shear lip (lower, right-of-center) in 2090-T81, tested in GOX at ambient pressure.(5X) Shear lip in 2090-T81, tested in GOX, ambient pressure (a) lip at lower, right-of-center.(5X) (b) microridges on lip formed by friction between striker pin and metal. (500X)



Figure II.5.4. Grain structure beneath shear lip of 2219-T37  
(10 kg·m, LOX). (100X)

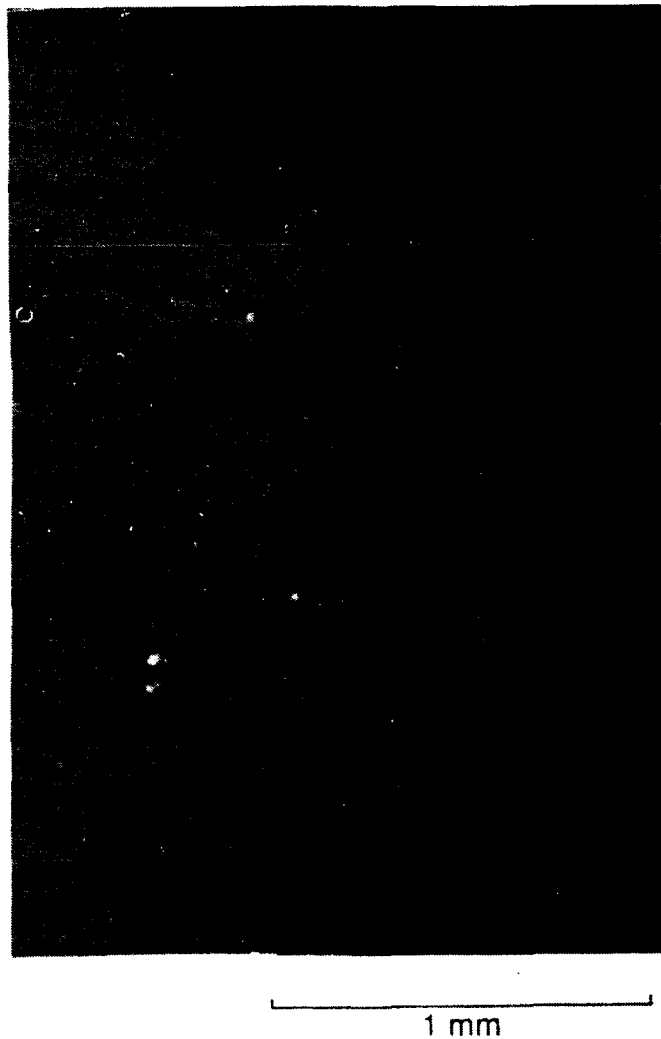


Figure II.5.5. Grain structure adjacent to shear lip and indentation in 2090-T81 (10 kg·m, LOX).

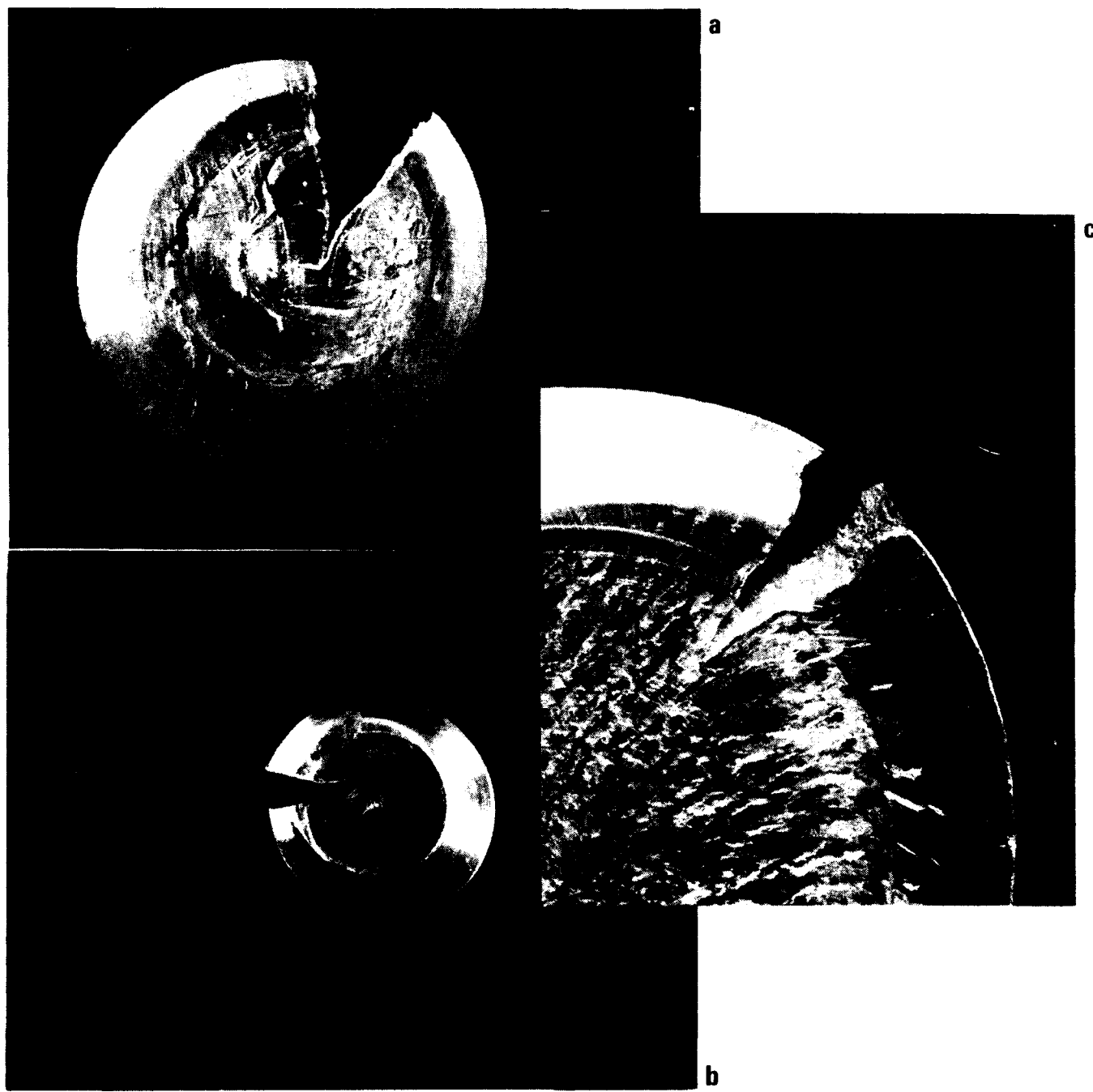


Figure II.5.6. Typical splits extending under the striker-pin indentation for (a) alloy 2090-T81, open-cup LOX, 6 kg·m; (b) WL049-T851, open-cup LOX, 10 kg·m; (c) 2219-T87, open-cup LOX, 10 kg·m.



Figure II.5.7. Crack growth along L orientation in 2090-T87 at  
(a)  $10 \text{ kg}\cdot\text{m}$  and (b)  $8 \text{ kg}\cdot\text{m}$  open cup LOX.

in Figures II.5.8 and II.5.9. There are alternate layers of shear followed by intergranular cracking, giving the appearance of a delaminated crack front. At higher magnification the transgranular shear faces are seen to contain evidence for microvoid coalescence on a very fine scale. Intergranular cracking was more prevalent in specimens tested in LOX (90 K), compared to those tested in GOX at room temperature for alloy 2090-T81. This increase of intergranular cracks at low temperatures corresponds to the reduction of SL and ST fracture toughness at 76 K from room temperature. (Refer to "Comparative Measurements of Cryogenic Mechanical Properties of Al-Li Alloys and Alloy 2219.<sup>2</sup>") Intergranular cracking associated with a split in 2090-T81, tested in LOX at 10 kg·m, is illustrated in Figure II.5.10. Quite obviously, the crack prefers to grow in that direction, within the long grain boundaries.

#### II.5.1.5. Cracks

Cracks are found either on the outside diameter of the specimens where the tensile stress is high, in the area of radial shear (plus tensile) deformation between the shear lip and the specimen perimeter, or within the impacted region of high compressive stress. Cracks have been observed in all alloys and are more prevalent in specimens that were impacted at low temperature (LOX). Both inter- and transgranular cracking have been observed. Microcracks in 2090-T81 are shown in Figure II.5.11. In this alloy, as discussed earlier, the cracks always tend to follow grain boundaries. Microcracks are not unexpected in these tests, owing to the large biaxial stress fields (compression/shear or shear/tensile) in many regions of the specimens.

#### II.5.1.6. Adiabatic Shear Bands

Large adiabatic shear bands are observed in the Al-alloy specimens immediately under the striker-pin indentation and under the shear lip. The scale of the adiabatic shearing varies with grain size. In Figure II.5.12, shear bands adjacent to the shear lip are shown for alloys 2090-T81, WL049-T851, and 2219-T87. The shear bands in 2090-T81 are very large and correspond to the size of the grains (1-5-mm long). In WL049-T851 and 2219-T87, the shear-band size is restricted by the grain size.

Shear bands are associated with both localized deformation and heating. In Section I.7.1. (Part I of this report), we estimate that the time of specimen deformation is between  $7 \times 10^{-5}$  and  $1.4 \times 10^{-4}$  s, and that the time for propagation of a thermal transient is  $2.8 \times 10^{-3}$  s. Thus, the establishment of thermal equilibrium lags mechanical equilibrium, leading to local hot spots. This is precisely the condition that produces adiabatic shearing, the process where thermal softening promotes continued local deformation that, in turn, promotes more local heating. The process may be continuous and, thus, lead to local melting. The adiabatic shear bands also lead to localization of excessive deformation; evidence of microcracking has been observed to be associated with these bands, particularly near grain boundaries. We find evidence for microcracking where the shear bands terminate at the grain boundaries.

An argument can be made that Al-Li alloys are expected to have more adiabatic shearing than alloy 2219. In Table II.5.1, typical values of



Figure II.5.8. The characteristic fracture surface of a split of the 2090-T81 open-cup LOX specimen: (a) low-magnification SEM micrograph of the general fracture morphology, (b) local, surface topography.



Figure II.5.9. Transgranular shear and intergranular cracking layers in 2090-T81 specimen impacted at low temperatures (open-cup LOX). (750X)

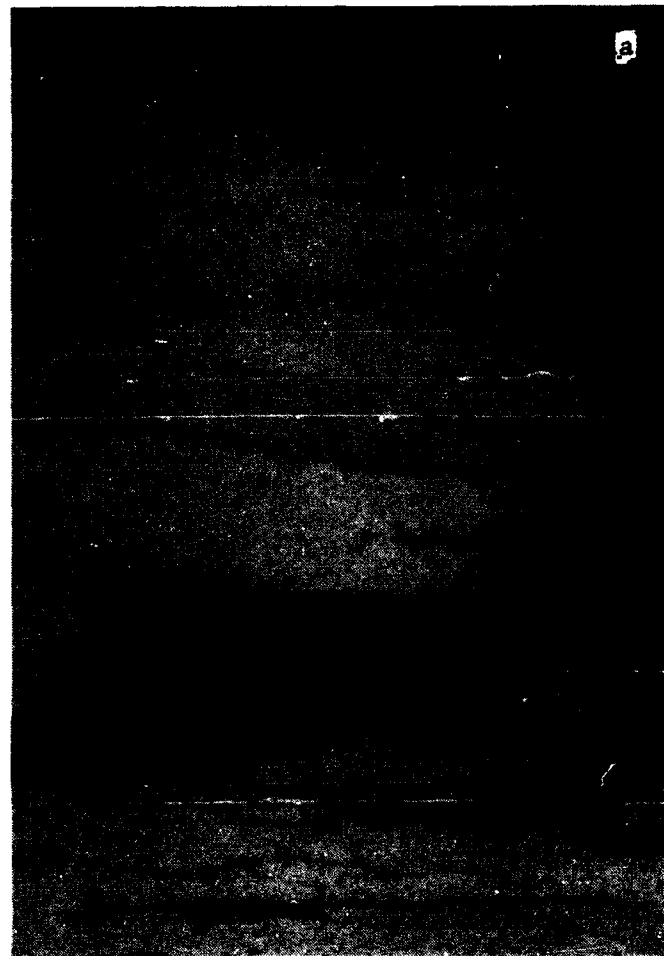


Figure II.5.10. Intergranular microcracking associated with split in 2090-T81 (10 kg·m, pressurized LOX). (100X)



Figure II.5.11. Microcracks in 2090-T81 (a) adjacent to shear lip (8 kg·m, GOX), and (b) in region between bottom of shear lip (indicated by curved "line" on the top) and specimen perimeter (10 kg·m, GOX). (Both at 50X)

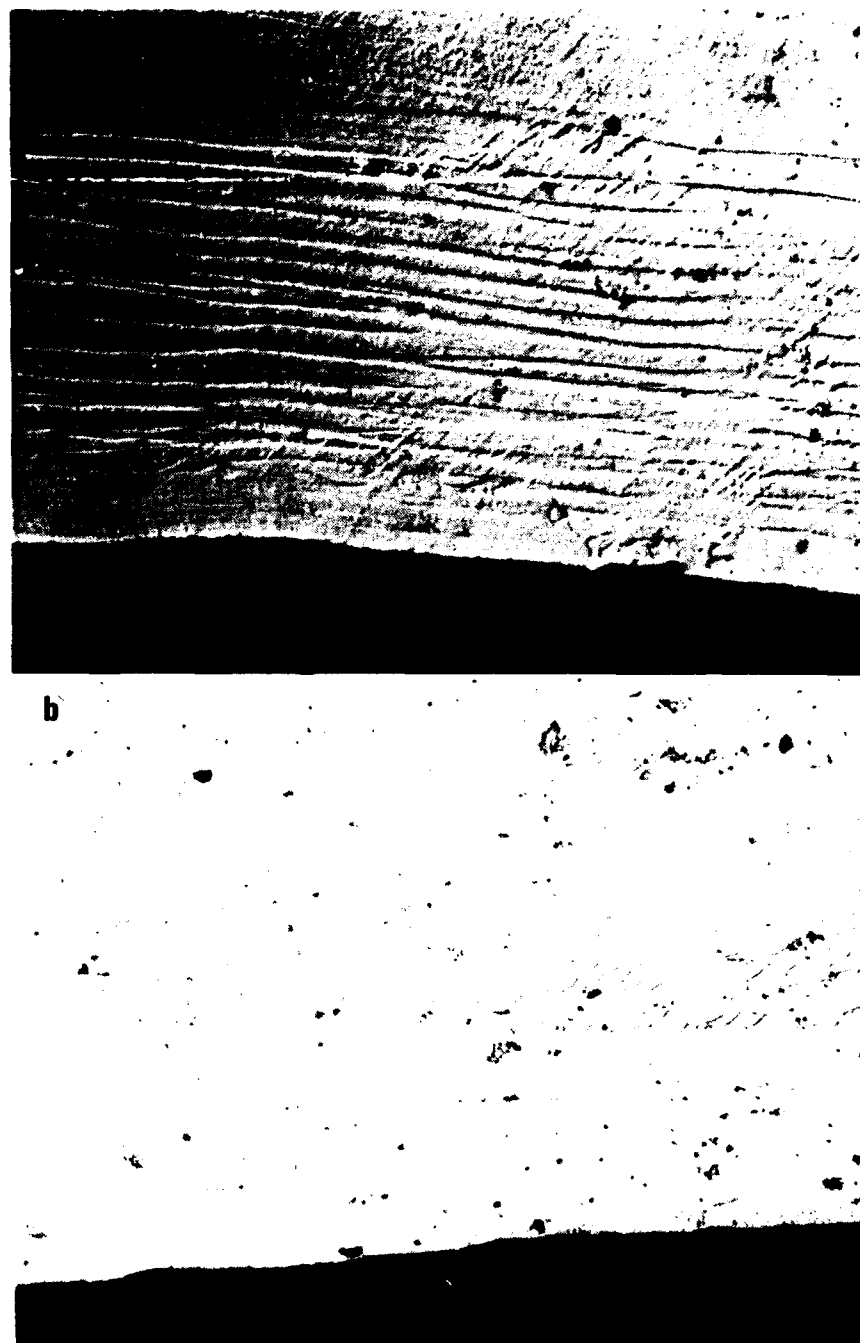


Figure II.5.12. Adiabatic shear bands adjacent to shear lip in (a) 2090-T81 (130X), (b) W1049-T851 (400X), and (c) 2219-T87 (130X). (See next page for continuation of figure.)

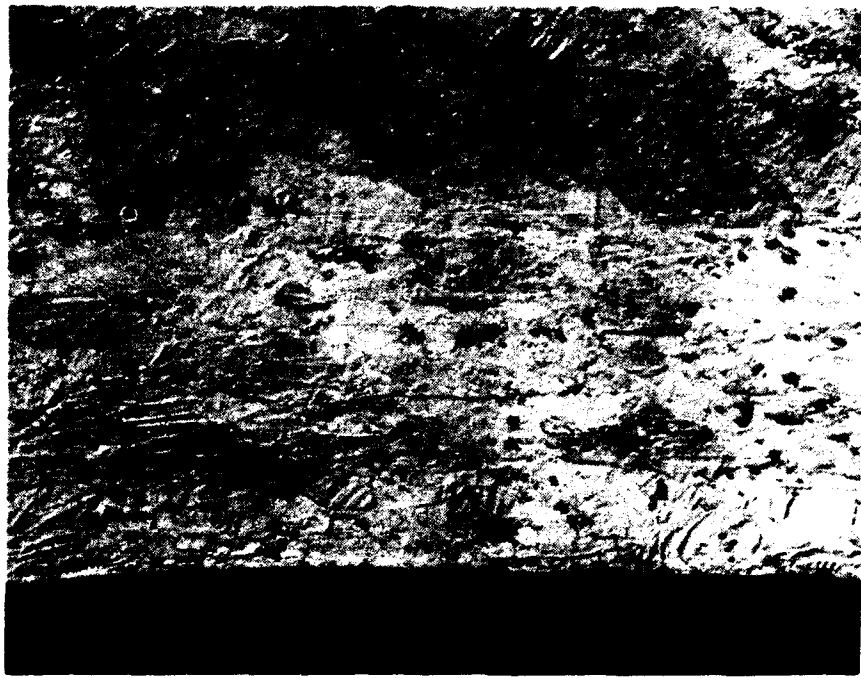


Figure II.5.12. continued

specific heat (C) and thermal conductivity (K) at 90 and 300 K are listed for each alloy. Included, also, in Table II.5.1 are the ratios of  $C \cdot \rho / K$  to permit estimations of the time to propagate a thermal transient ( $t_c$ ) using the relationship

$$t_c = \frac{x_t^2 C \cdot \rho}{K} \quad (5-1)$$

where  $x_t$  is the length of thermal path (assumed constant for both alloys for this discussion) and  $\rho$  is the density (2219 is about 10% more dense than 2090). It is clear from Table II.5.1 that the time to propagate a thermal transient for alloy 2090 is double that of alloy 2219. Therefore, thermal stability should not be achieved as quickly in alloy 2090, and near adiabatic conditions should occur more frequently in this alloy.

Table II.5.1. Thermal Transient Parameters.

Alloy	Specific Heat,C, J/(kg·K)		Thermal Conductivity,K, W/(m·K)		Transient Ratio, $C \cdot \rho / K$ , s/m <sup>2</sup> x 10 <sup>4</sup>	
	90 K	300 K	90 K	300 K	90 K	300 K
2219	520	890	70	125	2.1	2.0
2090	540*	930	32	72	4.4	3.3

\*estimate

#### II.5.1.7. Striker-Pin/Specimen Friction

The friction of the striker pin with the specimen along the perimeter of the indentation contributes to specimen heating. On all shear lips there are small ridges parallel to the direction of the striker pin. Careful SEM examination of these deformation lines indicates considerable fretting. Also, the contour of the deformation ridges closely follows the morphology of the striker-pin head.

#### II.5.1.8. Localized Melting

In Section I.7. (Part I of this report) we estimate that an increase in the local absorbed energy of only a factor of 8 is required to induce local melting, assuming that mechanical equilibrium precedes thermal equilibrium. We argued that testing irregularities, such as concavity of the striker-pin surface and nicks along the striker-pin perimeter could easily result in local increases of absorbed energy of this magnitude.

There is good evidence of localized melting in Al-Li alloys. Localized melting may be identified by two microstructural features: (1) a smooth surface on which no machining nor indications of deformation are present, and (2) a smooth, curved interface contour, as distinct from the abrupt, sometimes straight, interface lines from deformation shear.

In Figure II.5.13(a), a region of local melting on the shear lip is shown; notice evidence for solidification cracking on its surface. In Figure II.5.13(b), the compression surface at the base of the indentor (striker-pin penetration) is shown. The modular-like metal protrusions are indicative of probable melting. Evidence for melting at the base of the shear lip is shown for WL049-T851 in Figure II.5.14. Here the metal has melted; flowed on the base of the indentation, and, in the process, obliterated the specimen machining marks. The irregularities on the shear lip probably represent inclusion-striker-pin reactions in which the inclusions have been partially separated from the matrix. In Figure II.5.15, specimens of 2219-T87 show strong evidence for melting at the base of the shear lip and subsequent flow down and onto the base of the indentation.

## II.5.2. Open-Cup Mechanical-Impact Tests

### II.5.2.1. Initial Report of Reactions Observed by WSTF Staff

The results of open-cup testing in the WSTF modified tester in LOX are summarized in Table II.5.2. Initially, ten specimens were impacted from each alloy, at 10 kg·m (72 ft·lb), 8 kg·m (58 ft·lb), and 6 kg·m (43 ft·lb). Additional sets of ten specimens were tested at lower energy levels, decreasing by 2 kg·m intervals, until there were two energy levels at which no reactions occurred. After this effort to establish thresholds was completed, additional sets of ten tests were run on selected alloys and tempers at energy levels above threshold, resulting in the final sets of 20 tests shown in the table. According to NASA NHB 8060.1B (Paragraph 413),<sup>1</sup> a reaction is "an audible explosion, a flash (electronically or visually detected), evidence of burning (obvious charring) or a major discoloration (due only to ignition rather than other phenomena)." The terms "explosion," "flash," "burning," "charring," and "discoloration" are not further defined or specified in that document. No audible explosions or major discolorations were noted by WSTF personnel in this test series without observation of a flash or a burn. The numbers of flashes and burns are reported in Table II.5.2. Since a burn was always accompanied by a flash, the total number of reactions is equal to the number of flashes. (The one exception is WL049-T651, impacted at 10 kg·m, where one burn did not have a recorded flash.)

All seven alloys tested in LOX had reactions at 10, 8, or 6 kg·m according to the above definitions as interpreted by the WSTF personnel engaged in running these and similar impact tests. The 8090-T8771 alloy reacted at 10 and 8 kg·m, the 2090-T81 alloy reacted at 10, 8, and 6 kg·m, the WL049 alloy, tempers T851 and T651, reacted at 10 and 8 kg·m, and tempers T87 and T851 reacted at 10 kg·m, and temper T37 reacted at 8 kg·m for alloy 2219. The percentage of reactions for all alloys is plotted as a function of impact energy in Figure II.5.16. A correlation of increased reaction percentage with increasing impact energy is observed, except for alloy 2219 where not enough reactions were observed to define a curve on the graph.

The Al-Li alloys all showed charring obvious to the naked eye, whereas the 2219 tempers (T37, T851, and T87) showed no obvious evidence of charring. The 2219 tempers did, however, each flash one to two times when impacted. Thus, the 2219 tempers, by the definitions given above, did exhibit reactions, but the frequency of reactions, on this "macro" scale, was less than for the Al-Li



Figure II.5.13. Regions of localized melting on shear lip (a, 1000X) and on compression surface (b, 500X) of 2090-T87 (10 kg·m, 60X).

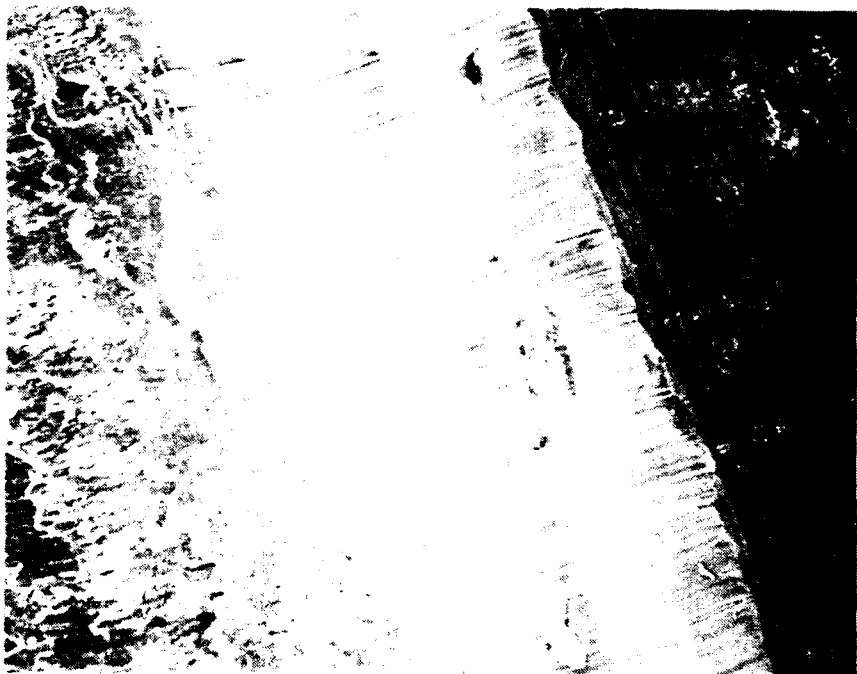


Figure II.5.14. Region of localized melting at the base of the shear lip in WL049-T851 (GOX, 6 kg·m).

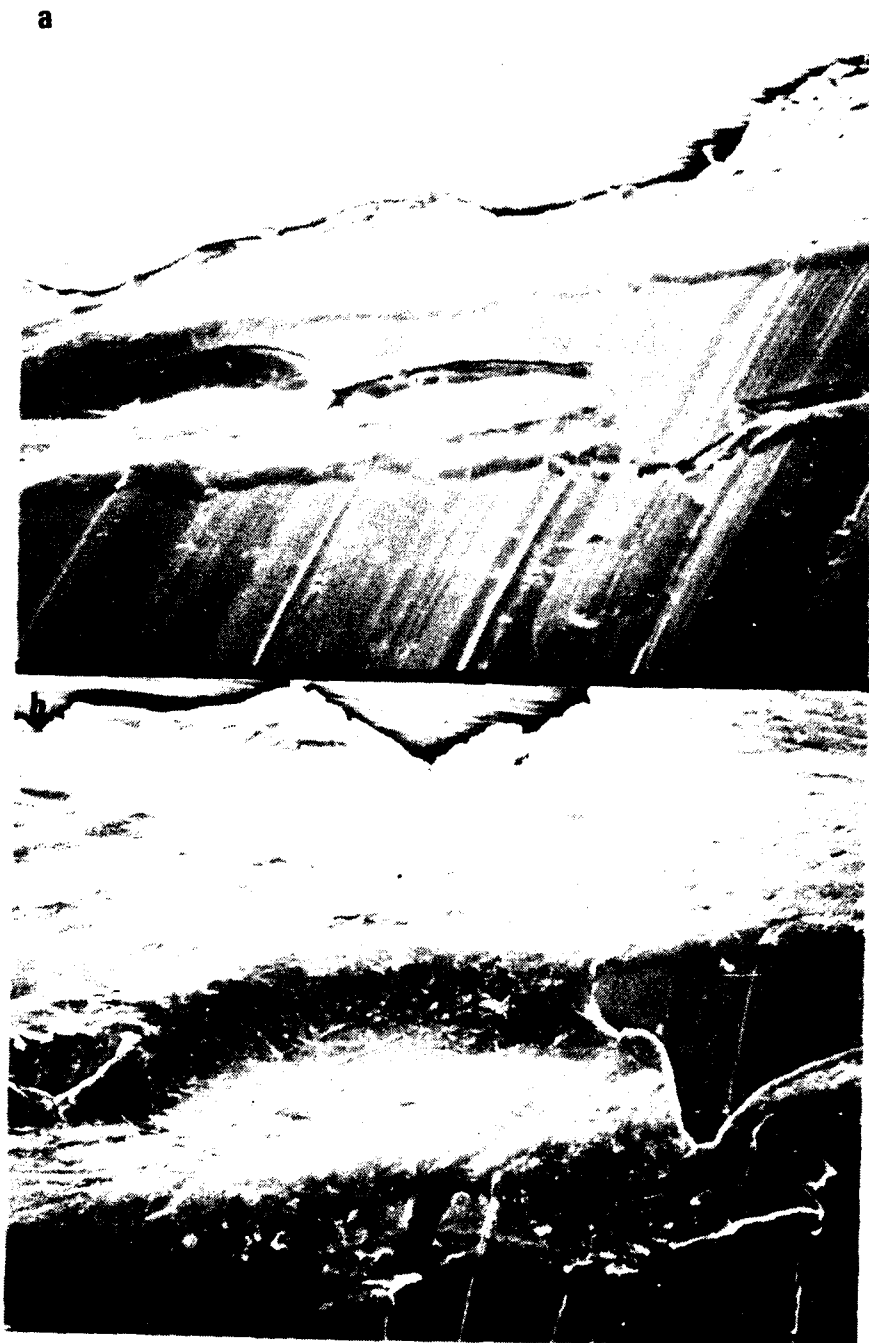


Figure II.5.15. Localized melting in 2219-T851 (10 kg·m, GOX) at the root of the shear lip. In both (a) and (b) the shear lip is on the top, the indentation (with specimen machining markings still showing) on the bottom.

Table II.5.2. Results of Open Cup Mechanical Impact Tests in LOX, Ambient Pressure.

Alloy	Energy, kg·m (ft·lb)		No. of specimens	No. of flashes*	No. of burns	Rebound height, cm (in)	
8090-T8771	10	(72)	20	14	7	16.5	(6.5)
8090-T8771	8	(58)	10	1	1	19.0	(7.5)
8090-T8771	6	(43)	10	0	0	21.6	(8.5)
8090-T8771	4	(29)	10	0	0	18.3	(7.2)
2090-T81	10	(72)	20	11	4	22.3	(8.0)
2090-T81	8	(58)	20	9	3	18.0	(7.1)
2090-T81	6	(43)	20	3	2	16.0	(6.3)
2090-T81	4	(29)	10	0	0	17.8	(7.0)
2090-T81	2	(14)	10	0	0	11.9	(4.7)
WL049-T851	10	(72)	20	9	3	26.7	(10.5)
WL049-T851	8	(58)	20	3	1	27.9	(11.0)
WL049-T851	6	(43)	20	0	0	26.9	(10.6)
WL049-T851	4	(29)	10	0	0	20.1	(7.9)
WL049-T651	10	(72)	20	9	7	29.9	(11.4)
WL049-T651	8	(58)	10	3	1	25.1	(9.9)
WL049-T651	6	(43)	10	0	0	25.9	(10.2)
WL049-T651	4	(29)	10	0	0	22.4	(8.8)
2219-T87	10	(72)	20	1	0	23.4	(9.1)
2219-T87	8	(58)	20	0	0	25.7	(10.1)
2219-T87	6	(43)	10	0	0	23.1	(9.1)
2219-T851	10	(72)	10	1	0	36.1	(14.2)
2219-T851	8	(58)	10	0	0	36.6	(14.4)
2219-T851	6	(43)	10	0	0	28.7	(11.3)
2219-T37	10	(72)	10	0	0	35.1	(13.8)
2219-T37	8	(58)	10	2	0	22.1	(8.7)
2219-T37	6	(43)	10	0	0	25.7	(10.1)
2219-T37	4	(29)	10	0	0	17.0	(6.7)

\*Equivalent to total number of reactions. (Exception: WL049-T651, impacted at 10 kg·m, where one burn did not have a recorded flash.)

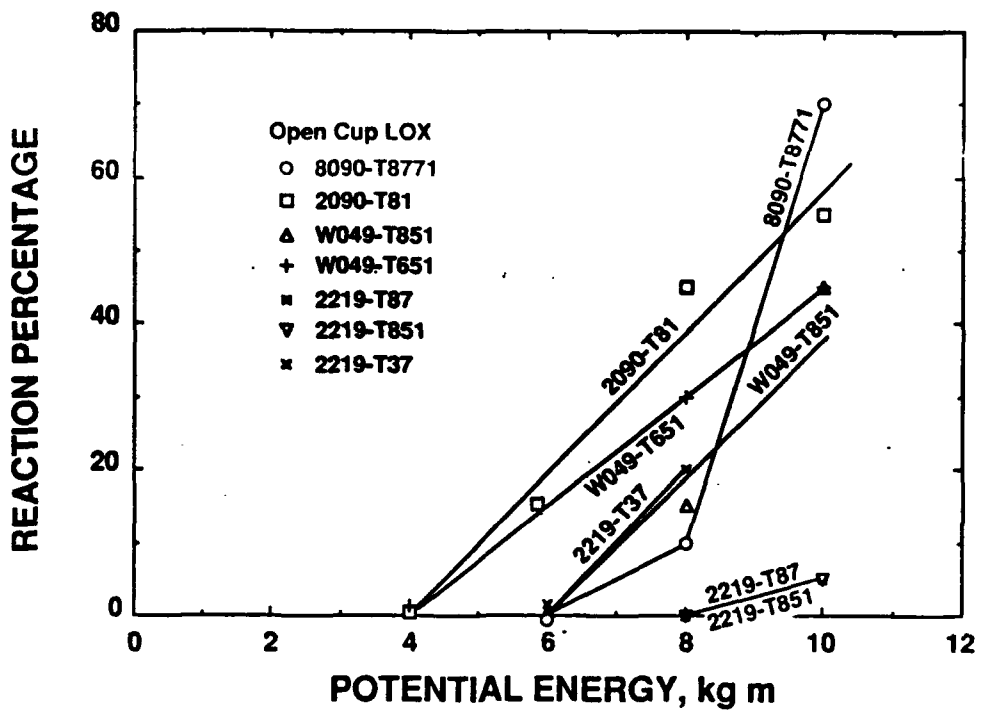


Figure II.5.16. Percentage of reactions vs. potential (impact) energy for open-cup tests in LOX.

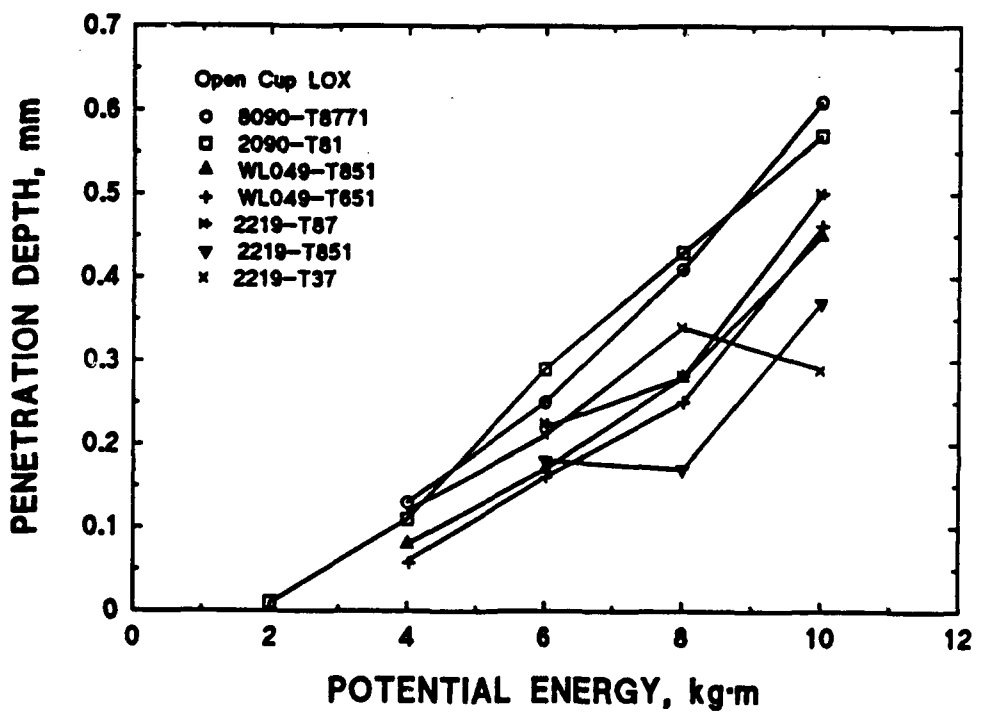


Figure II.5.17. Average penetration depth vs. potential (impact) energy for open-cup tests in LOX.

alloys. The relative frequencies of reaction changed when the impacted specimens were examined more closely under increasing powers of magnification. This finding is reported and discussed in Section II.7.4.2.

Table II.5.2 also shows the average rebound heights for the plummet after the initial impact. This is an average of 3 rebound heights recorded out of each group of ten specimens that were tested. Low rebound height correlates with increased absorption of energy by the specimen at constant impact (potential) energy.

#### II.5.2.2. Physical Measurements on Specimens

The following parameters were measured on each impacted specimen: impact depth (penetration depth), presence or absence of splits and shear lips, and eccentricity of impact. These measurements are presented in Tables II.5.3 and II.5.4. The penetration depth,  $d$ , is the difference between the original specimen thickness and the reduced specimen thickness in the impact area, measured with a micrometer. However, since the original specimen thicknesses were not measured and tracked through the test process,  $d$  was actually taken as the difference between the specimen thickness in the outer, unimpacted area, and the inner, impacted area. (If the thickness of the impacted area was not uniform, an average of measurements at the smallest and largest thickness was used.) The uncertainty in this measurement is estimated about  $\pm 0.05$  mm (0.002 in).

Splitting is defined as a through-thickness fracture of the specimen that usually is associated with gross opening of the crack mouth. See Section I.5.1.2. The shear-lip deformation is described in Sections I.5.1. and I.5.3.2., accompanied by figures that illustrate typical features. Eccentricity of impact is defined as the distance between the center of the specimen and the center of the striker-pin impact area.

The average penetration depth for each alloy is plotted against impact energy in Figure II.5.17. A correlation of increasing penetration depth with increasing impact (potential) energy is observed, as expected, for all alloys. When reaction percentage is plotted against penetration depth (Figure II.5.18), the plot is similar to that for reaction percentage against impact energy. Table II.5.3 presents information on the average penetration depth of specimens that flashed or burned or had splits. The reader is cautioned against drawing erroneous conclusions from Table II.5.3. For example, in the first row of this table, a comparison of the average impact depth (0.61 mm) with the average depth for splits (0.62 mm) at first suggests that splits do not affect impact depth. However, as discussed below, penetration depth and percentage of splits are correlated. The two averages quoted were obtained on virtually the same sets of specimens, since 18 out of 20 specimens had splits.

Table II.5.4 indicates that eccentric loading of the specimen was the rule rather than the exception. The severity of the state of stress is increased with the eccentric loading. The average eccentricity is plotted as a function of penetration depth in Figure II.5.19. No correlation is evident. However, Figure II.5.20, which shows the percentage of splits plotted against the penetration depth, does show a correlation of splits with penetration depth, especially for the Al-Li alloys. The percentage of splits also increases with impact or potential-energy level (Figure II.5.21), as would be expected from the correlation of penetration depth with impact energy. Splits usually occur before

Table II.5.3. Summary of Physical Measurements: On Specimens in LOX, Ambient Pressure.

Alloy	Energy, kg·m (ft·lb)	No. of Specimens	Avg. Impact depth, mm (in)	Avg. depth w/splits, mm (in)	Avg. depth w/flashes, mm (in)	Avg. depth w/burns, mm (in)	No. of Shearlips
8090-T8771	10	(72)	20	0.61 (0.0241)	0.62 (0.0244)	0.63 (0.0248)	18
8090-T8771	8	(58)	10	0.41 (0.0160)	0.45 (0.0178)	0.47 (0.0185)	9
8090-T8771	6	(43)	10	0.25 (0.0097)	0.31 (0.0123)	...	10
8090-T8771	4	(29)	10	0.13 (0.0051)	...	...	5
2090-T81	10	(72)	20	0.57 (0.0226)	0.57 (0.0226)	0.53 (0.0210)	20
2090-T81	8	(58)	20	0.43 (0.0169)	0.43 (0.0169)	0.43 (0.0170)	20
2090-T81	6	(43)	20	0.29 (0.0114)	0.29 (0.0114)	0.35 (0.0138)	19
2090-T81	4	(29)	10	0.11 (0.0042)	0.14 (0.0056)	...	4
2090-T81	2	(14)	10	0.01 (0.0005)	...	...	1
WL049-T851	10	(72)	20	0.45 (0.0177)	0.49 (0.0192)	0.49 (0.0193)	20
WL049-T851	8	(58)	20	0.28 (0.0111)	0.39 (0.0153)	0.30 (0.0118)	18
WL049-T851	6	(43)	20	0.17 (0.0066)	...	...	10
WL049-T851	4	(29)	10	0.08 (0.0033)	...	...	1
WL049-T651	10	(72)	20	0.46 (0.0180)	0.50 (0.0196)	0.51 (0.0200)	20
WL049-T651	8	(58)	10	0.25 (0.0099)	0.34 (0.0133)	0.29 (0.0116)	9
WL049-T651	6	(43)	10	0.16 (0.0064)	...	...	7
WL049-T651	4	(29)	10	0.06 (0.0023)	...	...	2
2219-T87	10	(72)	20	0.50 (0.0196)	0.50 (0.0196)	0.56 (0.0220)	20
2219-T87	8	(58)	20	0.28 (0.0111)	...	...	20
2219-T87	6	(43)	10	0.22 (0.0086)	...	...	2
2219-T851	10	(72)	10	0.37 (0.0145)	0.48 (0.0190)	0.51 (0.0200)	10
2219-T851	8	(58)	10	0.17 (0.0065)	...	...	4
2219-T851	6	(43)	10	0.18 (0.0071)	...	...	6
2219-T37	10	(72)	10	0.29 (0.0114)	...	...	8
2219-T37	8	(58)	10	0.36 (0.0142)	0.51 (0.0199)	0.43 (0.0169)	8
2219-T37	6	(43)	10	0.21 (0.0082)	...	...	6
2219-T37	4	(29)	10	0.12 (0.0049)	...	...	3

Table II.5.4. Summary of Physical Measurements: Splits and Eccentricity; on Specimens in LOX at Ambient Pressure.

Alloy	Energy, kg-m (ft-lb)	No. of Specimens	No. of Splits	Splits		Avg. Ecc., $\bar{\epsilon}$		Avg. $\bar{\epsilon}$ , w/ flashes,		Avg. $\bar{\epsilon}$ , w/ burns,		
				with Flash	with Burns	Eccentricity, $\bar{\epsilon}$ ,	mm (in)	mm (in)	mm (in)	mm (in)	mm (in)	
8090-T8771	10	(72)	20	18	13	0.99	(0.039)	0.97	(0.029)	0.74	(0.017)	
8090-T8771	8	(58)	10	5	1	0.66	(0.026)	0.97	(0.038)	0.76	(0.030)	
8090-T8771	6	(43)	10	1	0	1.07	(0.042)	2.03	(0.080)	...	...	
8090-T8771	4	(29)	10	0	0	1.09	(0.043)	...	...	...	...	
2090-T81	10	(72)	20	20	11	4	1.03	(0.041)	1.03	(0.041)	1.00	(0.039)
2090-T81	8	(58)	20	20	9	3	0.99	(0.039)	0.99	(0.039)	0.76	(0.030)
2090-T81	6	(43)	20	20	3	2	1.04	(0.041)	1.04	(0.041)	0.69	(0.027)
2090-T81	4	(29)	10	4	0	0	1.47	(0.058)	1.73	(0.068)	0.42	(0.017)
2090-T81	2	(14)	10	0	0	0	1.14	(0.045)	...	...	0.51	(0.020)
WL049-T851	10	(72)	20	13	9	3	0.81	(0.032)	0.81	(0.032)	0.76	(0.030)
WL049-T851	8	(58)	20	4	1	1	1.22	(0.048)	1.21	(0.0475)	1.44	(0.056)
WL049-T851	6	(43)	20	0	0	0	0.97	(0.038)	...	...	...	...
WL049-T851	4	(29)	10	0	0	0	1.14	(0.045)	...	...	...	...
WL049-T651	10	(72)	20	12	9	7	1.55	(0.061)	1.35	(0.053)	1.01	(0.040)
WL049-T651	8	(58)	10	2	2	1	0.76	(0.030)	1.02	(0.040)	0.76	(0.030)
WL049-T651	6	(43)	10	0	0	0	1.32	(0.052)	...	...	...	...
WL049-T651	4	(29)	10	0	0	0	0.69	(0.027)	...	...	...	...
2219-T87	10	(72)	20	15	1	0	1.45	(0.057)	1.35	(0.053)	1.01	(0.040)
2219-T87	8	(58)	20	0	0	0	0.91	(0.036)	...	...	...	...
2219-T87	6	(43)	10	0	0	0	0.61	(0.024)	...	...	...	...
2219-T851	10	(72)	10	3	1	0	1.27	(0.050)	1.02	(0.040)	1.52	(0.060)
2219-T851	8	(58)	10	0	0	0	1.52	(0.060)	...	...	...	...
2219-T851	6	(43)	10	0	0	0	0.58	(0.023)	...	...	...	...
2219-T37	10	(72)	10	10	0	0	1.52	(0.060)	...	...	...	...
2219-T37	8	(58)	10	1	1	0	2.03	(0.080)	2.54	(0.100)	...	...
2219-T37	6	(43)	10	0	0	0	0.46	(0.018)	...	...	...	...
2219-T37	4	(29)	10	0	0	0	0.86	(0.034)	...	...	...	...

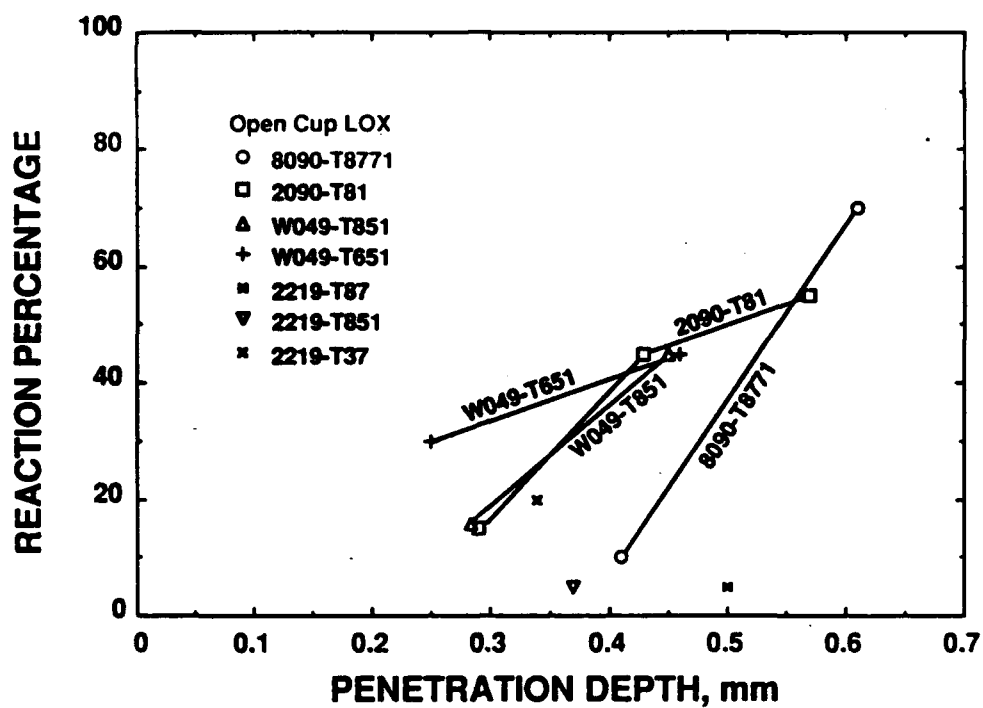


Figure II.5.18. Percentage of reactions vs. average penetration depth for open-cup tests in LOX.

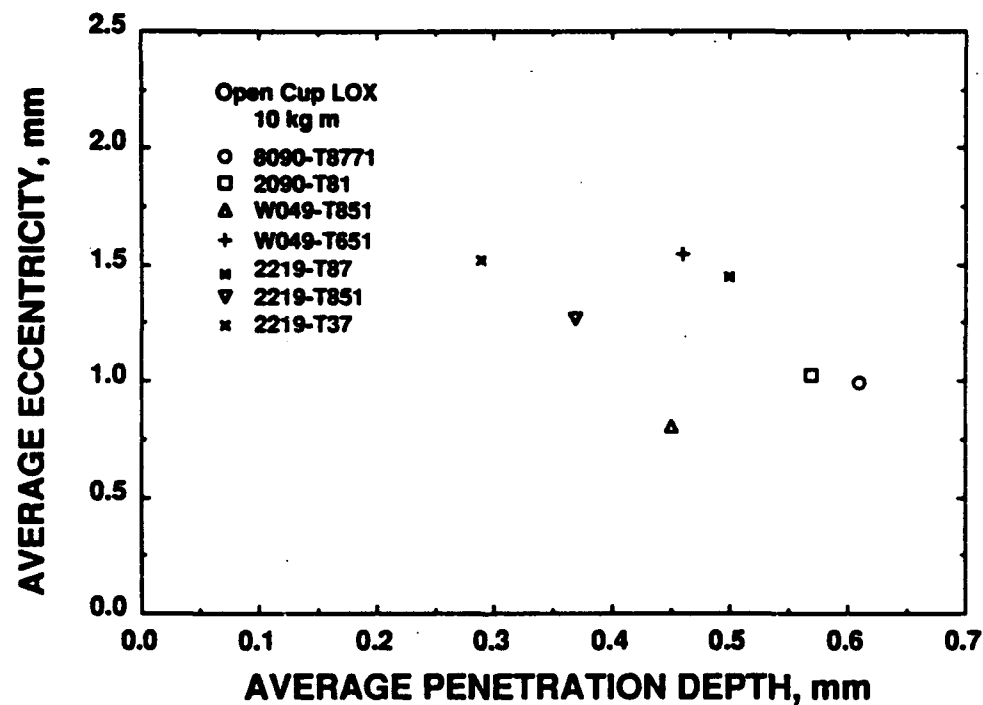


Figure II.5.19. Average eccentricity vs. average penetration depth for open-cup tests in LOX with a potential (impact) energy of 10 kg·m.

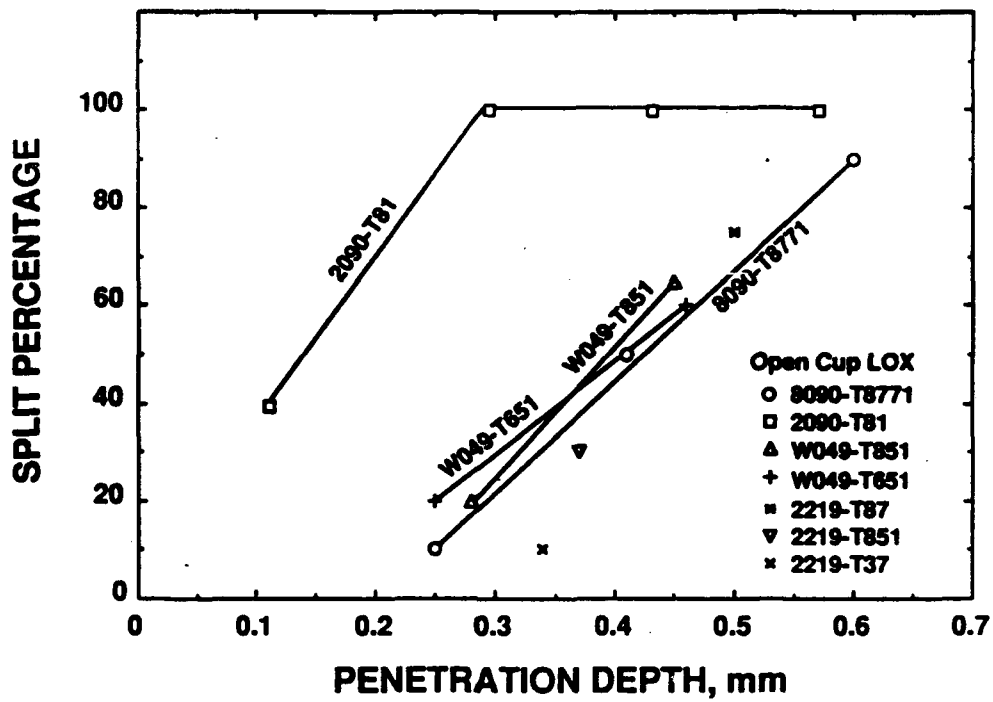


Figure II.5.20. Percentage of splits vs. average penetration depth for open-cup tests in LOX.

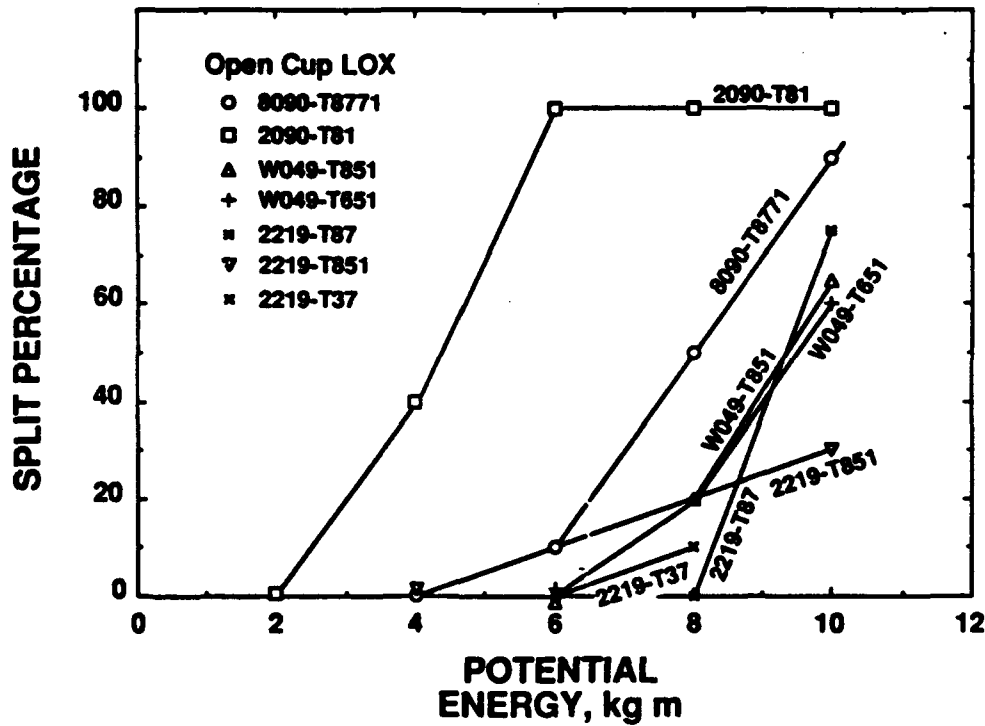


Figure II.5.21. Percentage of splits vs. potential (impact) energy for open-cup tests in LOX.

the deformation process has been completed: an abrupt change in the angle of striker-pin striations is observed on the shear lip of a specimen when a split is present. The splitting event then allows a greater absorption of energy by the specimen, as indicated by the greater penetration depths measured on a set of specimens when the percent of splitting is high. The large number of splits in the present series of tests is in marked contrast with the results in Part I open-cup testing at WSTF. (See Table I.5.1, in which one split and two cracks were noted in 132 tests.)

#### II.5.2.3. Macroreactions in Open-Cup Tests

Macroreactions occurred predominantly on shear lips in the open-cup tests. In 8090-T8771, all macroreactions occurred along the shear lip, as illustrated in Figure II.5.22. In this specimen, there were large reactions on both sides of the split, that extended over a long distance along the shear lip.

In Figure II.5.23, a small reaction in 2090-T81 is present on the shear lip. In Figure II.5.24, one reaction is evident in 2090-T81 that extends along the shear lip and another smaller reaction is evident at the crack below the shear lip. The reaction site at the crack is very rare; it is the only detected reaction found to definitely initiate at a crack site. In 2090-T81, some reactions were stronger, and essentially burned out the material between the shear lip and the specimen perimeter (Figure II.5.25). This reaction started on the shear lip and mostly burned outward.

A reaction in WL049-T851 that initiated in several locations along the shear lip is shown in Figure II.5.26. The features of the striation from the striker pin on the blackened surface and on the specimen at the base of the shear lip suggest that the reaction occurred during the impact and severely deformed the contour of the striker pin. The macroreaction in WL049-T651, shown in Figure II.5.27, is the only initiation site at a split in this series of tests. Many splits were carefully examined, using optical microscopy and SEM, and no other macroreactions and only a few microreactions were observed. Notice in Figure II.5.28 that the blackened oxide flow lines indicate that the reaction origin is along the crack (split).

A reaction at the bottom of a shear lip of alloy 2219-T851 is shown in Figure II.5.29. At the top of the photograph a portion of a split is present. The darkened area on the specimen perimeter is caused by lighting and is not a burned area.

#### II.5.3. Pressurized Mechanical-Impact Tests

##### II.5.3.1. Initial Report of Reactions Observed by WSTF Staff

The results of the pressurized impact testing in the WSTF modified pressurized impact machine are summarized in Table II.5.5. A Taguchi test matrix, shown in Table II.4.1, was used in an attempt to evaluate the relative effects of impact energy, pressure, and alloy type on the reaction probability. There were no recorded "macro" reactions in any alloy tested in GOX under the test conditions of the matrix. In LOX, there were reactions (all burns) in 2090-



Figure II.5.22. Two reactions in 8090-T8771 (10 kg·m, open-cup LOX) that extend over large distances or shear lip. (5X)



Figure II.5.23. Small reaction on shear lip of alloy 2090-T81 (8 kg·m, open-cup LOX). (5X)

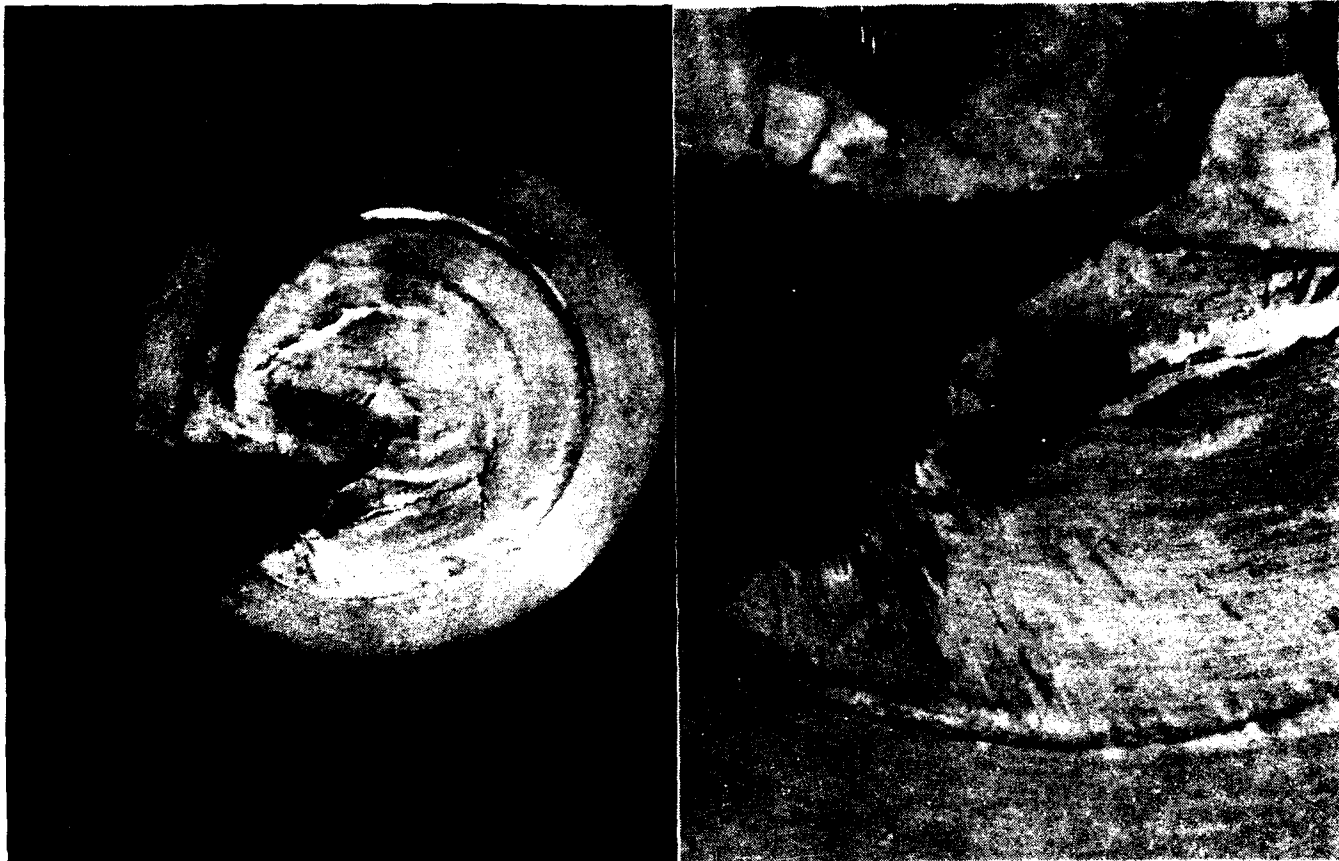


Figure II.5.24. Reactions in 2090-T81 (6 kg·m, open-cup LOX) along shear lip and at crack. Note the even smaller reaction below, and to the left of, the reaction at the crack. (5X)



Figure II.5.25. Two extensive reactions in 2090 (6 kg·m, open-cup LOX) that initiated on shear lip. (5X)



Figure II.5.26. Macroreaction on shear lip of WL049-T851 (10 kg·m, open-cup LOX). (5X)



Figure II.5.27 Macroreaction at split in WL049-T651 (10 kg·m, open-cup LOX). (5X)

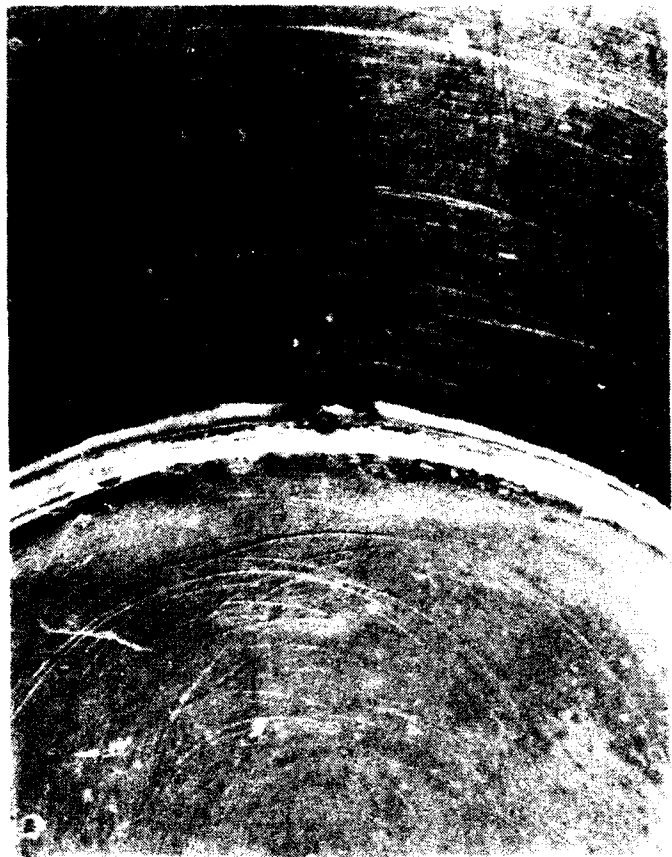


Figure II.5.28. Reaction on shear lip of WL049-T651 (10 kg·m, open-cup LOX). (5X)



Figure II.5.29. Reaction on shear lip of alloy 2219-T851 (10 kg·m, open-cup LOX). (5X)

Table II.5.5. Results of Pressurized Mechanical Impact Tests.

Alloy	Env.	Energy, kg·m (ft·lb)	Pressure, MPa (psi)	Temperature,*			No. of specimens	No. of flashes	No. of burns	Rebound height, cm (in)
				K	high	low				
WL049-T851	GOX	10	(72)	0.35 (50)	---	20	0	0	0	40.6 (16.0)
WL049-T851	GOX	8	(58)	0.69 (100)	---	20	0	0	0	39.3 (15.5)
WL049-T851	GOX	6	(43)	0.10 (14.7)	---	20	0	0	0	40.4 (15.9)
2090-T81	GOX	10	(72)	0.69 (100)	---	20	0	0	0	21.9 (8.6)
2090-T81	GOX	8	(58)	0.10 (14.7)	---	20	0	0	0	27.6 (10.9)
2090-T81	GOX	6	(43)	0.35 (50)	---	20	0	0	0	29.5 (11.6)
2219-T87	GOX	10	(72)	0.10 (14.7)	---	20	0	0	0	32.9 (13.0)
2219-T87	GOX	8	(58)	0.35 (50)	---	20	0	0	0	29.2 (11.5)
2219-T87	GOX	6	(43)	0.69 (100)	---	20	0	0	0	27.4 (10.8)
WL049-T851	LOX	10	(72)	0.35 (50)	105	93	21	0	1	38.1 (15.0)
WL049-T851	LOX	8	(58)	0.69 (100)	105	94	20	0	1	37.6 (14.8)
WL049-T851	LOX	6	(43)	0.10 (14.7)	91	88	20	0	0	33.5 (13.2)
2090-T81	LOX	10	(72)	0.69 (100)	105	98	20	0	0	25.1 (9.9)
2090-T81	LOX	8	(58)	0.10 (14.7)	90	89	20	0	0	23.1 (9.1)
2090-T81	LOX	6	(43)	0.35 (50)	104	94	20	0	1	26.4 (10.4)
2219-T87	LOX	10	(72)	0.10 (14.7)	91	90	20	0	0	23.9 (9.4)
2219-T87	LOX	8	(58)	0.35 (50)	105	98	20	0	0	24.1 (9.5)
2219-T87	LOX	6	(43)	0.69 (100)	111	92	20	0	0	31.8 (12.5)

\*These values are the highest and lowest temperatures recorded among the test temperatures for the series of 20 tests at the specified test condition.

T81 at 6 kg·m and 0.35 MPa (50 psi), and in WL049-T851 at 10 kg·m and 0.35 MPa (50 psi) and at 8 kg·m and 0.69 MPa (100 psi). The operational definition of "reaction" at this macro level is noted above, in Section II.5.2.1. Appendix II.A. discusses the problems in interpreting the Taguchi matrix when the number of macroreactions is so low. One observation is that the reaction threshold needs to be determined before the matrix is finalized. Section II.7.4.2. discusses the results of a closer examination of the specimens under higher powers of magnification. The lesser number of macroreactions, as compared to results of open-cup testing, is analyzed further in Section II.5.3.3.

### II.5.3.2. Physical Measurements on Specimens

The physical measurements on the specimens were made as described above in Section II.5.2.1. Tables II.5.6 and II.5.7 show that the modifications to the pressurized tester increased the energy absorbed by the specimen, as evidenced by the indentation depths of 0.04–0.59 mm (0.0017–0.0232 in) and large numbers of splits. Pressurized tests at WSTF reported in Part I resulted in indentation depths of 0.0229–0.4039 mm (0.0009–0.0159 in) for similar impact energy levels on 1.6-mm (1/16-in) specimens (see Tables I.C.13 and 16). Penetration depth is plotted versus reaction energy in Figure II.5.30. A positive correlation is observed, as expected. Figure II.5.31, in which percentage of splits is plotted versus average penetration depth, shows that there were more splits in specimens in LOX than in GOX, even though the impact depths were approximately the same. For example, WL049-T851 had no splits in GOX at 10 kg·m and 0.035 MPa (50 psi) with an average depth of 0.32 mm (0.0126 in), whereas the same alloy and temper had 5 splits in LOX under the same conditions with an average depth of 0.32 mm (0.0125 in). The 2219-T87 alloy had no splits in GOX at 10 kg·m and ambient pressure and an average depth of 0.34 mm (0.0161 in), but in LOX, under the same conditions, had 8 splits with an average depth of 0.411 mm (0.0175 in). The rebound heights for the alloys that split were usually lower, at the same impact-energy levels, than for alloys that did not split.

The eccentricity of the impact strike is plotted versus the average penetration depth in Figure II.5.32. Again, as noted for the open-cup tests, there is no correlation. However, the eccentricity in LOX was much greater than in GOX. This is because the specimen-cup insert was not used in the LOX tests, leaving the specimen more freedom to move off center. This was done to prevent constraint of the specimen by the insert. Since the pressurized GOX tests were run first, difficulties with the specimens sticking in the inserts led to the change in procedure for the pressurized LOX tests.

### II.5.3.3. Comparison of Macroreactions and Physical Measurements. Pressurized and Open-Cup Tests

Table II.5.8 compares average penetration depths,  $\bar{d}$ , and rebound heights in the pressurized GOX and LOX tests with the corresponding parameters from the present series of open-cup tests for the three alloys (2090-T81, WL049-T851, and 2219-T87) for which comparative data are available. Since the uncertainty in measuring the penetration depths is about  $\pm 0.05$  mm (0.002 in), it is clear that there is no significant difference between  $\bar{d}$  for the GOX or LOX environment in the pressurized tests. However, for the WL049-T851 and perhaps the 2219-T87 alloys, there does appear to be a decrease in  $\bar{d}$  in the pressurized tests as compared with the open-cup tests. Examination of Table II.5.2 shows that the

Table II.5.6. Summary of Physical Measurements: On Specimens in LOX and GOX, Ambient and Pressurized Environment.

Alloy	Env.	Energy, kg-m (ft-lb)	Pressure, MPa (psi)	No. of splits	Avg. impact depth, mm (in)	Avg. depth, w/ splits, mm (in)	Avg. depth, w/ burns, mm (in)	No. of shear lips
W049-T851	GOX	10 (72)	0.35 (50)	0	0.32 (0.0126)	...	...	6
W049-T851	GOX	8 (58)	0.69 (100)	0	0.21 (0.0082)	...	...	4
W049-T851	GOX	6 (43)	0.10 (14.7)	0	0.04 (0.0017)	...	...	0
2090-T81	GOX	10 (72)	0.69 (100)	20	0.59 (0.0232)	0.59 (0.0232)	...	20
2090-T81	GOX	8 (58)	0.10 (14.7)	20	0.32 (0.0126)	0.32 (0.0126)	...	19
2090-T81	GOX	6 (43)	0.35 (50)	11	0.16 (0.0063)	0.21 (0.0083)	...	9
2219-T87	GOX	10 (72)	0.10 (14.7)	0	0.41 (0.0161)	...	...	0
2219-T87	GOX	8 (58)	0.35 (50)	0	0.27 (0.0128)	...	...	0
2219-T87	GOX	6 (43)	0.69 (100)	0	0.16 (0.0077)	...	...	0
W049-T851	LOX	10 (72)	0.35 (50)	5	0.32 (0.0125)	0.46 (0.0182)	0.47 (0.0185)	18
W049-T851	LOX	8 (58)	0.69 (100)	0	0.16 (0.0077)	...	0.18 (0.0070)	14
W049-T851	LOX	6 (43)	0.10 (14.7)	0	0.07 (0.0035)	...	...	2
2090-T81	LOX	10 (72)	0.69 (100)	20	0.53 (0.0207)	0.53 (0.0207)	...	20
2090-T81	LOX	8 (58)	0.10 (14.7)	20	0.38 (0.0151)	0.38 (0.0151)	...	20
2090-T81	LOX	6 (43)	0.35 (50)	11	0.18 (0.0072)	0.27 (0.0106)	0.18 (0.007)	13
2219-T87	LOX	10 (72)	0.10 (14.7)	8	0.44 (0.0175)	0.53 (0.0207)	...	14
2219-T87	LOX	8 (58)	0.35 (50)	1	0.29 (0.0113)	...	...	16
2219-T87	LOX	6 (43)	0.69 (100)	0	0.13 (0.0052)	...	...	1

Table II.5.7. Summary of Physical Measurements: Splits and Eccentricity, on Specimens in GOX, LOX, Ambient and Pressurized Environment.

Alloy	Env.	Energy, kg·m (ft·lb)	Pressure, MPa (psi)	No. of Splits	Splits with flash	Splits with burns	Avg. $\bar{c}$ , $\bar{c}$ , (in)	Avg. $\bar{c}$ , $\bar{c}$ , w/ splits, (in)	Avg. $\bar{c}$ , $\bar{c}$ , w/ flash, (in)	Avg. $\bar{c}$ , $\bar{c}$ , w/ burns, (in)
WL049-T851	GOX	10	(72)	0.35 (50)	0	0	0.71 (0.0285)	...	...	...
WL049-T851	GOX	8	(58)	0.69 (100)	0	0	0.75 (0.0295)	...	...	...
WL049-T851	GOX	6	(43)	0.10 (14.7)	0	0	0.65 (0.0255)	...	...	...
2090-T81	GOX	10	(72)	0.69 (100)	20	0	0.48 (0.0190)	0.91 (0.036)	...	...
2090-T81	GOX	8	(58)	0.10 (14.7)	20	0	0.65 (0.0255)	1.19 (0.047)	...	...
2090-T81	GOX	6	(43)	0.35 (50)	11	0	0.58 (0.0230)	1.14 (0.045)	...	...
2219-T87	GOX	10	(72)	0.10 (14.7)	0	0	0.60 (0.0235)	...	...	...
2219-T87	GOX	8	(58)	0.35 (50)	0	0	0.58 (0.0230)	...	...	...
2219-T87	GOX	6	(43)	0.69 (100)	0	0	0.71 (0.0280)	...	...	...
WL049-T851	LOX	10	(72)	0.35 (50)	5	0	2.1.45 (0.057)	2.09 (0.082)	...	2.07 (0.081)
WL049-T851	LOX	8	(58)	0.69 (100)	0	0	0.1.32 (0.052)	...	...	1.40 (0.055)
WL049-T851	LOX	6	(43)	0.10 (14.7)	0	0	0.1.35 (0.053)	...	...	...
2090-T81	LOX	10	(72)	0.69 (100)	20	0	0.1.63 (0.064)	1.63 (0.064)	...	...
2090-T81	LOX	8	(58)	0.10 (14.7)	20	0	0.1.29 (0.050)	1.29 (0.050)	...	...
2090-T81	LOX	6	(43)	0.35 (50)	11	0	1.1.60 (0.063)	1.50 (0.059)	...	2.46 (0.097)
2219-T87	LOX	10	(72)	0.10 (14.7)	8	0	0.1.19 (0.047)	1.88 (0.074)	...	...
2219-T87	LOX	8	(58)	0.35 (50)	0	0	0.1.58 (0.062)	...	...	...
2219-T87	LOX	6	(43)	0.69 (100)	0	0	0.1.40 (0.055)	...	...	...

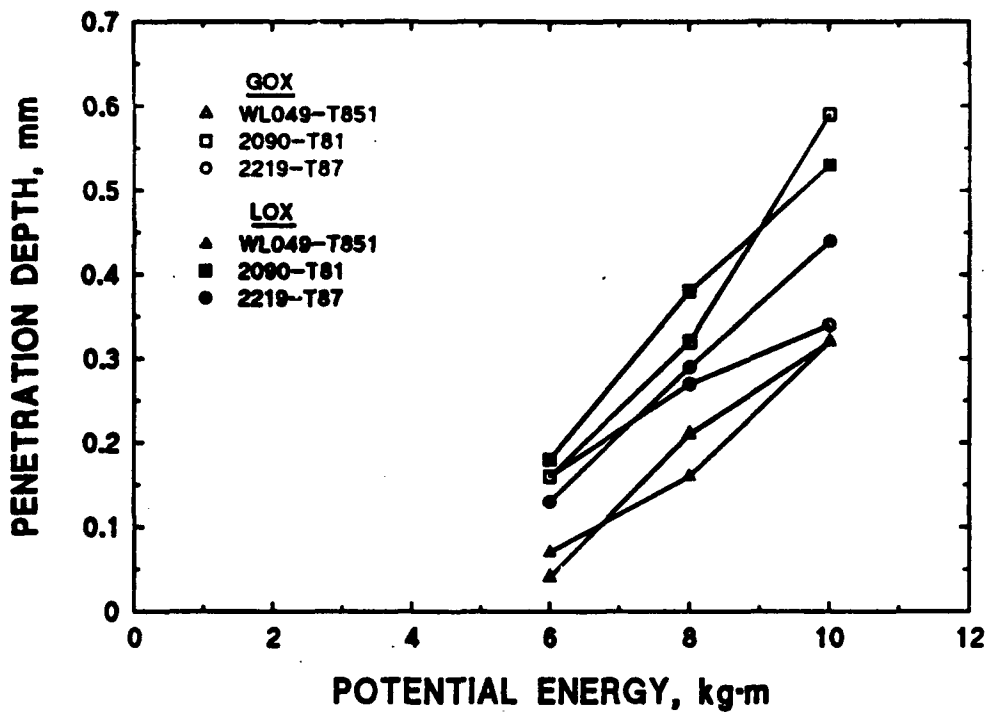


Figure II.5.30. Average penetration depth vs. potential (impact) energy for pressurized tests in LOX and GOX.

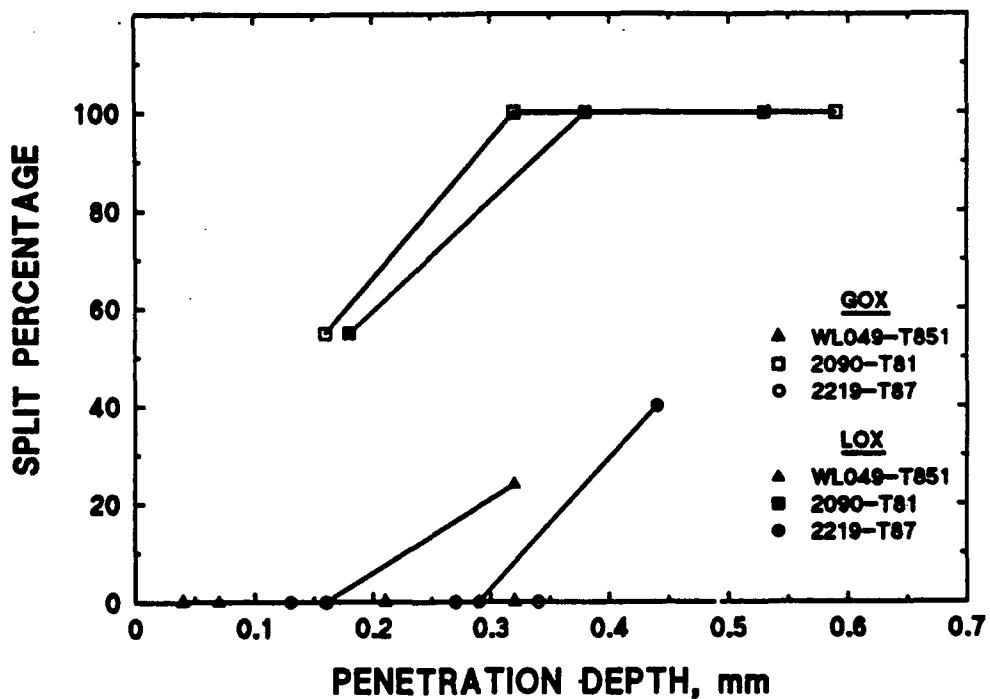


Figure II.5.31. Percentage of splits vs. average penetration depth for pressurized tests in LOX and GOX.

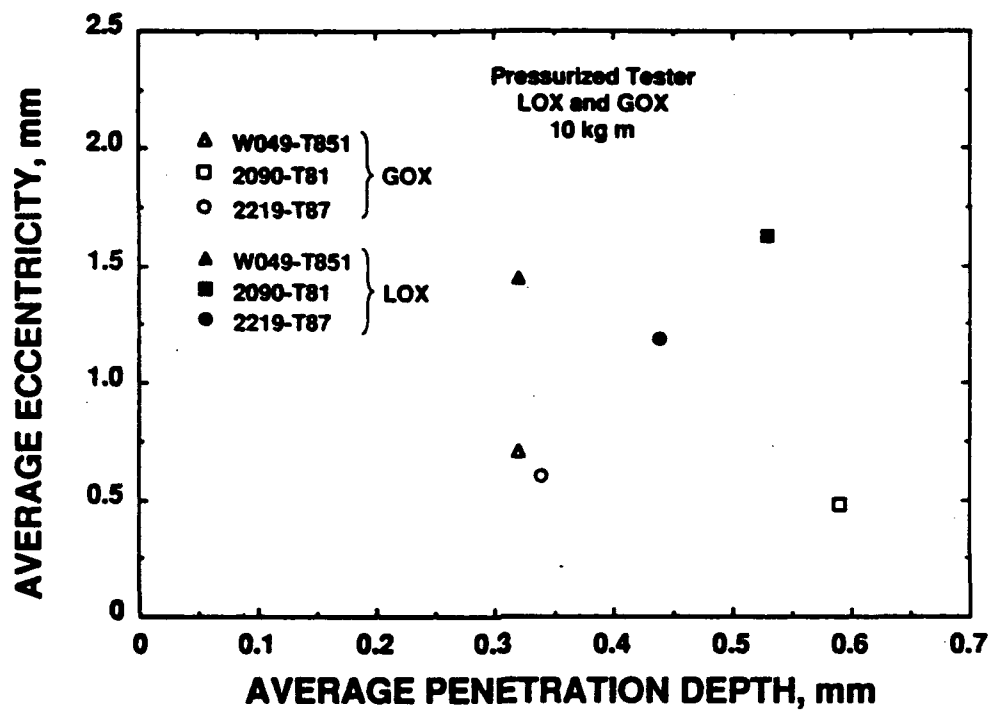


Figure II.5.32. Average eccentricity vs. average penetration depth for pressurized tests in LOX and GOX with a potential (impact) energy of 10 kg·m.

Table II.5.8. Penetration Depths and Rebound Heights, Open-Cup and Pressurized Tests.

Alloy	Energy, kg·m (ft·lb)	Penetration Depths,			Rebound Heights,		
		Open Cup mm (in)	GOX mm (in)	LOX mm (in)	Open Cup mm (in)	GOX mm (in)	LOX mm (in)
2090-T81	10 (72)	0.574 (0.0226)	0.589 (0.0232)	0.526 (0.0207)	203 (8.0)	218 (8.6)	251 (9.9)
	8 (58)	0.429 (0.0169)	0.320 (0.0126)	0.384 (0.0151)	180 (7.1)	277 (10.9)	231 (9.1)
	6 (43)	0.290 (0.0114)	0.160 (0.0063)	0.183 (0.0072)	160 (6.3)	295 (11.6)	264 (10.4)
	4 (29)	0.107 (0.0042)	—	—	178 (7.0)	—	—
	2 (15)	0.013 (0.0005)	—	—	119 (4.7)	—	—
	—	—	—	—	—	—	—
WL049-T851	10 (72)	0.452 (0.0178)	0.320 (0.0126)	0.318 (0.0125)	267 (10.5)	406 (16.0)	381 (15.0)
	8 (58)	0.282 (0.0111)	0.208 (0.0082)	0.196 (0.0077)	279 (11.0)	394 (15.5)	376 (14.8)
	6 (43)	0.168 (0.0066)	0.043 (0.0017)	0.089 (0.0035)	269 (10.6)	404 (15.9)	335 (13.2)
	4 (29)	0.084 (0.0033)	—	—	201 (7.9)	—	—
	—	—	—	—	—	—	—
	—	—	—	—	—	—	—
2219-T87	10 (72)	0.498 (0.0196)	0.409 (0.0161)	0.445 (0.0175)	231 (9.1)	330 (13.0)	239 (9.4)
	8 (58)	0.282 (0.0111)	0.325 (0.0128)	0.287 (0.0113)	257 (10.1)	292 (11.5)	241 (9.5)
	6 (43)	0.218 (0.0086)	0.196 (0.0077)	0.132 (0.0052)	231 (9.1)	274 (10.8)	318 (12.5)
	—	—	—	—	—	—	—

macroreaction frequency for the Al-Li alloys decreases sharply between 10 and 8 kg·m. Thus, tests at 10-kg·m impact (potential) energy are at, or just above, the reaction threshold, so a small decrease in the absorbed energy of the specimen in the pressurized system could drastically reduce the observed macroreaction frequency.

A further possible cause for the lowered reaction frequency in pressurized testing is the change in methodology for observing flashes. These were visually observed by a technician in the open-cup testing and recorded by a photocell in the pressurized tests. It is thought that the photocell might have been located so close to the striker pin that the field of vision was limited. Note that the number of flashes in Table II.5.2 exceeded the number of burns (charring evident to the naked eye).

The difference between the impact, or potential energy,  $E_p$ , and the recoil energy,  $E_r$ , is plotted versus the average penetration depth,  $\bar{d}$ , for the three alloys for which comparative open-cup and pressurized data are available in Figure II.5.33. Equation (8-1) from Section I.8.1. indicates that the quantity on the y-axis,  $E_p - E_r$ , should be equal to  $E_f + E_a$ , where  $E_f$  denotes the frictional energy losses absorbed in the machine, and  $E_a$  is the energy absorbed by the specimen. Equation (7-6) from Section I.7.1.6. shows that  $E_a$  should be linearly proportional to the impact depth of the specimen. The offset of about 15 J on the y-axis ( $\bar{d} = 0$ ) corresponds to  $E_f$ .  $E_p - E_r$  is a linear function of  $\bar{d}$ , as expected. The slight offset in the linear relationship for WL049-T851 as compared with 2090-T81 is due to the increased splitting in the latter alloy, which allows a greater penetration depth. The difference in splitting behavior in the two alloys is explained in Section II.5.1.4. The increase in  $E_a$  or  $\bar{d}$  with increasing impact energy ( $E_p$ ) can be understood by reference to Section I.8.5. and Figure I.8.1(a) which give idealized stress-strain diagrams. Increasing  $E_p$  allows the stress,  $\sigma$ , on the specimen to increase; thus,  $\bar{d} = \bar{d}/h$  ( $h$  = specimen thickness) is increased, as is  $E_a$ , the area under the stress-strain curve.

#### II.5.4. Comparison of Mechanical-Impact Equipment and Procedures at WSTF, MSFC, and SSFL

Comparisons of the three pressurized mechanical-impact testers at WSTF, MSFC and SSFL were previously made by Bransford et al.<sup>5</sup> and Bryan<sup>6</sup> and in Section I.5.5. of Part I. The present summary is based on further data from Part II of the mechanical-impact testing at WSTF. As mentioned in Part I of this report, specimens tested in the WSTF machines did not absorb as much energy as did specimens in the SSFL and MSFC machines. The WSTF ABMA test machine was modified for this program by changing from an Al-alloy cup and stainless-steel insert to the use of a Ni-based alloy cup only. The WSTF pressurized machine was also modified so that it would deliver more absorbed energy into the specimens.

As explained above in Section II.4.4., disks of annealed 304 stainless steel were found to be inadequate to calibrate impact depths and absorbed energies of the specimens for the particular combinations of test alloys and specimen-cup materials in this program. For this reason, a series of 2090-T81 comparison specimens from the 12.4-mm (1/2-in) plate in the 3-mm (1/8-in) thickness were impacted to evaluate and compare the

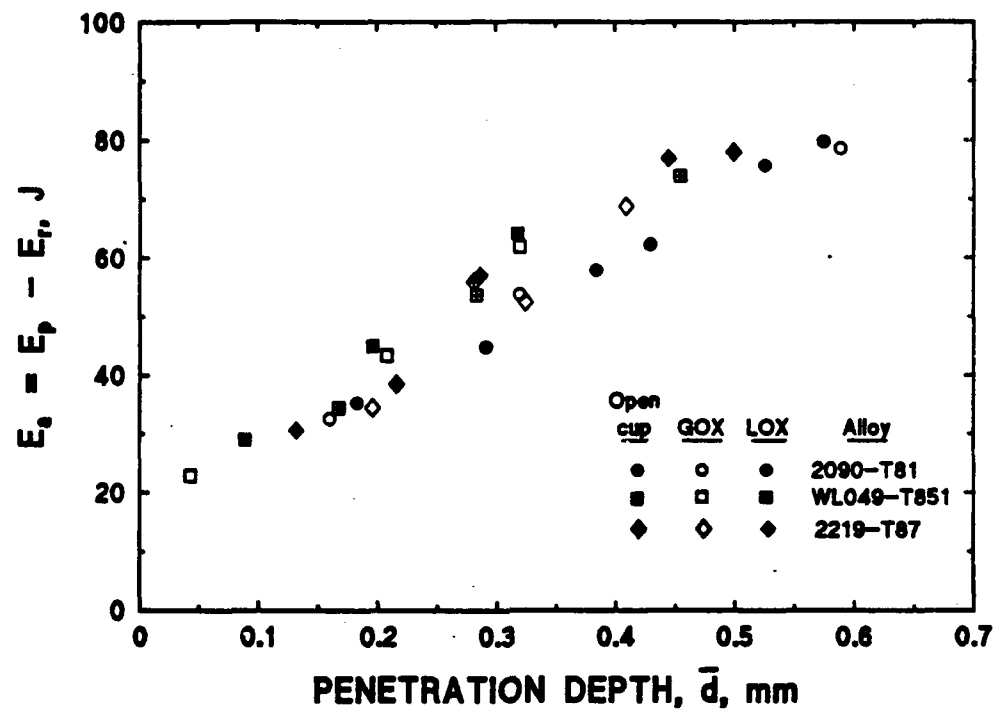


Figure II.5.33. Absorbed energy vs. penetration depth for open-cup and pressurized tests in LOX and GOX.

energy absorbed by the specimens in the modified machines. Table II.5.9 shows that the impact depths from the modified open-cup machine were deeper than those from the MSFC and SSFL pressurized machines. Table II.5.9 also shows that the average penetration depth from the 2090-T81 specimens tested in the WSTF pressurized machine are now also larger than the average depths from comparable specimens impacted at MSFC or SSFL. Thus, the modifications outlined in Sections II.4.2.1. and II.4.3.1. of this report, enabled the pressurized impact machine to deliver an adequate amount of energy to the specimens. The test procedure was also changed so that among every group of 20 specimens, a single 2090-T81 comparison specimen was impacted in order to ensure that the system was operating consistently. These single comparison specimens had impact depths ranging from 0.43 mm (0.017 in) to 0.58 mm (0.023 in), within expected scatter for the penetration-depth measurement.

In Part II of this program, all load-train components in the open-cup and pressurized machines were examined for adherence to the NASA NHB 8060.1B<sup>1</sup> specifications. In particular, the pin surfaces and radii were checked for conformance to the specification described earlier in Section I.5.3.3. All parts were found to be within specification. As mentioned before, the specified Al-alloy cup and insert were eliminated and replaced with a Ni-based alloy cup in the open-cup machine. Although this was a deviation from the specification, it was a necessary change to increase the level of absorbed energy in the Al-Li and 2219 specimens.

The specimen-changing procedure for the WSTF pressurized tests differs from the MSFC and SSFL procedure in that the specimen is installed by lifting the pressurized machine and placing the pre-cooled specimen and cup on the anvil. The specimen and cup are cooled by pouring LOX through the top of the chamber. This procedure is outlined in Section II.4.3.1., above.

In conclusion, both of the modified WSTF impact test machines, open-cup and pressurized, deliver at least as much energy into the specimen as do other test facilities.

## II.5.5. Promoted-Combustion Tests

Most results of the promoted-combustion tests, conducted at WSTF, are contained in the interim report (Section I.5.6. and Appendix I.B.). Additional tests were conducted on 8090-T8771, WL049-T851, 2219-T851, and 2219-T87 (Table II.5.10). Graphs and all data are contained in Figures II.5.34(a-g). These are summarized in Figure II.5.35. From these figures, it is clear that the threshold oxygen pressure to cause complete burns in all Al-Li alloys [2.1 MPa, (300 psi)] is an order of magnitude higher than the threshold energy for complete burns in all 2219 tempers [0.21 MPa (30 psi)]. The data are very consistent and conclusive. The Al-Li alloys are less flammable than alloy 2219 in the presence of oxygen under pressure.

Table II.5.9. Comparison of Specimen Impact Depths  
2090-T81 (12.5-mm plate, 3-mm thick comparison samples).

Machine	Energy, kg·m (ft·lb)	Environment	Impact Depth, mm (in)	Average Depth, mm (in)
WSTF Open cup	10 (72)	LOX, Ambient	0.584 (0.0230) 0.536 (0.0211) 0.511 (0.0201) 0.427 (0.0168) 0.589 (0.0232)	0.528 (0.0208)
WSTF Open cup	11 (79)	LOX, Ambient	0.554 (0.0218) 0.602 (0.0237) 0.632 (0.0249) 0.749 (0.0295) 0.676 (0.0266)	0.643 (0.0253)
MSFL pressurized	10 (72)	LOX, 0.69 MPa, (500 psi)	—	0.368 (0.0145)
SSFL pressurized	10 (72)	LOX, 0.55 MPa, (400 psi)	—	0.345 (0.0136)
WSTF pressurized	10 (72)	LOX, Ambient	0.46 (0.018) 0.48 (0.019) 0.51 (0.020) 0.51 (0.020) 0.43 (0.017)	0.478 (0.0188)

Table II.5.10. Results of Promoted-Combustion Tests from WSTF  
on Specimens 14.7 cm Long.

Alloy	Test Pressure, psia												
	15	20	25	30	40	50	60	65	70	80	200	250	300
Length of Specimen Consumed, cm													
8090-T8771											3.4		
											3.5		
											3.4		
8090-T8151											3.1	4.2	
											2.6	4.2	
											2.8	5.4	
8090-T3**		2.1	1.7	2.0	1.6	3.8					3.5		
						1.6					3.3		
											3.6		
2090-T81 (12.7-mm plate)			0.2			3.4					2.8	4.2	
											3.1	6.7	
											3.5		3.5
WL049-T851 (Lot 1)											3.8	5.0	CB
												9.8	
												5.6	
WL049-T651											3.7		
											3.2		
											3.1		
WL049-T351			2.2								3.1		
											1.5		
											3.3		
2219-T87 (Lot No. 294592)	3.4	CB	10.0										
	0.3		8.2										
	12.3		CB										
			CB										
			CB										
2219-T851	0.6	3.5	CB					CB					
		4.7	CB										
		1.6	11.8										
2219-T37		0.2	8.0	6.4	13.6	9.7	CB	CB	CB	CB			
		6.4	CB										
		CB											
		CB											

\*CB - Complete Burn

\*\*Initial Specimen Length - 12.2cm

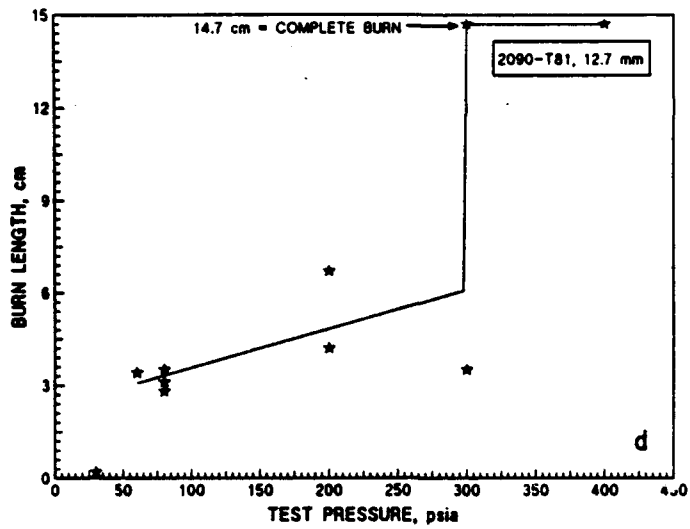
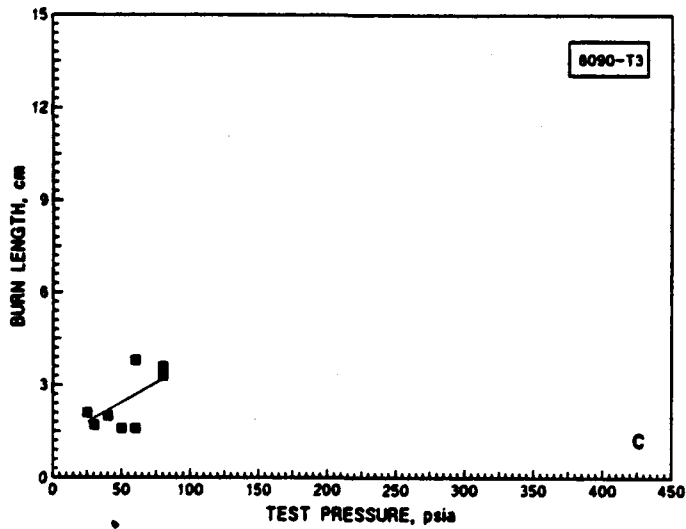
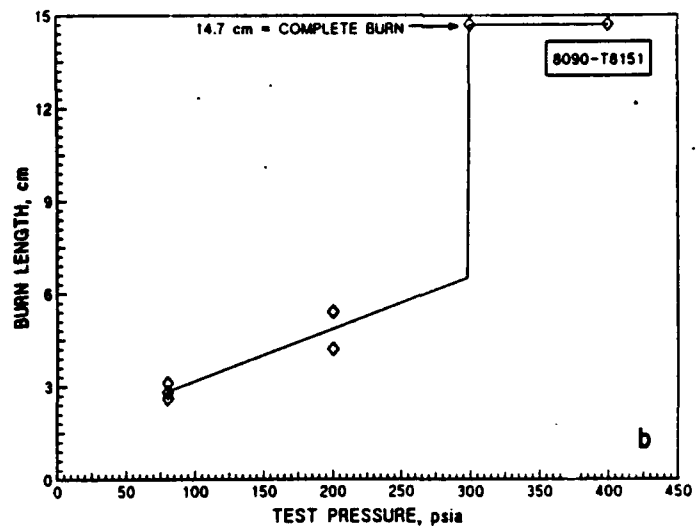
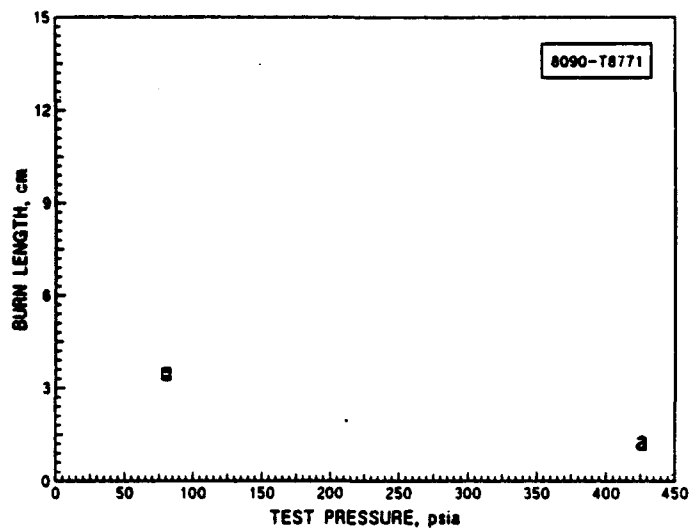


Figure II.5.34. Burn length vs. test pressure for (a) 8090-T8771, (b) 8090-T8151, (c) 8090-T3, (d) 2090-T81, 12.7-mm thick plate, (e) WL049-T851, (f) WL049-T651, (g) WL049-T351, (h) 2219-T87, (i) 2219-T851, and (j) 2219-T37. (See next two pages for continuation of figure.)

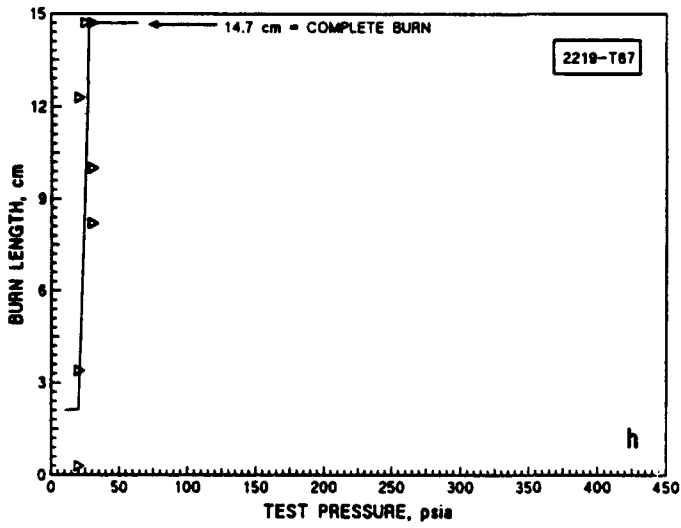
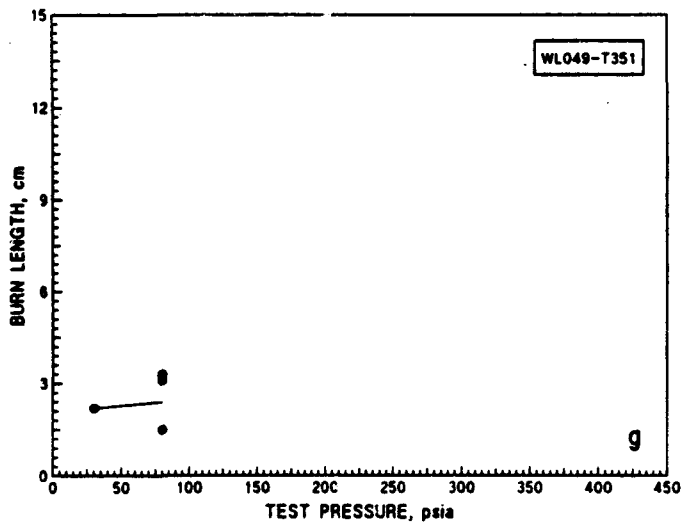
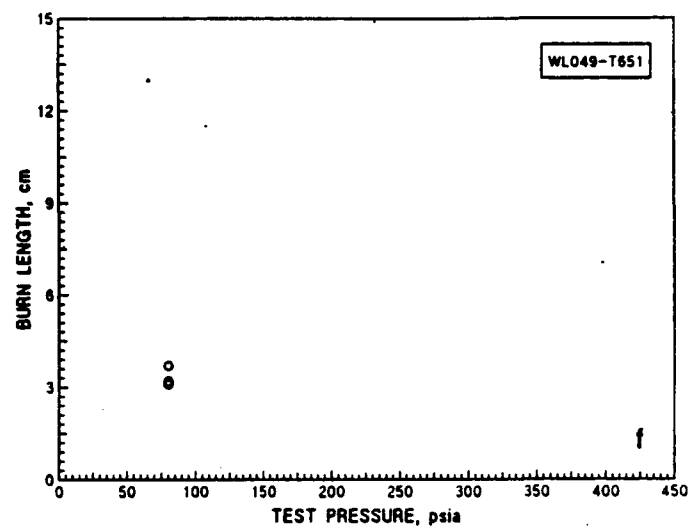
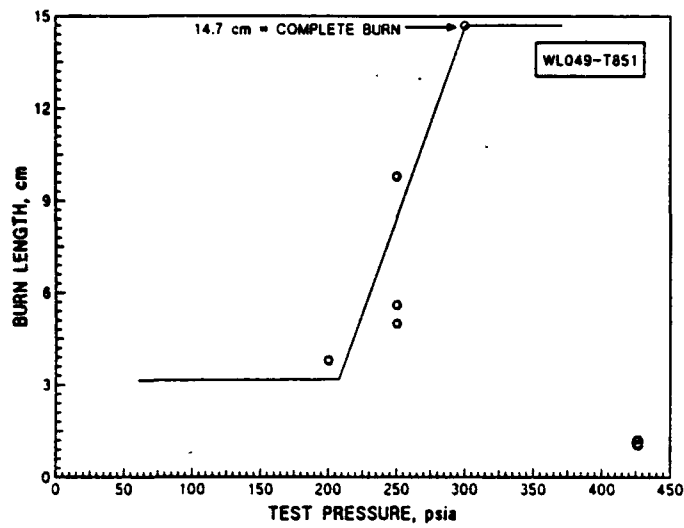


Figure II.5.34., continued

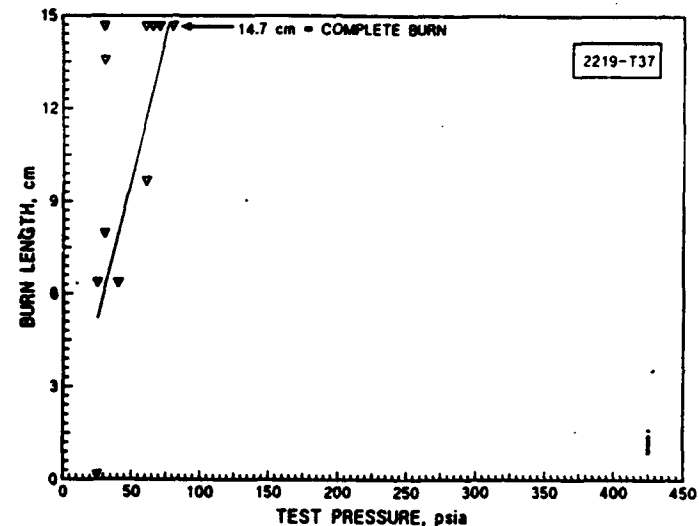
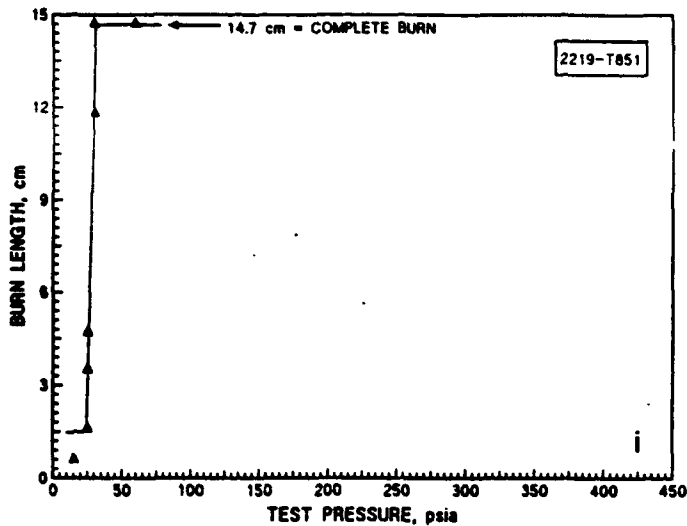


Figure II.5.34. continued

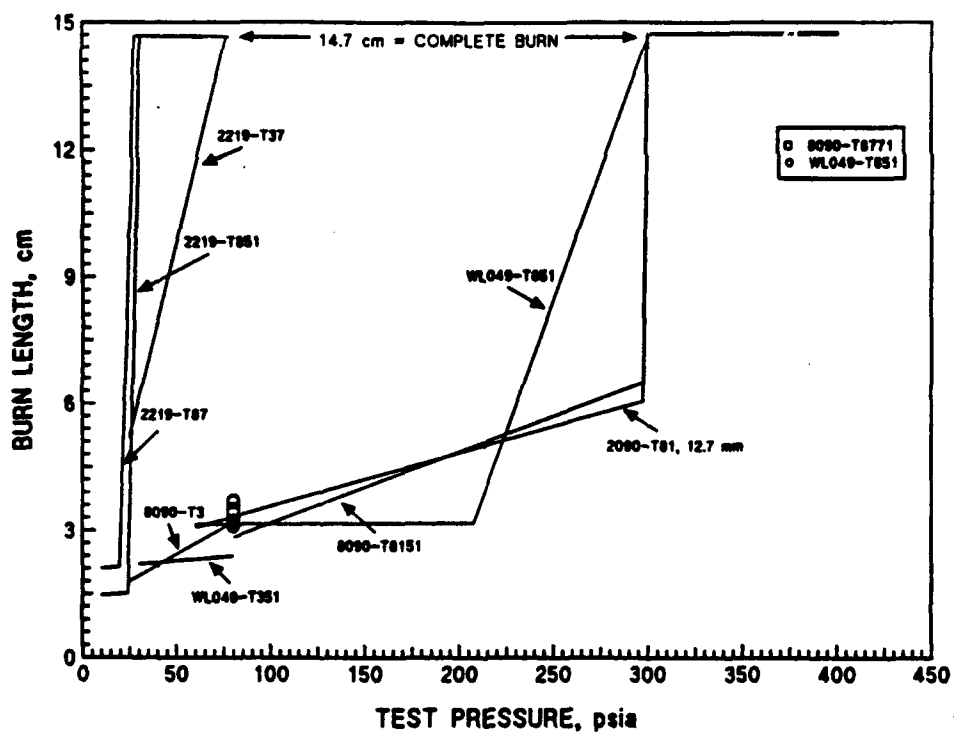


Figure II.5.35. Summary of burn length vs. test pressure of fitted curves for the following alloys: 8090 (tempers T8771, T8151, and T3); 2090-T81; WL049 (tempers T851, T651, and T351); and 2219 (tempers T87, T851, and T37).

## II.6. IGNITION TEMPERATURES AND CONDITIONS

### II.6.1. Experimental Studies of Ignition Temperature of Al in O<sub>2</sub>

The ignition temperature of Al in O<sub>2</sub> varies significantly in different experiments because the condition of the protective oxide layer is the determining factor. A survey of the literature in Part I of this report (Section I.6.2.) reported ignition temperatures that varied from 923 to 2318 K. In fact, a single ignition temperature may be well defined only for metals, such as Mg, that don't form a protective oxide layer.<sup>7</sup> Metals with a protective oxide layer, in general, should not ignite until they melt; the mobility in the liquid state can cause rupture at the film.<sup>8</sup> A fresh Al surface very quickly forms an oxide layer of about 20 nm (200 Å); then, further oxidation is very slow.<sup>9</sup> Often, ignition temperature experiments on metals are done with small spheres<sup>10,11,12</sup> usually placed in a furnace but sometimes in a flame of known temperature. The Al<sub>2</sub>O<sub>3</sub> not only has a high melting point (2318 K), but also, it is less dense than the metal, so it does not sink into the molten metal. Thus, the small Al spheres retain enough integrity to preserve the outer oxide layer even above the melting temperature of Al, and ignition of even small spheres (35–45-μm diameter) may not be observed until the temperature is within 100–400 K of the oxide melting temperatures.<sup>13,10,14</sup> If the oxide skin is broken, "catastrophic," i.e., excessive, oxidation rather than ignition may result under certain conditions.<sup>15</sup> In laser ignition of 230–680-μm spheres in air or O<sub>2</sub>, the initial flame tongue appeared at only one point of the particle surface; this was interpreted as indicating that ignition was preceded by a disruption of the oxide film.<sup>16</sup>

Although the protective surface-oxide layer is very influential in preventing ignition, the actual ignition event may not be a surface-oxidation reaction, but rather a vapor-gas reaction.<sup>17</sup> This conclusion was reached in experiments in which 3–4-mm spheres were heated in Ar and ignition did not occur, even without oxide, until the temperature was greater than 2038 K. Even in experiments on atomized Al (~ 10–100-μm diameter) in which ignition temperatures as low as 923 K (cloud) or 1033 K (layer) were reported, it was stated that the atomized Al usually did not ignite after heating in the furnace, but only if a high voltage spark also was present.<sup>18</sup> This difference was ascribed to the disruption of the oxidized surface by the spark, because ignition was readily obtained in the furnace with flaked Al with a protective stearic-acid coating that prevented formation of the oxide layer. Flash ignition in foils also occurred well below the melting point of the oxide.<sup>14</sup>

In the experiments described above, the closest analogue to the conditions under which ignition may occur in impact testing appears to be the cases described in References 18 and 14, in which a spark suddenly disrupted the protective oxide coating in the presence of O<sub>2</sub> while the thermal conditions necessary for ignitions existed, i.e., T > 932 K. Thus, it is hypothesized that a microreaction could occur if a part of the specimen attains temperatures near the melting point of an Al or Al-Li alloy.

### II.6.2. Experimental Studies of Ignition Temperature of Al in N<sub>2</sub>

Under experimental conditions where particles in O<sub>2</sub> ignited only after melting of Al<sub>2</sub>O<sub>3</sub>, lower ignition temperatures were obtained in gaseous N<sub>2</sub> (~ 1520-1620 K) than in gaseous O<sub>2</sub>. This is thought to occur because the aluminum nitride does not form a barrier to diffusion. Evidence of N as a reactant has been reported by several authors.<sup>19,20,21</sup> This means that "control" experiments in LN<sub>2</sub> to determine whether microreactions are some sort of artifact or are truly reactions of the test alloy with O<sub>2</sub>, could be misleading because surface reactions with N<sub>2</sub> could also occur.

## II.7. DISCUSSION

### II.7.1. Absorbed Energy

In our interim report (Part I) we argued that the absorbed energy of the specimen is the dominant factor affecting reactions in the mechanical-impact test for oxygen compatibility. We suggested that WSTF modify their open-cup and pressurized test equipment to impart more energy to the specimen and to prevent the loss of energy from high striker-pin rebounds. This could be accomplished by reducing the resiliency of the restraining system (see Section I.7.2.3.). Both sets of test equipment were modified and the absorbed energy of the specimens greatly increased. This led to reactions in both systems, similar to those found in MSFC tests in Part I of the program.

We defined two ways to calculate the absorbed energy ( $E_a$ ).

(1) From knowledge of the penetration depth of the striker-pin indentation:

$$E_a = \sigma_c \epsilon_d V_c + \sigma_h \epsilon_t V_t \quad (7-1)$$

where  $\sigma_c$  is the average compressive flow stress,  $\epsilon_d$  is the compressive specimen strain,  $V_c$  is the compressed volume,  $\sigma_h$  is the average tensile hoop stress,  $\epsilon_t$  is the tangential specimen strain, and  $V_t$  is the volume of the specimen under tensile stress. For 2090-T81 we estimate, using equation (7-6) in Section I.7.1.6., that  $E_a = 53$  J for  $E_p = 10$  kg·m.

(2) The absorbed energy may also be estimated using the relationship

$$E_a = E_p - E_r - E_f \quad (7-2)$$

where  $E_p$  is the potential energy of the plummet-striker-pin assembly,  $E_r$  is the energy lost from rebound of the striker pin following specimen impact, and  $E_f$  is the energy lost from friction during the fall of the striker pin to impact. This approach is discussed in Sections I.8.1. and I.8.2. in the interim report. We estimated that  $E_a = 65$  J for conditions during mechanical impact at 10 kg·m for alloy 2090 at MSFC facilities.

In the recent test program at WSTF we obtained more extensive information on penetration depths and rebound heights as a function of  $E_p$  (drop height) to permit firmer estimates of  $E_a$ . In Figure II.7.1,  $E_a$  calculated from specimen deformation characteristics [using Equation (7-1)] is plotted versus  $E_a$  calculated from rebound heights [using Equation (7-2)]. Clearly, there is good linear correlation between the two methods of calculation. For the calculations of  $E_a$  from penetration depths, we assumed that  $\sigma_c = \sigma_h$  and that  $\epsilon_t$ ,  $V_c$ , and  $V_t$  are linear functions of  $\epsilon_d$ . Thus,

$$E_a' = \frac{\epsilon_d'}{\epsilon_d} E_a \quad (7-3)$$

where the primes refer to the new WSTF data,  $E_a = 53$  J, and  $\epsilon_d = \bar{d}/h$  where  $\bar{d} = 0.033$  mm (0.013 in) and  $h = 1.59$  mm (0.0625 in).

All open-cup and pressurized LOX and GOX data are plotted in Figure II.7.1. With some scatter, all fall on the same straight lines, independent of test machine, test temperature, or alloy temper. The data are separated into two alloy groups: 2090 and 8090 in one, and WL049 and 2219 in the other. The higher values of  $E_a$  for alloys 2090 and 8090 from penetration-depth measurements [using Equation (7-1)] result from more extensive specimen splitting. If the specimen splits, the measured penetration depths are larger. Additional discussion is included in Section II.7.3.

The slight offsets at  $E_a$  (penetration depths) = 0 on the  $E_a$  (rebound height) axis suggest that there are undetermined system energy losses of about 10 J. Contributions to these losses could come from friction, and vibration of the support and plummet system. The equivalence of these trends for both open-cup and pressurized test assemblies suggests that vibrational losses are the major contributors.

### II.7.2. Splits

The absorbed energy of the specimens from the impact of the striker pin is usually sufficient to induce cracks in Al alloys. In many cases a large crack develops on the specimen perimeter and grows inward; this is called a split. The fracture surfaces of splits are similar to the fracture surfaces of tensile specimens (interim report, Section I.5.1.). From analysis of the stress distributions presented in Section II.5.1., one would expect that the energy to induce splits on mechanical impact would be a function of the product of the tensile strength and the tensile elongation to failure.

In Figure II.7.2, we plot the tensile fracture energy versus the minimum absorbed energy to induce splits in open-cup tests for the alloys 8090-T8771, 2090-T81, WL049, tempers T851 and T651, and 2219, tempers T87, T851, and T37. The minimum absorbed energy was estimated from striker-pin penetration depths at the lowest impact energy for which splits were observed. The transverse- (T) orientation tensile strength and elongation data at 76 K were used to obtain an estimate of fracture energy. The T orientation was used because the splits have been shown to propagate in the L direction. There is reasonable correlation between these variables as illustrated in Figure II.7.2. This suggests that very high tensile hoop forces cause splitting of the specimens on impact.

### II.7.3. Rebound Heights

The average rebound heights from open-cup tests on three alloys (2090-T81, WL049-T851, and 2219-T87) are plotted versus potential energy (drop height) in Figure II.7.3(a) for unsplit specimens and in Figure II.7.3(b) for split specimens. The rebound heights increased as the potential energy was increased in both cases. However, values for the split specimens are lower by about 100 mm (4 in) at each energy level. The reduced rebound heights for the impacts that resulted in split specimens indicate that splitting is associated with energy absorption. The approximate value of the absorbed energy consumed in splitting is estimated to be 9 J, using  $\Delta E = mg\Delta h$  where  $\Delta h = 100$  mm (4 in). The difference between the absorbed-energy curves (Figure II.7.1) of the alloys that split extensively (2090-T81 and 78

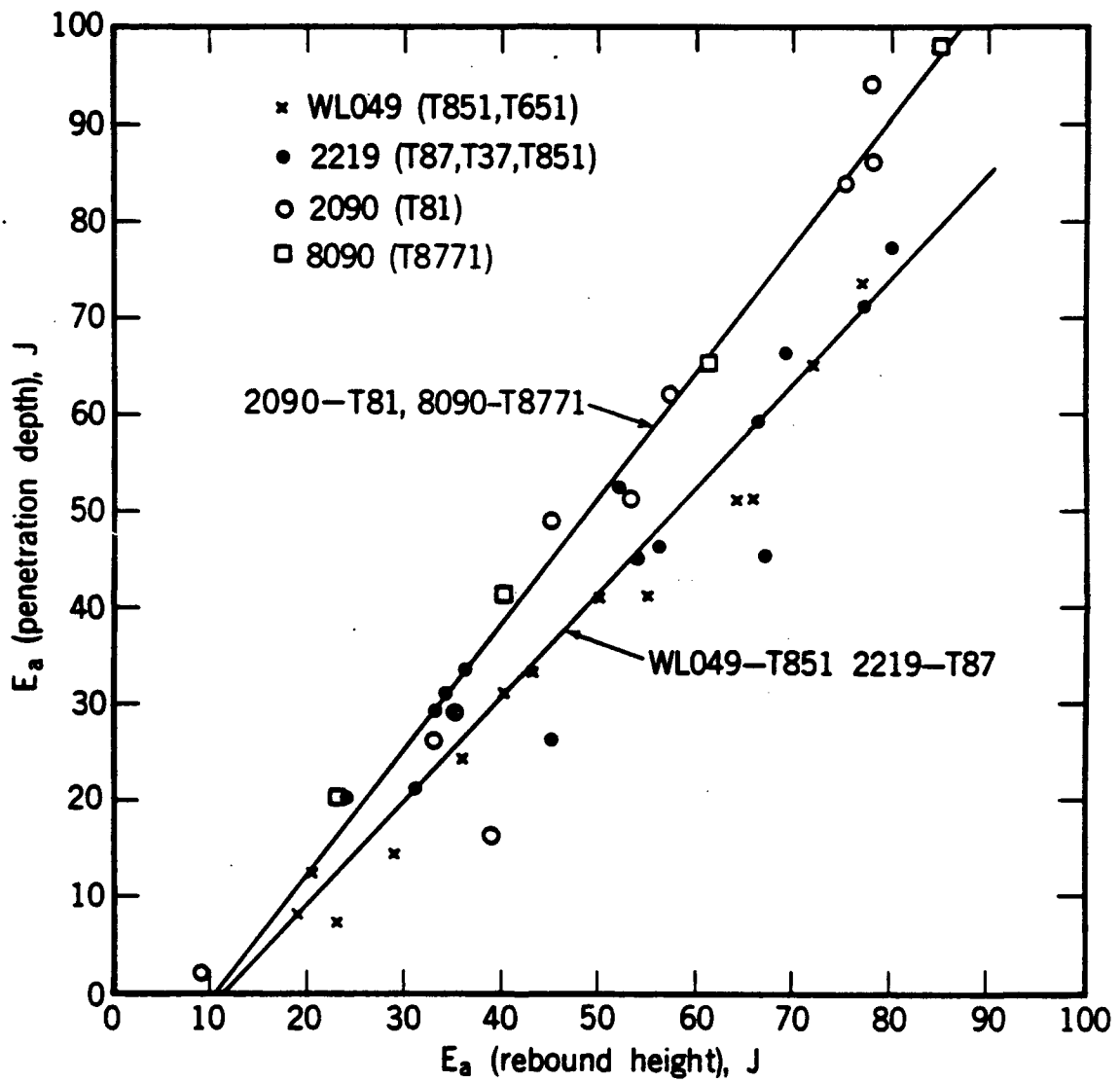


Figure II.7.1. Absorbed energy, calculated from specimen deformation characteristics, vs. absorbed energy, calculated from rebound heights.

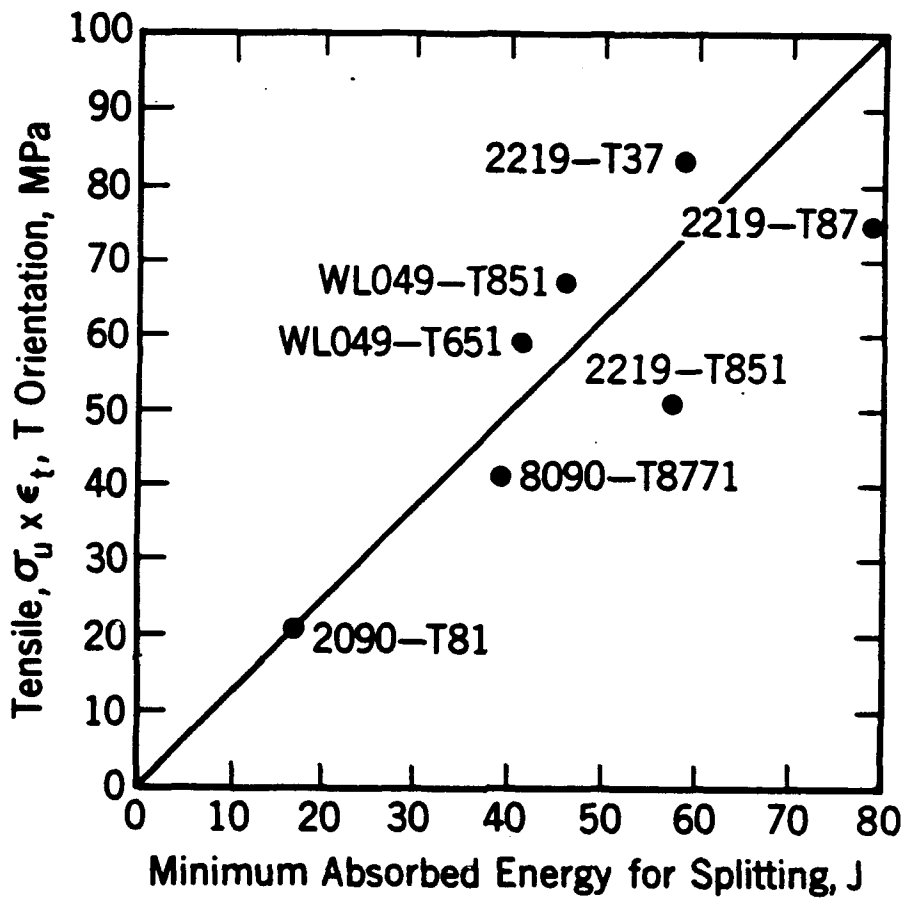


Figure II.7.2. Tensile fracture energy vs. minimum absorbed energy needed to induce splits in open-cup tests.

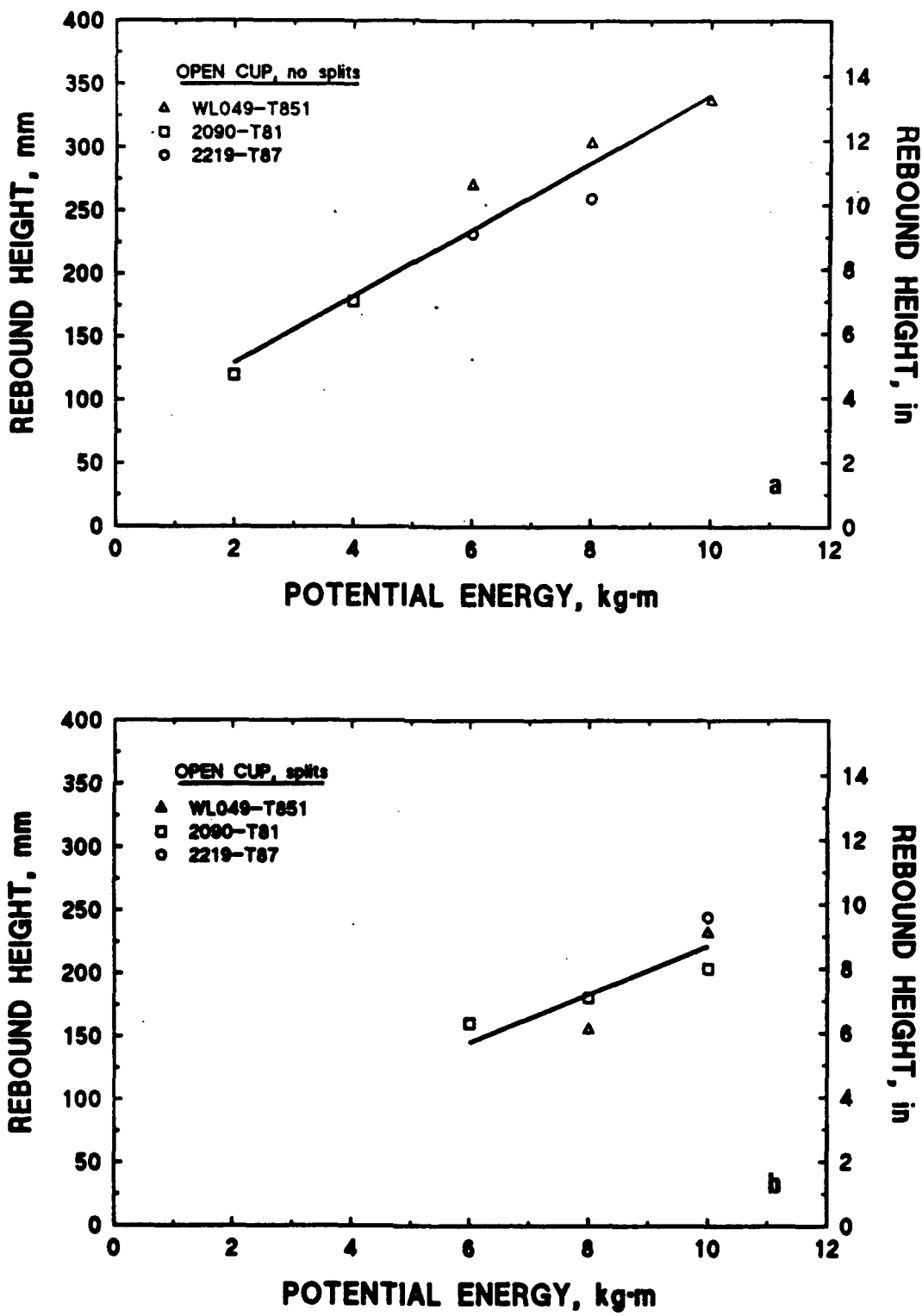


Figure II.7.3. Average rebound height vs. potential energy from open-cup tests where (a) splits did not occur, and (b) where the specimen split.

8090-T8771) and the alloys that split less (WL049-T851 and 2219-T87) is also about 9 J.

The increase of the rebound height with potential energy is expected, despite the inelastic nature of the striker-pin-specimen collision. The increase suggests that at each potential-energy level, a higher stress is obtained in the specimen. This higher stress ensures higher stored elastic energy and, thus, a higher rebound. Possibly, small distinctions between the various alloys in the unsplit specimen data may be attributed to flow strength variations between alloys.

#### II.7.4. Reactions

For this report, a reaction is defined as localized oxidation or burning, leaving remnant oxidation products (that result in localized discoloration) and material transfer (ranging from absence, such as a hole, to flow and spraying). The term, reaction, is identified by test laboratory personnel (using their judgment and experience) following test-standard (NASA NHB 8060.1B<sup>1</sup>) specifications as related to burned or charred areas, flashing, audibility, and discoloration. We point out that in standard NASA NHB 8060.1B there is no explicit definition of a reaction.

Reactions in Al alloys in mechanical-impact tests require three conditions: (1) extensive local deformation, (2) the presence of oxygen, and (3) an oxide-free surface. Under mechanical-impact conditions in which a potential energy of 98 J (10 kg·m) is used, local deformation may be excessive and the associated very high temperature increases may lead to localized melting. Oxygen is present abundantly except under the striker pin on both sides of the specimen. An oxide-free surface is provided by cracking, splitting, or the scraping of the striker pin as it penetrates the specimen during impact.

##### II.7.4.1. Microreactions

In 8090-T8771, microreactions were observed in the SEM on the shear lip. Two of these for 10 kg·m, pressurized LOX tests are shown in Figure II.7.4. Quite possibly, the combination of heavy axial compression and radial shear deformation with frictional heating and ridge formation satisfied, locally, the conditions to achieve local melting and oxidation.

In 2090-T81, microreactions were detected on both sides of the specimens. On the underside, microreactions were always observed in the area between the striker-pin indentation and the outside specimen perimeter. Typical microreactions are shown in Figure II.7.5. Some appear to be associated with grain-boundary precipitates, second phase particles and, perhaps, with clusters of second phase particles. Examples of shear-lip microreactions are shown in Figure II.7.6. Notice that these are more symmetric. In Figure II.7.6(b), there is clear evidence of oxide solidification cracking. In Figure II.7.6(c), there is evidence for local melting, combined with local oxidation.

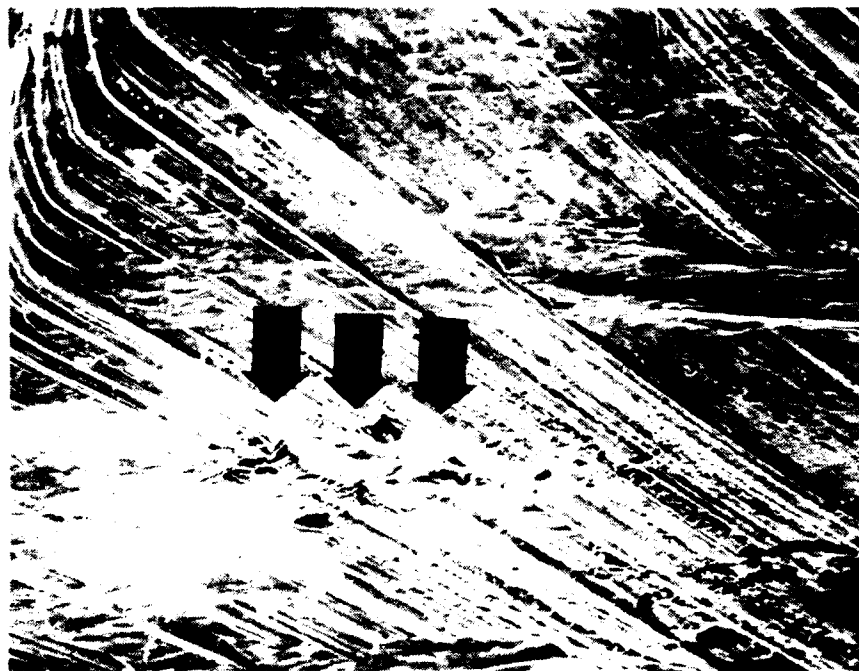


Figure II.7.4. Local microreaction on shear lip of 8090-T8771 from 10 kg·m, pressurized LOX test. (100X) (SEM)

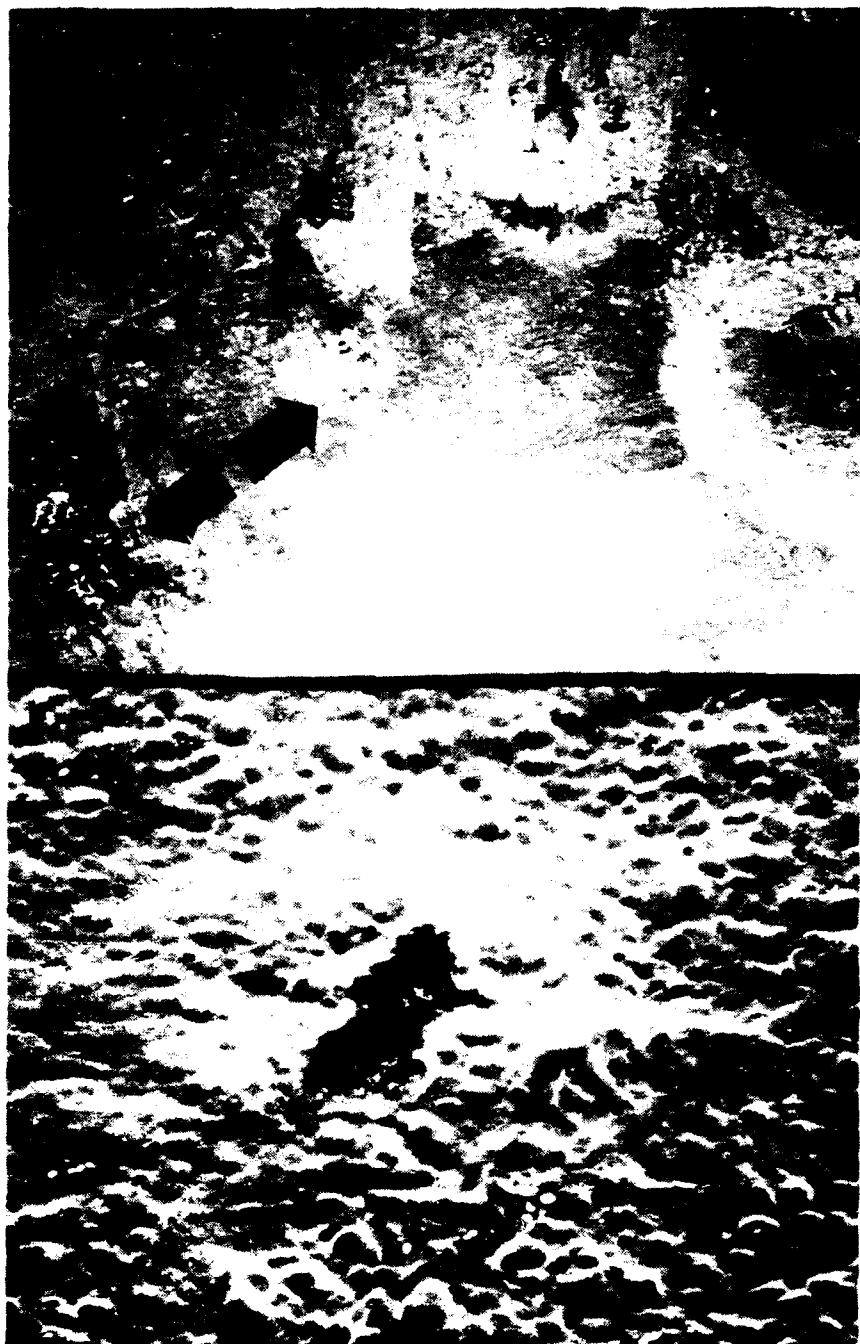
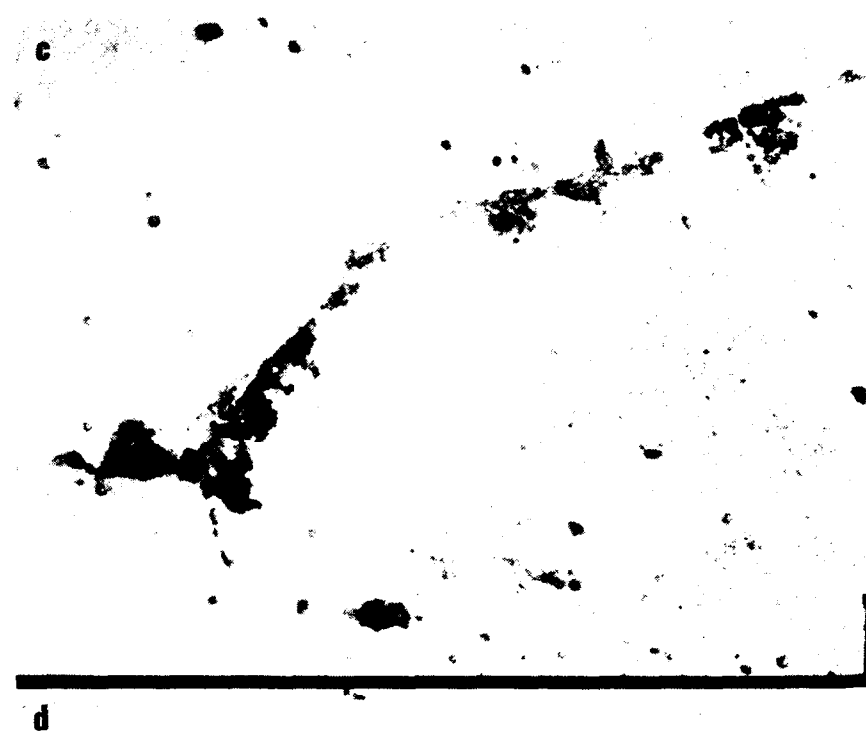


Figure II.7.5. Local microreactions on back of 2090-T81 specimens from 10 kg·m, pressurized GOX tests (a) 50X, (b) 500X, (c) 1000X, and (d) 1000X. (See next page for continuation of figure.)



d

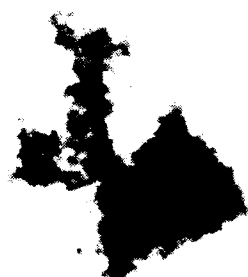
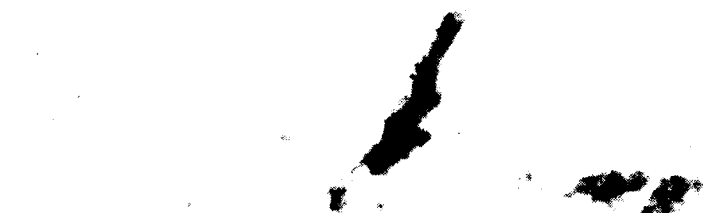


Figure II.7.5., continued



**Figure II.7.6.** Microreactions on the shear lip of 2090-T81 specimens from 10 kg·m GOX tests. (a) 1000X, (b) 3000X, (c) 1000X, and (d) 50X. (See next page for continuation of figure.)

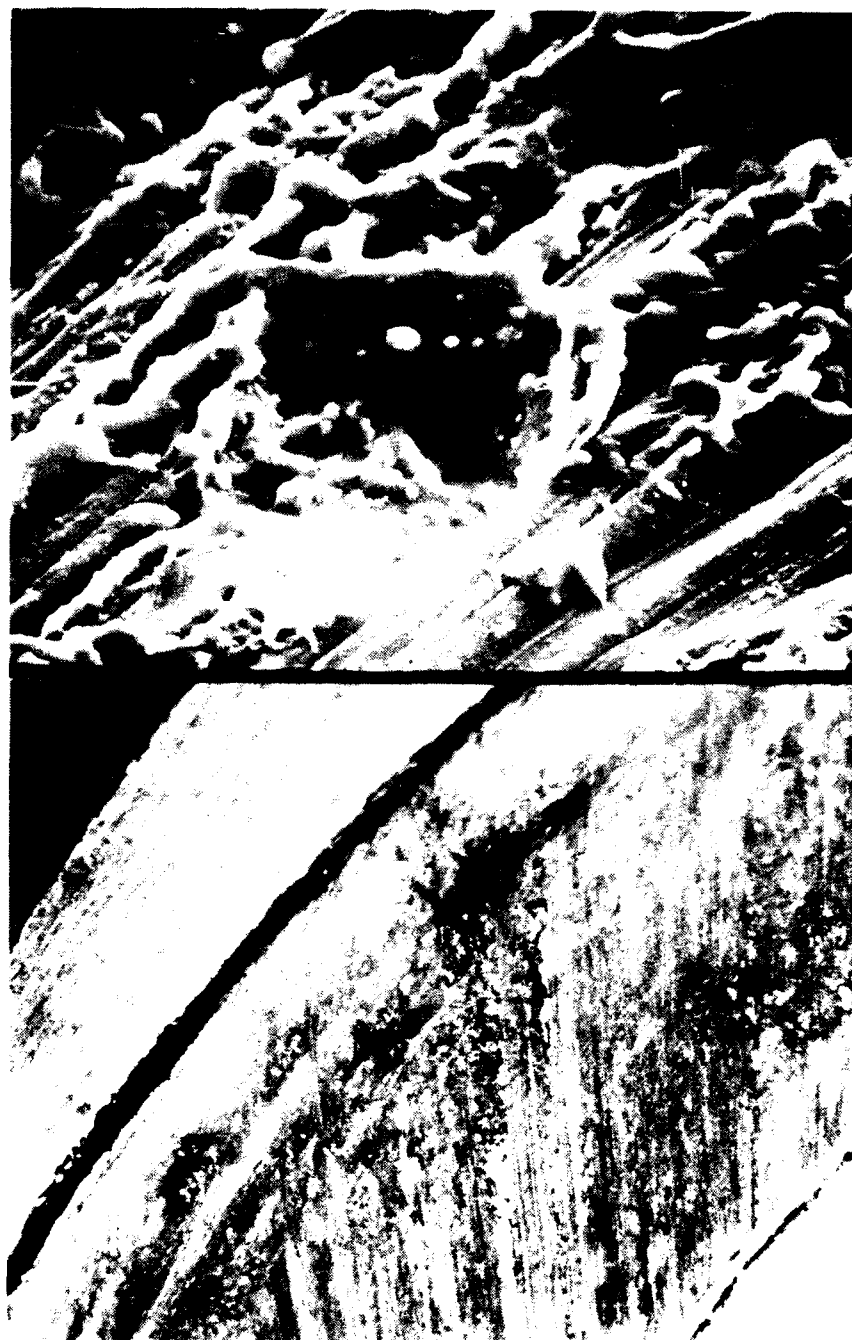


Figure II.7.6., continued

In WL049-T851, microreactions were detected on the shear lip and on the top surface of the specimen between the shear lip and outside perimeter. The microreactions on the specimen surface appear to be associated with second phase particles [Figure II.7.7(a)]. Similarly, microreactions on the shear lip [Figure II.7.7(b,c)] may be associated with second phase particles, but chemical analyses of the particles remaining (or formed) in the darkened regions is needed for association with the local reaction.

In 2219, microreactions were found on the shear lip [Figure II.7.8(a,b)], the bottom of the shear lip [Figure II.7.8(c)], on the under surface of the specimen [Figure II.7.8(d)], and under the striker pin [Figure II.7.8(e,f)]. The microreaction on the under surface seemed to be associated with grain boundaries. Under the striker pin, most traces of the striations from milling were obliterated [Figure II.7.8(e)] and small apparent oxide particles were observed at higher magnification [Figure 7.8(f)].

It is important to note that none of the specimens photographed in Figures II.7.4 to II.7.8 were identified as "reacted" following standard WSTF mechanical-impact test procedures.

Macro- and microreactions on the shear lip were undoubtedly assisted by frictional forces that served both to remove oxide layers and to contribute to localized heating. The microreactions on the top or bottom surfaces of the specimens originated at either specimen inhomogeneities, such as second phase particles, or as a result of heavy deformation, such as adiabatic shear bands.

#### II.7.4.2. Size of Reactions

Under NASA specification NHB 8060.1B<sup>1</sup>, reactions are judged to occur if a flash is detected during the impact or if a burned or charred area on the specimen is visually observed. In Part I, no flashes were observed in WSTF tests. In the MSFC pressurized test apparatus, instrumentation to detect flashes was not in use. In Part II at WSTF, numerous flashes were recorded in open-cup tests, but no flashes were recorded in pressurized tests (perhaps because the position of the photocell was too close to the striker pin, limiting detection to a small region around the circumference of the specimen).

In Part I, all but one burn recorded at MSFC occurred along the shear lip of the specimen. In Part II, all but one of the burns recorded in WSTF open-cup and pressurized tests were also found to occur along the shear lip.

Specimens (10 each of 2090-T81, WL049-T851, and 2219-T87) from open-cup and pressurized tests in the Part II program at WSTF were examined using a 2X power magnifying glass, a 50X power optical microscope, and an up to 2000X power scanning electron microscope. The results of our observations are summarized in Table II.7.1. Examining those specimens from the pressurized-machine tests using a magnifying glass, three more burns were detected on the shear lips in 2090 and WL049. Many "microreactions" (19 more reactions) were observed on both the shear lip and under surface (outside the striker-pin-impression area) using the optical microscope on the same three alloys. Using the SEM, many microreactions were found both



Figure II.7.7. Microreactions on the top specimen surface (a) 100X, and shear lip (b) 3000X, and (c) 1500X of WL049-T851 from pressurized LOX tests at 10 kg·m. (See next page for continuation of figure.)

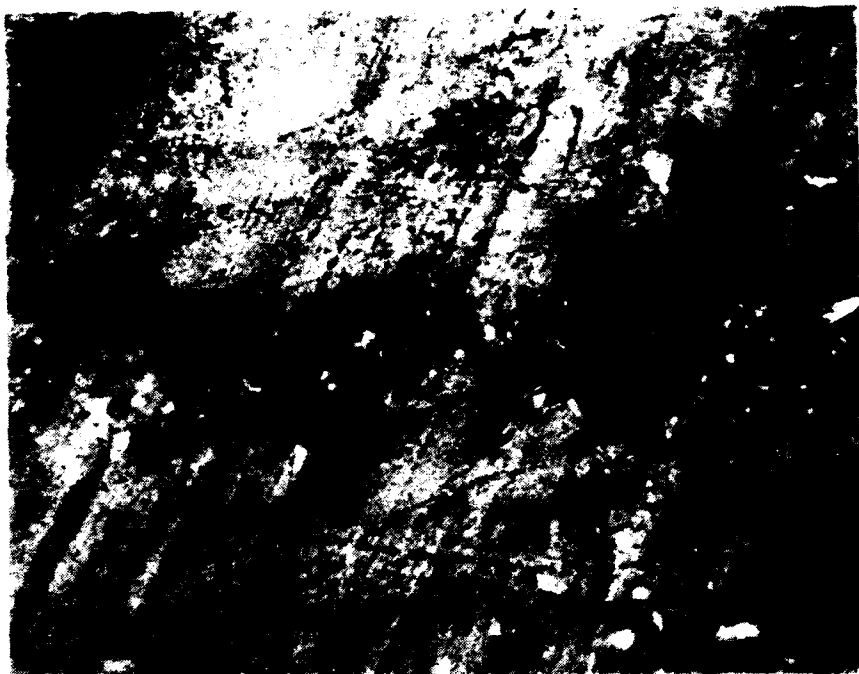


Figure II.7.7., continued



Figure II.7.8. Microreactions in 2219 from pressurized LOX and GOX tests on shear lip (a) T851, 75X and (b) T87, 200X, at bottom of shear lip (c) T87, 500X, on back (d) T87, 1000X, and under striker-pin indentation (e) T87, 5X and (f) T851, 1000X. (See next 2 pages for continuation of figure.)

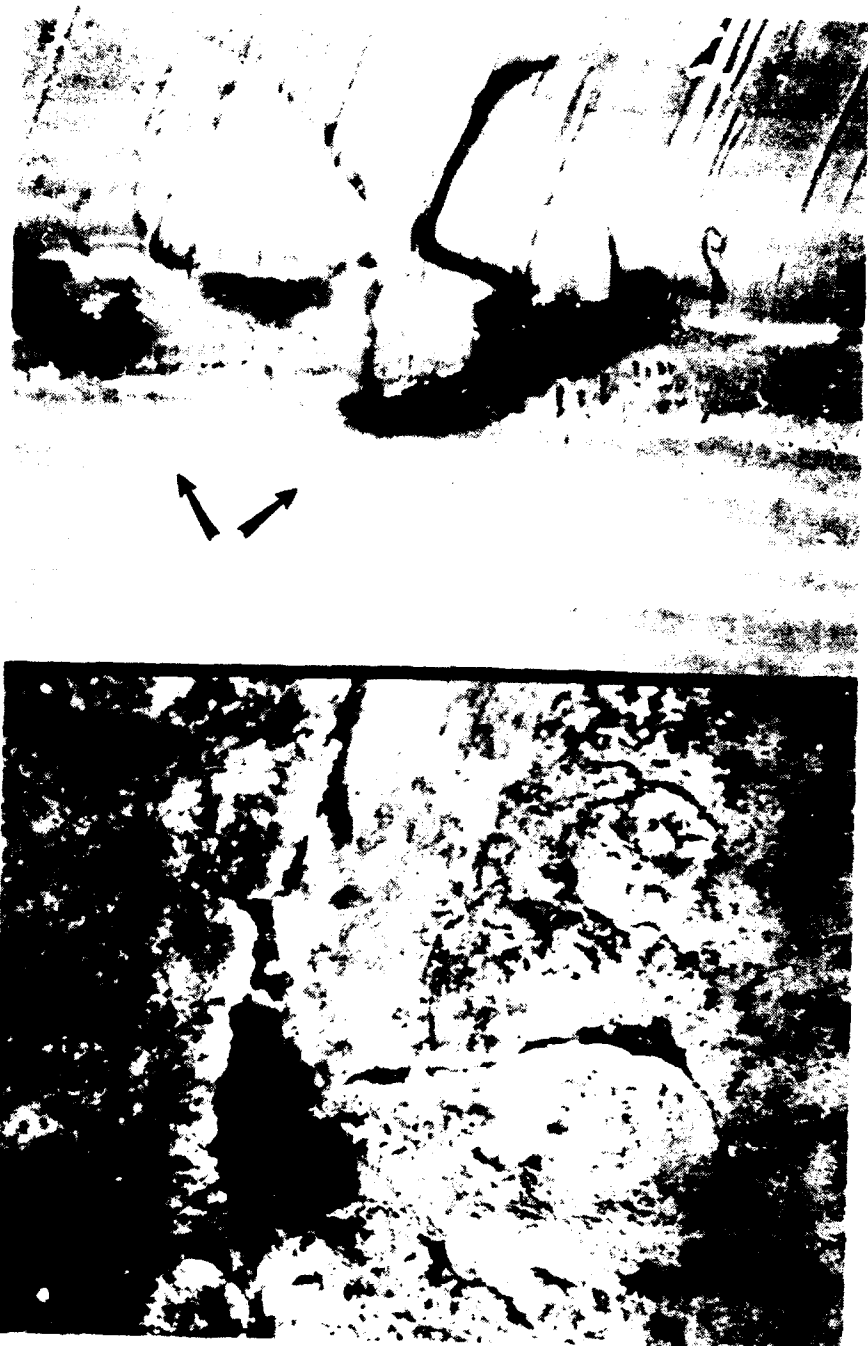


Figure II.7.8, continued

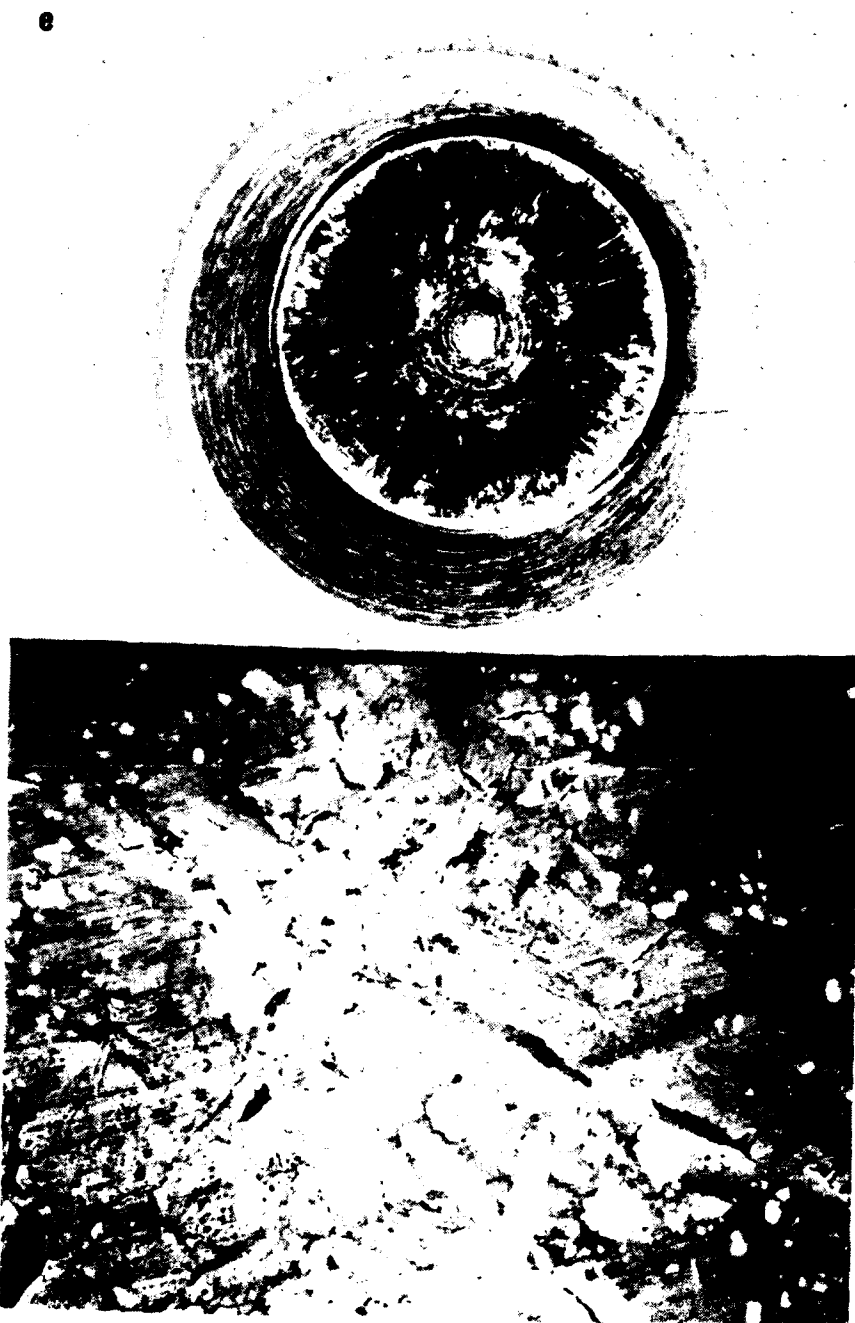


Figure II.7.8., continued

on the shear lip and on both surfaces. Here we use "many" to indicate that, if one took special precautions to count, perhaps, over 50 reactions per specimen would be identified. The term "some" refers to less than about 50 reactions. Figure II.7.9 schematically illustrates these observations: as the optical power of the observation increases, the number of observed reactions increases.

These observations raise the question of a proper definition for a reaction. Clearly, all alloys are "reacting," but in some alloys the propagation of the reaction event is greater. Another variable in identification of reactions is the ingenuity and observational ability of the test personnel charged with identification of reactions. Following identification of burns using a magnifying glass, it was relatively easy in 2 of 3 cases to visually "see" the burn on the shear lip by proper tilting of the specimen with respect to the light field.

Thus, the credibility of this test depends on proper identification of reactions. Should one characterize microreactions as "reactions"? Research relating the size of the reacted area to performance has not been conducted. Yet, for the mechanical-impact test to be judged a creditable test for identifying safe materials for aerospace applications, linkage between performance and reaction size is necessary.

#### II.7.5. Reaction/Fracture Relationship

In Section II.7.2., the forces that result in specimen splitting have been associated with tensile (hoop) stresses. These tensile stresses along the specimen perimeter result from the shear forces that act to expand the specimen radially, in all directions. The constraint to this radial expansion results in the hoop stress. It was demonstrated that these tensile stresses produce specimen splitting (see Figure II.7.2 and associated discussion). Additionally, the fractography of split faces matches that for tensile failures at equivalent temperatures (interim report, Section I.5.). Therefore, specimen splitting may be equated to tensile failure. A minimum absorbed energy for splitting can be estimated for each alloy by using the minimum striker-pin penetration depth and calculating  $E_a$  from Equation (7-1).

Similarly, one can estimate the minimum absorbed energy for reactions (macroreactions) in each alloy. The minimum striker-pin penetration depths at which a reaction occurs is converted to  $E_a$  using Equation (7-1).

In Figure II.7.10, the minimum absorbed energy to cause a reaction is plotted versus the minimum absorbed energy to cause splitting. The solid line denotes equivalent energies. For all alloys in this program, the minimum absorbed energy to cause a reaction is equal to, or larger than, the minimum absorbed energy to cause splitting. That is, for all alloys tensile failure will accompany or precede a reaction. There is one known specimen reaction that is an exception. In the LOX pressurized mechanical-impact tests on WL049-T851 at 8 kg·m and 0.69-MPa (100-psi) pressure, one specimen reacted on the shear lip, but no specimens split.

Thus, from a performance standpoint, one may preclude ignition (under

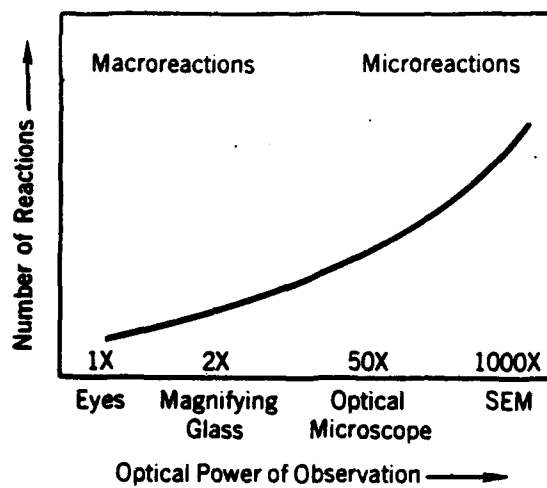


Figure II.7.9. Number of observed reactions vs. optical power of the observation.

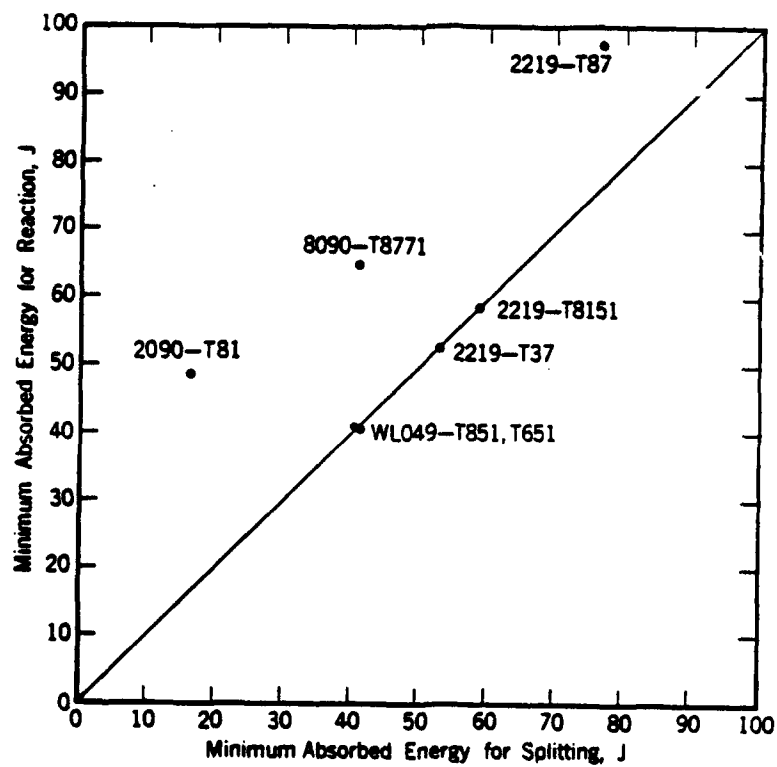


Figure II.7.10. Minimum absorbed energy to cause a reaction vs. minimum absorbed energy to cause splitting.

conditions simulated by the mechanical-impact test) by proper design to prevent tensile failure.

#### II.7.6. Reactions in Al-Li Alloys and Alloy 2219

From open-cup mechanical-impact tests, the number of recorded reactions (flashes, burned areas) from visual (1X) observation for the Al-Li alloys is greater than for alloy 2219. Using Table II.7.1, the recorded reactions for 2090 and WL049 average 6.5 per 20 specimens at 10 kg·m (LOX), while for 2219 there is one recorded reaction for 20 tests. If one uses a magnifying glass, the Al-Li average increases to 8.5 per 20 specimens, the 2219 total increases to 2 reactions per 20 tests. Therefore, there are approximately 4 times more macroreactions in Al-Li alloys, compared with 2219.

However, when one uses more optical power to examine the surfaces in greater detail, the relative frequencies of reactions change. Using optical microscopy to look for microreactions, we found that three specimens of 2090 that had previously been observed to not have a reaction, exhibit local reacted areas. For WL049, six more new specimens were observed to have microreactions and for 2219, six more new specimens have microreactions. Alloys WL049 and 2219 have slightly more specimens exhibiting microreactions than alloy 2090. If one considers both macro- and microreactions, one would conclude that Al-Li alloys and alloy 2219 were similar. This conclusion holds at lower potential-energy levels for open-cup tests, also. While the Al-Li alloys have more macroreactions, 2219 has the equivalent number or more microreactions.

In pressurized LOX and GOX mechanical-impact tests, the same conclusion also is apparent from Table II.7.1. Al-Li alloys have more macroreactions, 2219 has as many or more microreactions. Thus, judging from all detected reactions, the alloys must be considered similar; judging from reactions detected visually, 2219 is better.

The increased frequency of macroreaction for the Al-Li alloys compared to alloy 2219 may be associated with the time for propagation of a thermal transient [Equation (5-1)]. A relative estimate of this time is obtained by comparing the ratio  $C \cdot \rho / K$ ; results were presented in Table II.5.1. The time to propagate a thermal transient is a factor of two greater for 2090 than for 2219 over the temperature range from 90 K to room temperature. Longer thermal-propagation times may be associated with longer times to establish thermal equilibrium. A sudden thermal spike, from a mechanical impact, is dissipated about twice as rapidly in 2219 as in 2090. A larger increase in temperature, locally, is expected in 2090 than in 2219 from equivalent reaction sites (nuclei).

There are other plausible explanations for the apparent larger size of reactions in Al-Li alloys. (1) The deformation of Al-Li alloys is more anisotropic than in 2219. This anisotropic behavior will tend to localize deformation, and thus temperature increases. (2) As discussed in Section II.5.1.7., adiabatic shear-band formation is more prevalent in Al-Li alloys than in 2219. These shear bands can result in considerably higher localized temperatures. (3) Perhaps the exothermic oxidation reaction in Al-Li alloys releases more energy than in 2219 (Al-Cu alloy). We are not aware of data

Table II.7.1. Reaction Frequency.

Alloy	Potential Energy, kg·m (ft·lb)	Machine	Env.	Pressure, MPa (psi)	Reactions*						
					Macro Shear Lip	Visual 1X	Mag. 2X	Glass	Optical 50X	Micro Shear Lip	SEM 1000X
2090-T81	10 (72)	pressurized	GOX	0.69 (100)	0/20	0/10	1/10	1/10	many	many	some
	10 (72)	pressurized	LOX	0.10 (14.7)	0/20	1/10	0/10	0/10	many	many	—
	10 (72)	open cup	ambient	0.10 (14.7)	11/20	2/10	2/10	1/10	—	—	—
8 (58)	open cup	ambient	0.10 (14.7)	9/20	2/10	2/10	2/10	2/10	—	—	—
	WL049-T851	pressurized	GOX	0.34 (50)	0/20	0/10	2/10	2/10	many	many	—
		pressurized	LOX	0.34 (50)	1/20	2/10	0/10	1/10	many	many	—
		open cup	ambient	0.10 (14.7)	9/20	2/10	4/10	2/10	—	—	—
8 (58)	open cup	ambient	0.10 (14.7)	3/20	2/10	2/10	0/10	0/10	many	many	some
	2219-T87	pressurized	GOX	0.10 (14.7)	0/20	0/10	2/10	5/10	many	many	—
		pressurized	LOX	0.10 (14.7)	0/20	0/10	2/10	3/10	many	many	—
		open cup	ambient	0.10 (14.7)	1/20	1/10	2/10	4/10	—	—	—
8 (58)	open cup	ambient	0.10 (14.7)	0/20	0/20	1/10	4/10	4/10	many	many	some

\*Value equals the number of additional reactions detected among the number of specimens examined using the indicated observation method. When using the SEM, "many" > 50 and "some" < 50 reactions.

for comparison.

The observations of very frequent microreactions in all alloys suggest that reactions nucleate (initiate) about equally in these alloys.

The promoted-combustion results from WSTF are discussed in Section II.5.4. They are clear. The flammability of alloy 2219 is much more sensitive to oxygen pressure than are the flammabilities of the Al-Li alloys. The transition from exhausted burning to fall burns occurs at about 0.21 MPa (30 psi) for 2219 and at about 1.7 MPa (250 psi) for Al-Li alloys.

## II.8. SUMMARY

### II.8.1. Definition of Reaction

A proper definition for a reaction from mechanical impact in LOX or GOX is problematical. Reactions (oxidation and material transfer) have been shown to range from the macro-scale, visible with the naked eye, to the micro-scale, visible only with the SEM. Microreactions are much more frequent than macroreactions, as depicted schematically in Figure II.7.9. Detection of smaller macroreactions depends on the angle of lighting, skill of the observer, and amount of discoloration, unless a magnifying glass is used. Therefore, for metal alloys that have a reaction threshold, within the range of absorbed energy used in the mechanical-impact tests, the definition and adjudication of an ignition event by identification of a "burned" or "charred" area is quite arbitrary.

Another event defined as a reaction is flashing. Flashes could not be identified with the pressurized equipment at MSFC as the detector was not in use. Perhaps flashes only within a very restricted region can be detected with the pressurized equipment at WSTF. Yet, when detection equipment was operating in the open-cup WSTF tests in our Part II program, numerous flashes were detected. Specimens that flashed exhibited microreactions.

A problem with the definition of a reaction ignition has been identified. This lack of clarity is compounded by lack of correlation of reactability from mechanical-impact tests with prototypical or in-service performance. This uncertainty of the definition of a reaction poses a severe constraint in the use of the mechanical-impact test as a qualification test for metals for aerospace applications. Clearly, to use this test to qualify metals, macro- and micro-reactivities must be correlated with performance to permit identification of acceptable sizes of reactions.

### II.8.2. NASA Standard NHB 8060.1B (Paragraph 413, test 13)

The major deficiency in the mechanical-impact test for metals is the inability to define a reaction and, in so doing, to relate the definition to in-service performance. Therefore, we advise that the test should not be used as a qualification test until this issue is resolved.

However, as discussed in the interim report (Section I.8.9.), this standard currently has other deficiencies that permit wide variations in significant test parameters between the test laboratories. The major changes to address these inadequacies are listed here:

1. Specifications should be adhered to for striker-pin geometry and surface finish.
2. Specifications should be required for maximum allowable eccentricity of striker-pin impact area with specimen center.
3. New cleaning and quantitative surface-finish specifications for metallic specimens are recommended.

4. Temperature measurement and control of the specimen and its environment should be defined.
5. Impact energy ( $E_i$ ) should be redefined; it should include the frictional contributions. That is,  $E_i = E_p - E_f$ .
6. Results should be stated in terms of absorbed energy.  $E_a = E_i - E_r$ , not impact energy. Knowledge of the specimen's absorbed energy permits comparison between laboratories and application to failure analyses.
7. Use of absorbed energy as a basis for reporting test results and for specifying test requirements would have beneficial results: (1) interlaboratory results would be comparable, (2) failure analyses could be realistically compared to test data, (3) alloy-to-alloy comparisons would be meaningful. (Currently, Al alloys are judged inferior, but, if their lower resiliency is considered, this probably would not be the case.)
8. Twenty specimens are not sufficient, statistically, when the probability of ignition is less than about 0.20 (the case of Al alloys at 65 J and in a LOX environment). As discussed in Section I.8.6., more specimens or an increased impact energy are required to increase the confidence level of the results.
9. To ensure more consistent machine resiliency and better comparison between open-cup and pressurized tests, specimen cups for each type of test should be made of the same alloy.
10. Currently, there is interlaboratory diversity in the detection of flashes (MSFC doesn't use any detectors, WSTF does). The issue of whether a flash during impact represents a reaction (as currently stated in the standard) must be resolved. Microreactions were always associated with flashes in this series of tests.

#### II.8.3. Reaction/Fracture Energies

In mechanical-impact tests in a LOX or GOX environment, Al alloys experience very high compressive, shear, and tensile stresses that result in extensive axial compressive deformation, radial shear deformation, and circumferential cracking (splitting) under tensile (hoop) stress. The deformation and fracture attributes have been characterized. It is demonstrated for all Al alloys that the absorbed energy necessary to achieve reactions is equivalent to, or greater than, the tensile failure energy. Therefore, the prevention of tensile failure in the design of cryogenic tankage will preclude ignition in LOX or GOX from mechanical impact, under similar conditions.

#### II.8.4. Comparison of Al-Li Alloys with 2219

Extensive mechanical-impact tests, using modified open-cup and pressurized equipment at WSTF, have been conducted on the alloys 8090, 2090,

WL049, and 2219 in various tempers. Both LOX and GOX environments, and pressures up to 0.69 MPa (100 psi) have been used. The results suggest that both react with similar frequency, but that reactions tend to be larger in Al-Li alloys, compared with 2219. However, in promoted-combustion tests, also conducted at WSTF in GOX at various pressures, Al-Li alloys are superior to 2219. Extensive burning in 2219 occurs at pressures on an order of magnitude less than that required to achieve equivalent burning in Al-Li alloys.

Energy levels required to induce reactions in the Al alloys are higher, or equivalent to, the energy required to induce tensile failure. Thus, proper design to ensure structural integrity will also ensure a proper level of oxygen compatibility. We conclude that both Al-Li alloys and 2219 have equal potential for use in oxygen environments under conditions equivalent to those simulated by mechanical-impact and promoted-combustion tests.

## II.9. RECOMMENDATIONS

- \* The use of Al-Li alloys is equivalent to the use of alloy 2219 in oxygen environments under conditions for ALS cryogenic tankage that represent those simulated by mechanical-impact and promoted-combusted tests.
- \* The Al alloys in this program reacted at induced mechanical energy (absorbed energy) levels either the same as, or greater than, those needed for tensile failure. Proper design to prevent tensile failure will eliminate reactions under similar conditions.
- \* The current mechanical-impact open-cup and pressurized tests should not be used as a qualification test for structural alloys for ALS cryogenic tankage. Definition of a reaction is arbitrary and has not been related to service use. If the definition of a reaction is resolved, a number of modifications to the impact tests are recommended.

## II.10. ACKNOWLEDGMENTS

We thank the staff of White Sands Test Facility for careful and diligent conduction of the open-cup and pressurized tests. We especially are indebted to J. Stoltzfus and C. Garcia-Salcedo of WSTF for their expert consultation and leadership, to M. Rucker for redesign of the WSTF pressurized test facility, to R. Blackstone and D. Hirsch for their contributions in conducting the tests, and to G. Payton for capable monitoring of the various materials.

In addition, the authors thank Will Fehringer and Ray Santoyo for careful measurement of the hardness and tensile properties, and impact penetration depths. Becky Wait overcame all of our grammatical inconsistencies to produce an excellent final copy.

## II.11. REFERENCES

1. Weeks, L. M., "Flammability, Odor, and Offgassing Requirements and Test Procedures for Materials in Environments That Support Combustion, NASA, Office of Space Transportation Systems, Washington, DC, Report No. NHB 8060.1B, 107 pp. (1981).
2. Reed, R. P., Purtscher, P. T., McColskey, J. D., Walsh, R. P., Berger, J. R., Drexler, E. S., Santoyo, R. L., and Simon, N. J., "Comparative Measurements of Cryogenic Mechanical Properties of Al-Li Alloys and Alloy 2219," in preparation.
3. Simon, N. J., Drexler, E. S., and Reed, R. P., "Review of Cryogenic Mechanical and Thermal Properties of Al-Li Alloys and Alloy 2219," in preparation.
4. "Standard Test Method for Compatibility of Materials with Liquid Oxygen (Impact Sensitivity Threshold and Pass-Fail Techniques)," ASTM Standard D2512, American Society for Testing And Materials, Philadelphia, PA, 67-78 (1982).
5. Bransford, J. W., Bryan, C. J., Frye, G. W., and Stohler, S. L., "LOX/GOX Mechanical Impact Tester Assessment," National Aeronautics and Space Administration, Washington, DC, Report No. NASA TM 74106, 104 pp. (1980).
6. Bryan, C. J., "NASA Mechanical Impact Testing in High-Pressure Oxygen," in Flammability and Sensitivity of Materials in Oxygen-Enriched Atmospheres, ASTM Special Technical Publication 812, Ed. B. L. Werley, American Society for Testing and Materials, Philadelphia, PA, 9-42 (1983).
7. Markstein, G. H., "Combustion of Metals," AIAA Journal 1, 550-562 (1963).
8. Grosse, A. V., and Conway, J. B., "Combustion of Metals in Oxygen," Industrial and Engineering Chemistry 50, 663-672 (1958).
9. Seybolt, A. U., "Oxidation of Metals," Advances in Physics 12, 1-43 (1963).
10. Macek, A., "Fundamentals of Combustion of Single Aluminum and Beryllium Particles," in Symposium on Combustion, Vol. 11, 203-214 (1966).
11. Bouriannes, R., and Manson, N., "Nonautonomous and Autonomous Combustion of Spherical Aluminum Particles in Oxygen-Nitrogen or Oxygen-Argon Mixtures," Compt. Rend. Acad. Sci., Series A 270, 1546-1549 (1970).
12. Bouriannes, R., "Temperature of Aluminum During its Combustion in Argon-Oxygen Mixtures, Nitrogen, and Air," Compt. Rend. Acad. Sci., Series C 275, 717-720 (1972).
13. Merzhanov, A. G., Grigorjev, Yu. M., and Gal'chenko, Yu. A., "Aluminum Ignition," Combustion and Flame 29, 1-14 (1977).
14. Prentice, J. L., "Metal Particle Combustion Progress Report," Naval Weapons Center, China Lake, CA, Report No. NWC TP 4435 (1968).

15. Moskovits, M., "Catastrophic Aluminum Reactions in an Oxy-Gas Flame," ALCAN International Limited, Kingston, Ontario, Canada, Report No. KS-133-71-11/04 (1971).
16. Razdobreev, A. A., and others, "Mechanism of Ignition and Combustion of Aluminum Particles," *Fiz. Gorenija Vzryva* 12, 203-208 (1976).
17. Derevyaga, M. E., Stesik, L. N., and Fedorin, E. A., "Ignition and Combustion of Aluminum and Zinc in Air," *Combust. Explos. Shock Waves* 13, 722-726 (1977).
18. Jacobson, M., Cooper, A. R., and Nagy, J., "Explosivity of Metal Powders," U.S. Bureau of Mines, Report No. RI 6516 (1976).
19. Prentice, J. L., "Combustion of Pulse-Heated Single Particles of Aluminum and Beryllium," *Combustion Science and Technology* 1, 385-398 (1970).
20. Bouriannes, R., "Experimental Study of Aluminum Combustion in Oxygen-Argon Mixtures, Nitrogen, and Air," *Rev. Int. Hautes Temp. Refrac.* 10, 113-124 (1973).
21. Prentice, J. L., and Nelson, L. S., "Differences Between the Combustion of Aluminum Droplets in Air and in an Oxygen-Argon Mixture," *Journal of the Electrochemical Society* 115, 809-812 (1968).

## APPENDIX A

### **Design of Experiment for Mechanical Impact Testing of Aluminum-Lithium Alloys.**

**Bao Nguyen and Bruce Pham, Lt, USAF, Astronautics Laboratory, Air  
Force Systems Command, Edwards AFB, CA (Jun 90).**

---

For the purpose of evaluating the potential hazards of Aluminum-Lithium (Al-Li) applications in oxygen-tank service, the test program will assess the major factors which adversely affect material reactivity with oxygen. This appendix will address the use of a Taguchi design of experiment to study the material reactivity under the mechanical impact test (NASA Handbook 8060.1B).

The working group comprised of the Steering Committee of the ALDP Structures/Materials/Manufacturing technology area, the National Institute of Standards and Technology (NIST), NASA White Sands Test Facility (NASA/WSTF), and the Aerospace Corporation. A summary of potential causes and effects was developed by the group (Fig. 1). From this, three main factors were identified as the major contributing factors to material reactivity under the mechanical impact tests with oxygen. These are the impact energy, the oxygen test pressure, and the materials being evaluated. A potential interaction effect between the impact energy and the test pressure was also identified. This interaction may have played a role in affecting the actual impact energy delivered to the test sample.

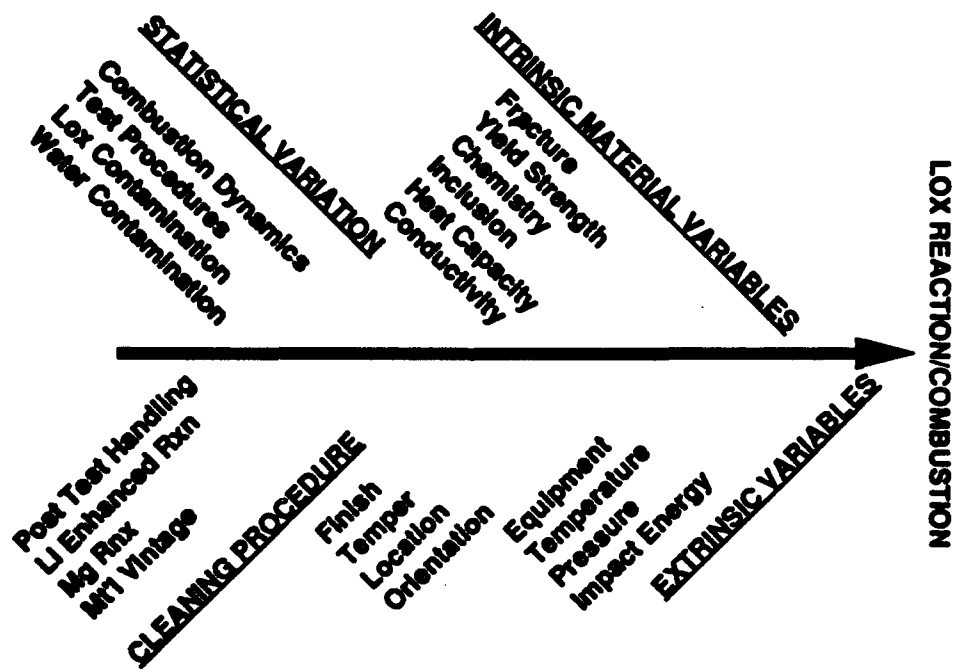


**FIGURE 1: FISH BONE REACTION HYPOTHESIS**

A secondary effect, the present of liquid oxygen (LOX) or gaseous oxygen (GOX) which affects the temperature of the test, was also included into the test matrix (Fig. 2). From the thermodynamic point of view, and

based on the extensive flammability evaluation completed by the White Sands Test Facility, NASA/Johnson Space Center, for aluminum-lithium alloys, these factors above constitute the combustibility triangle (Fig 3).

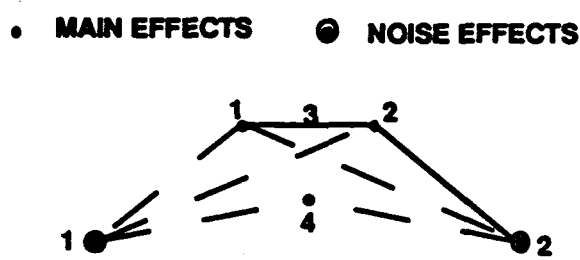


FIGURE 2: LINEAR GRAPH

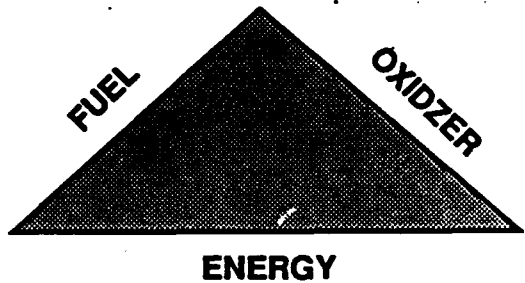


FIGURE 3: REACTION TRIANGLE

The Taguchi orthogonal experiment array L9 was used<sup>1</sup>. This efficient array enabled the evaluation of the three main effects above and one interaction effect between two of the factors. The array is structured to evaluate at three levels for each of these effects in a total of 9 experimental runs. The array was coupled with a two level outer array to assess the effect of GOX and LOX. Table 1 illustrate the set up of the array with the entries denoting the levels of setting for each of the effects being studied.

#	CONTROL FACTORS				GOX		LOX	
	CHAMBER PRESSURE	IMPACT ENERGY	INTERACTION WITH 1 & 2	MT'L	SPLITS	RXNS	SPLITS	RXNS
1	1	1	1	1	0	0	8	0
2	1	2	2	2	20	0	20	0
3	1	3	3	3	0	0	0	0
4	2	1	2	3	0	0	5	2
5	2	2	3	1	0	0	0	0
6	2	3	1	2	10	0	17	0
7	3	1	3	2	20	1	20	2
8	3	2	1	3	0	0	0	1
9	3	3	2	1	0	0	0	0

Table 1: Experiment Array L9 ( $3^4 \times 2^1$ )

For this program, test chamber pressure was assigned to the main effect column 1, impact energy to column 2, and material effect to column 4.

Column 3 was assigned to the interaction effect between the impact energy and the chamber pressure.

Level 1, 2, and 3 of the chamber pressure were set at ambient, 50, and 100 psi, respectively. Similarly, the impact energy levels were 10, 8, and 6 kg-m. For the material effect, the three levels were Al-2219, Al-Li 2090, and Weldalite 049. Both the frequency of reactions and the number of coupons which crack or split when subjected to the impact load were recorded.

A sampling population of 20 impacted specimens were obtained for each of the runs. For the array, a total of 360 specimens were tested, one half in LOX and the other half in GOX. To further control the potential effect due to the drifting of equipment settings, the array was randomized prior to the test. Impact energy was calibrated at the end of each experiment run with Al-Li 2090 coupons to ensure the consistency of the tester. The test cell pressure was also tracked for each of the impacts to record the initial, transient, and final conditions. The results are recorded in the four rightmost columns of Table 1.

For the purpose of evaluation, reactivity is defined as evidence of charring or burning which produces heavily oxidized, melted metal. The impacted specimens were examined with naked-eye and 50X microscopes. Evidence of burning were further studied using a Scanning Electron Microscopy (SEM) with up to 10,000X magnification power coupled with a chemical composition analyzer to confirm the present of oxygen as part of the reaction byproducts.

Only evidence of severe local melting in GOX was observed under high magnification for one coupon in run number 7. In the LOX environment, two samples in run 8 and 4 showed definite reactions which could be seen with the naked-eye and were confirmed with having heavily oxidized layer. The rest of the reactions was at microscopic level which had severed local melting with presents of oxygen in the reaction byproducts. Figures 4 through 8 show the different types of reaction, from macro to micro levels, which were observed.

Analyzing the results of the array can be visualized by drawing the orthogonal box for the experiment settings (Fig. 9). The orthogonal surfaces of the box encompass all set of conditions to be evaluated. The effect of each factors is determined by comparing the aggregated results across the orthogonal surfaces generated by the changes of the factor in question. The impacts of other factors would have canceled out due to the orthogonality of the array.

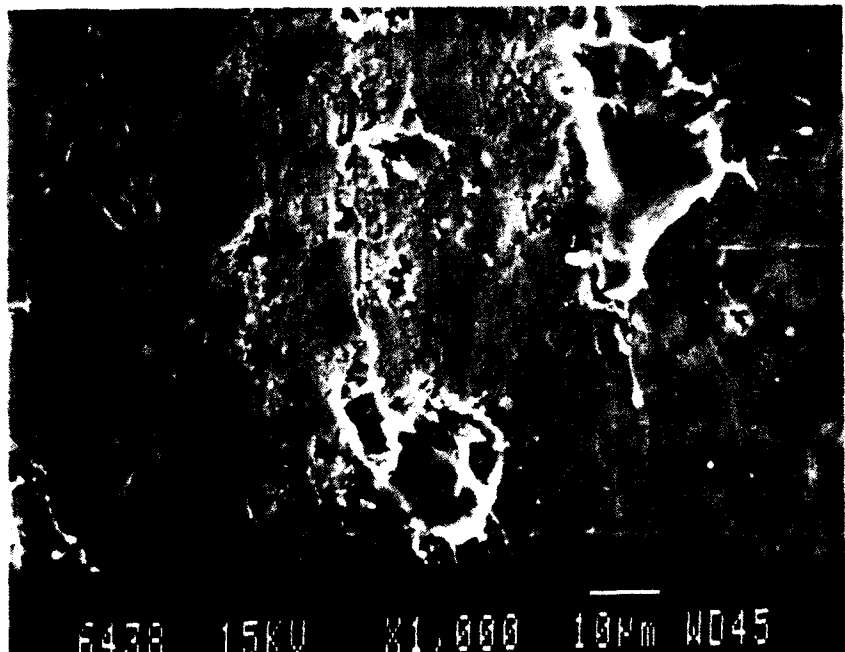


**Figure 4. Local Melting, Al-Li 2090, 10 Kg-m, 100 psi, GOX  
Unseen by Naked-eye**

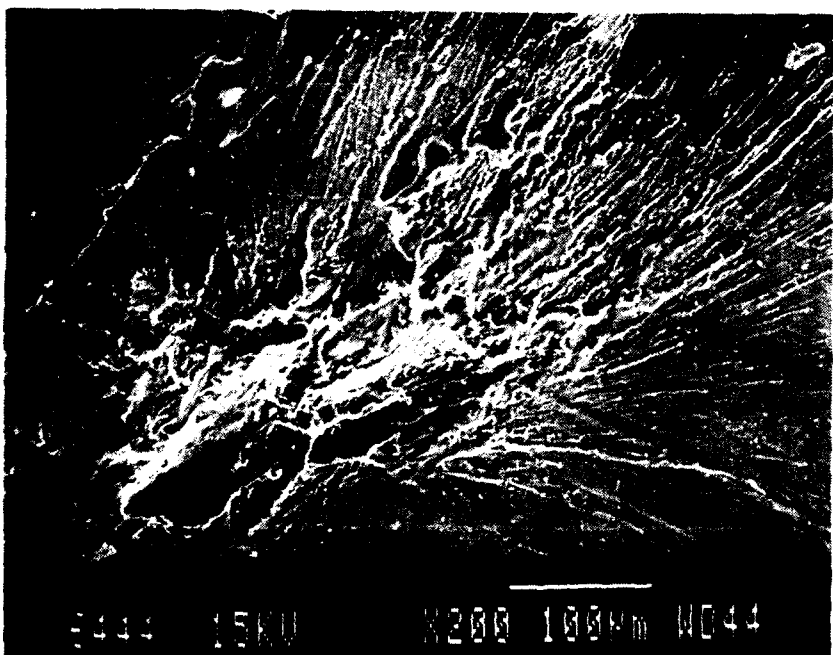
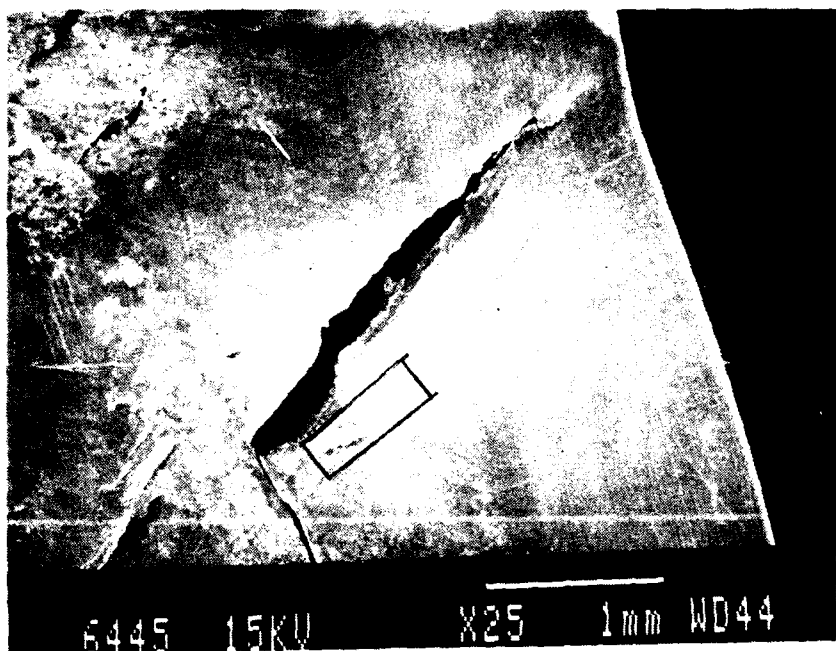


**Figure 5. Macro Reaction, Al-Li 2090, 10 Kg-m, 100 psi, LOX**  
**(a) 25X and (b) 200X Magnification of the Same Reaction Site**

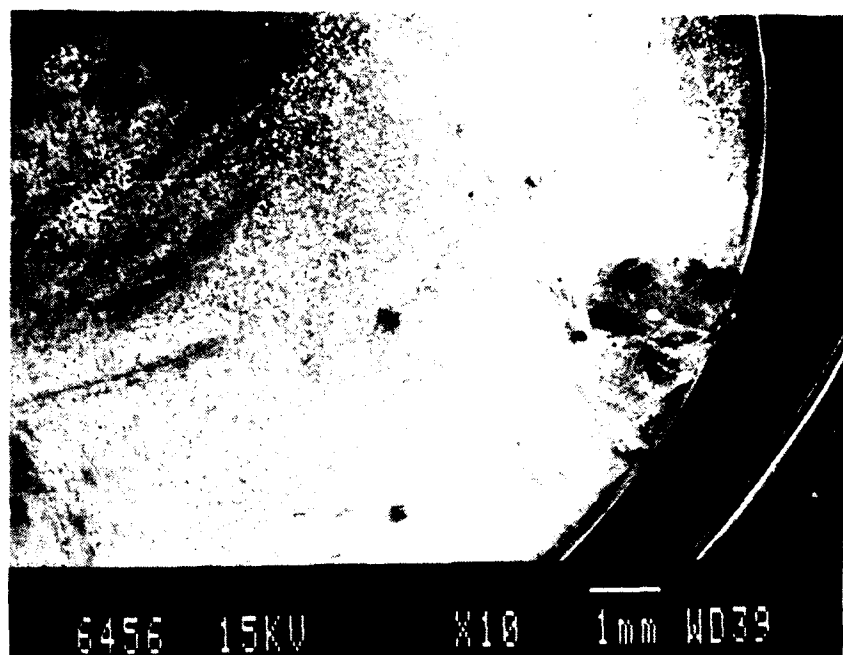


**Figure 6. Oxidized Byproduct within Reaction Site  
Weldalite, 8 Kg-m, 100 psi, LOX**

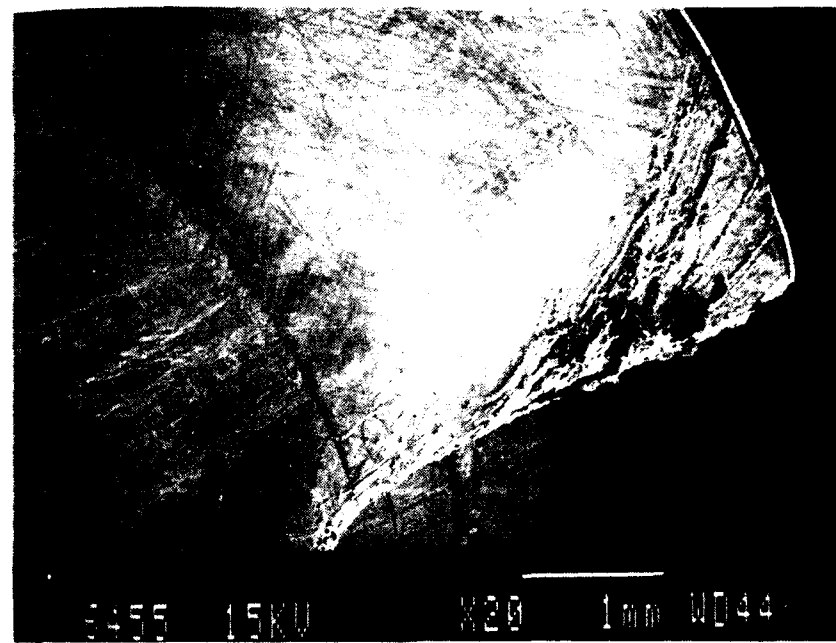
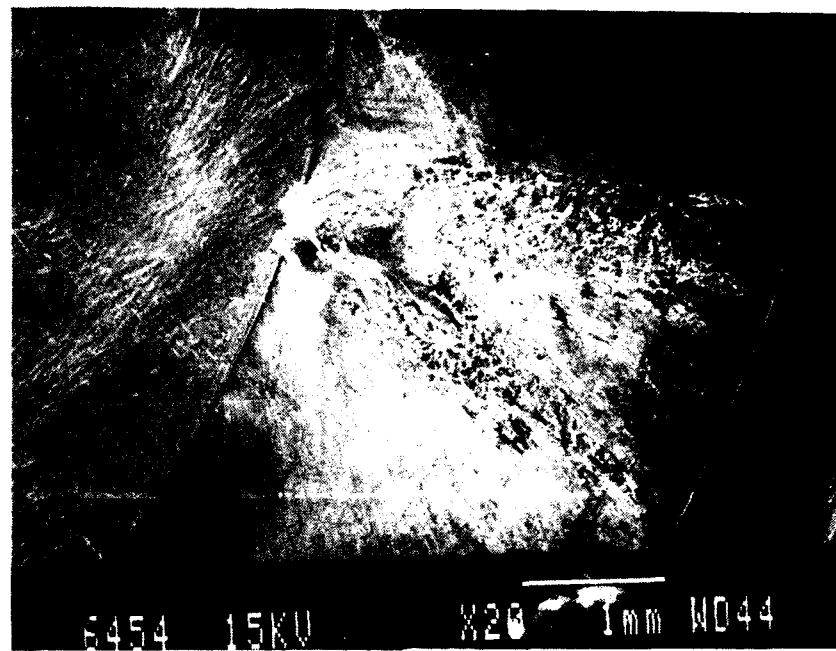


**Figure 7. Extensive Macro-Reaction with Melted Spray, Same Sample of Weldalite, 10 Kg-m, 50 psi, LOX**

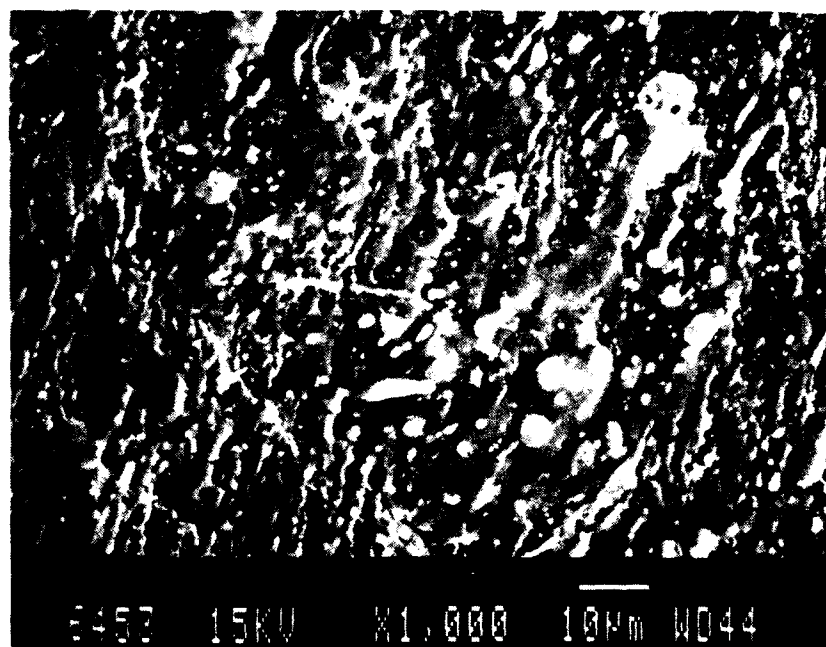


**Figure 8. Micro-Reaction Site with Recrystallized Surface  
Weldalite, 10 Kg-m, 50 psi, LOX**

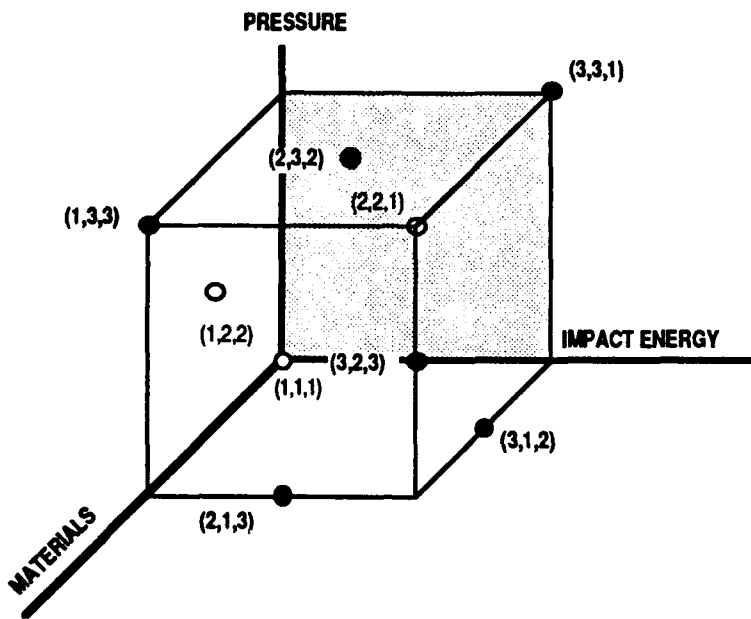


Figure 9: Orthogonality of Factors Evaluated

Using data averaging method, the response characteristics are presented in Table 2 below.

	Levels	PRESSURE		IMPACT		P-I INTERACTION		MATERIAL	
		Splits	Rxns	Splits	Rxns	Splits	Rxns	Splits	Rxns
GOX	1	6.7	0	6.7	.33	3.3	0	0	0
	2	3.3	0	6.7	0	6.7	0	16.7	.33
	3	6.7	.33	3.3	0	6.7	.33	0	0
LOX	1	9.3	0	11	1.33	8.3	.33	2.6	0
	2	7.3	.67	6.7	.33	8.3	.67	19	.67
	3	6.7	1	5.7	0	6.7	.67	1.6	1

Table 2. Response Table

These numbers were plotted on the response charts. Figure 10 showed that the difference in reaction rate was negligible considering the number of the test specimen, the variation in the deformation load caused by the test equipment, and the low probability of a reaction under impact loads<sup>2</sup>. Note, that the reaction frequencies are out of a possible 20 reactions. Figure 11 showed that Al-Li 2090 is the least resistant to fracture under the mechanical impact test. Also, the number of splits went up in the colder LOX environment (95 K vs. 300 K) indicates the negative affect of low temperatures on impact resistance.

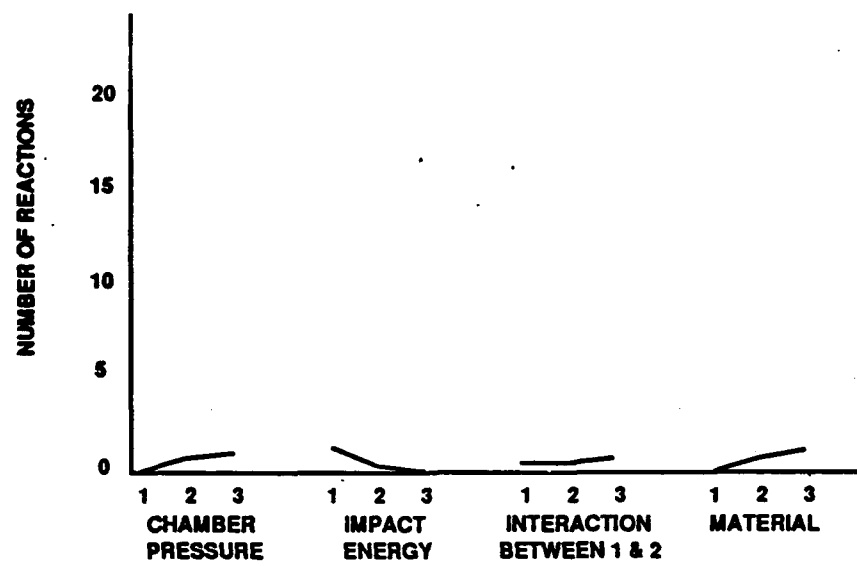


Figure 10: Reaction in LOX Environment

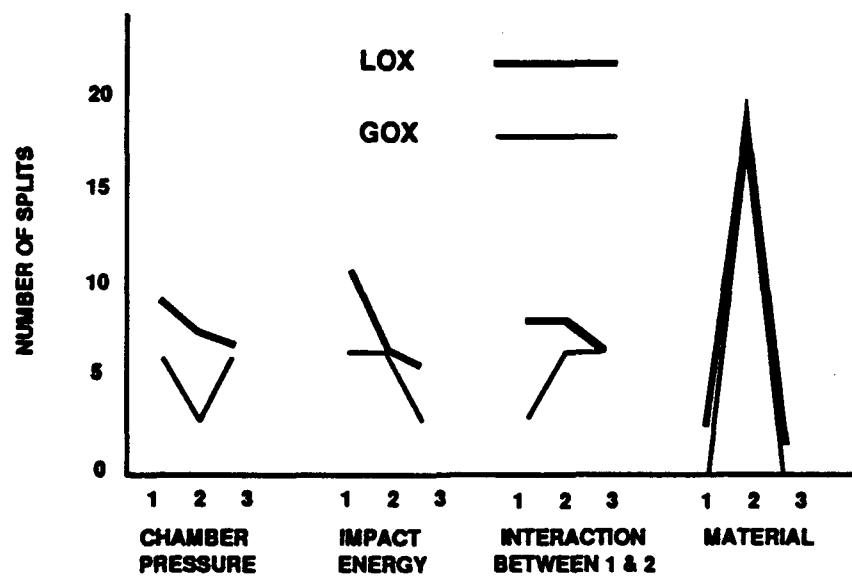


Figure 11: Effect of Factors on Splits

## CONCLUSION:

Oxygen compatibility for metal products could not be thoroughly assessed using the Mechanical Impact Test as per the current standards due to the very limited but widely scattered data. First, the impact load could not be delivered consistently to generate the same impact deformation on every coupon. Second, current requirements for classification of reactions are qualitative and are subjected to individual interpretation.

However, within the parameters of the Mechanical Impact Test, there are no significant difference in oxygen compatibility between the aluminum-lithium alloys studied and the aluminum 2219 being used for the space shuttle external tank. The frequency of reactions between the three alloys studied was too small to conclusively assess their compatibility with oxygen.

Although there was a strong tendency of fracture under impact load for the Al-Li 2090, the result may not be representative of actual application. Yet, within the same parameters of this test, Al-Li 2090 may be more susceptible to impact damage due to the fact that the alloy is not as ductile as Al 2219 or as exceptionally strong as Weldalite 049.

---

## REFERENCE:

1. Taguchi Methods - Orthogonal Arrays and Linear Graphs, American Supplier Institute, Inc., 1987.
2. R. P. Reed, N. Simon. "Aluminum Alloys for Cryogenic Tanks: Oxygen Compatibility Interim Report", National Institute of Standards and Technology, Boulder, CO, May 1990.